Interoperable Protection and control of multi-terminal HVDC systems

Liu, L.

DOI
10.4233/uuid:b501ee35-170e-4b3f-b1e9-0087cc995c49

Publication date
2024

Document Version
Final published version

Citation (APA)
Liu, L. (2024). *Interoperable Protection and control of multi-terminal HVDC systems*. [Dissertation (TU Delft), Delft University of Technology]. https://doi.org/10.4233/uuid:b501ee35-170e-4b3f-b1e9-0087cc995c49

Interoperable Protection and Control of Multi-terminal HVDC Systems

INTEROPERABLE PROTECTION AND CONTROL OF MULTI-TERMINAL HVDC SYSTEMS

Dissertation

for the purpose of obtaining the degree of doctor
at Delft University of Technology,
by the authority of the Rector Magnificus Prof.dr.ir. T.H.J.J. van der Hagen,
Chair of the Board for Doctorates
to be defended publicly on
Monday 22 January 2024 at 12:30 o'clock

by

Le LIU

Master of Engineering in Electrical Engineering, Xi'an Jiaotong University, China
born in Weinan, China

The dissertation has been approved by the promotors.

Composition of the doctoral committee:

Rector Magnificus	chairperson
Prof. dr. ir. M. Popov	Delft University of Technology, promotor
Dr. A. Lekić	Delft University of Technology, copromotor

Independent members:

Prof. dr. X. Kang	Xi'an Jiaotong University, China
Prof. dr. Z. Chen	Aalborg University, Denmark
Prof. dr. ir. P. Bauer	Delft University of Technology
Prof. dr. P. Palensky	Delft University of Technology
Prof. ir. M. van der Meijden	Delft University of Technology/Tennet
Prof. dr. ir. O. Isabella	Delft University of Technology, reserve member

This research is supported by the China Scholarship Council (Scholarship No. 202006280010).

Keywords: HVDC protection,Traveling wave analysis, Fault location, MMC control, Interoperability
Cover by: Ron Zijlmans | info@ron.nu
Cover image by: Herman IJsseling
Printed by: ProefschriftMaken

ISBN 978-94-6469-705-6

An electronic version of this dissertation is available at
http://repository.tudelft.nl/.

Dedicated to my country,
my parents, my dream.

"路虽远行则将至, 事虽难做则必成."

Le Liu
Delft, Nov 2023

CONTENTS

SUMMARY

The MMC-based MTDC systems are considered a promising solution for long-distance power transmission, integration of renewable energy sources, and interconnection of power grids. Nowadays, MMC-based MTDC systems have been successfully developed in various projects worldwide and are expected to play a significant role in future electrical power transmission systems.

Despite the benefits provided by the MMC-based MTDC system, various technical problems emerge. For example, in case of a DC fault on HVDC transmission lines, the DC voltage suffers a deep sag, and the fault current increases to the peak value after several milliseconds, the system stability is seriously affected. The fault currents will easily damage the power electronics and may lead to a collapse of the entire system if the faults are not cleared promptly. Thus, it is crucial to implement a fast, selective, and reliable DC fault protection technology in the system for fault detection. Once the fault is cleared, it is important to know the exact fault location to repair the faulty sections and to restore the system. Hence, an accurate DC fault location technique is of utmost importance for the MTDC system, which would significantly minimize electricity loss and expedite the system restoration process in the event of power outages. In addition, there is a lack of standardization in MMC control, and the majority of HVDC projects are constructed in a vendor-specific manner. As of today, it is unclear how MMC converters from different manufacturers will interoperate with each other. These pose new challenges to the performance of HVDC protection and MMC control and need to be addressed to manage, safeguard, and accelerate the practical feasibility of this system.

The research in this thesis aims to address the shortcomings that have not been addressed in the state of the art, mainly related to the challenges arising when DC faults occur in the MMC MTDC systems and, as such, could provide promising solutions for future practical MTDC applications. The main topics are *MMC control & interoperability, Protection, and Fault location* for the MMC-based MTDC system. The thesis deals with designing a robust protection scheme, a fault location method, and an investigation of the interoperable MMC controllers. The chapters are organized as follows.

In chapter 1, we first demonstrate the technical advantages of MMC MMC-based MTDC system compared to traditional LCC-HVDC and HVAC systems. Then, this chapter presents newly emerged phenomena and technical issues that may arise, posing various challenges. This is followed by a discussion of the main research topics and the state-of-the-art protection and control methods, including their advantages and limitations. Based on this, the key research questions are proposed.

In chapter 2, we introduce the critical components, e.c., MMCs and DCCBs, within the MMC-based MTDC grids. Their roles and working principles are explained, providing a deep understanding of these complex systems. In addition, we use an example to analyze the DC fault responses in an MTDC system, demonstrating how protection, control, and DCCBs behave during fault and the post-fault stage.

In chapter 3, we introduce the modeling and stability analysis of non-linear MMC control methods. The back-stepping control (BSC), sliding mode control (SMC), and advanced model predictive control (MPC), are selected to model the MMC. The detailed modeling process is introduced.

In chapter 4, we provide a detailed introduction to traveling wave fault analysis for MTDC systems. Applying the Peterson equivalent circuit and the TWs theory, the frequency and time domain expressions of the line-mode voltage TWs and pole voltage TWs measured at different relay units are obtained. By constructing transfer functions, this chapter analyzes the characteristics of measured TWs in the high-frequency domain and their influencing factors.

In chapter 5, we detail the traveling wave analysis for MTDC grids in the postfault stage. Applying the pole-mode transform and the Peterson equivalent circuit, the frequency and time domain expressions of the line-mode and pole voltage TWs are obtained under different DC fault scenarios. By constructing transfer functions, the characteristics of measured TWs in the high-frequency domain and their influencing factors are detailed. Based on this, we propose the DWT-based protection scheme and validate its robustness in a four-terminal HVDC model in PSCAD. The protection working steps and thresholds selecting principles are explained in detail. Based on the simulation results, the robustness of the proposed protection algorithm is determined.

In chapter 6, we first derive the expressions for the backward line-mode current TWs containing fault location information. Then, the adaptive multi-step Levenberg-Marquardt (AMLM) algorithm is detailed for solving the nonlinear least-squares problem of parameter fitting. By doing so, the fault location can be estimated based on the fitted coefficient from the sampled discrete data. Furthermore, we verify the proposed method using different MTDC systems modeled in PSCAD and RTDS through numerous simulations. The results indicate that the proposed fault location method has accurate estimation performance.

In chapter 7, we investigate the MMC control Interoperability for different transient processes. The most frequent contingencies of the practical projects, e.g., power flow variation, wind speed variation, and DC/AC grid faults, are simulated in RTDS with eight different control allocation scenarios. Each scenario presents different control capabilities for maintaining system stability. More precisely, the scenarios with non-linear controllers show faster settling time and fewer DC voltage and power variations. Controller switchings are also achieved without bringing large system oscillations. Finally, we provide the optimal controller allocation to cope with system contingencies.

In chapter 8, we summarize the conclusions and provide the answers to the research questions. Besides, a few suggestions for future research are also discussed.

SAMENVATTING

De MMC-gebaseerde MTDC-systemen worden beschouwd als een veelbelovende oplossing voor de elektriciteitstransport over lange afstanden, de integratie van hernieuwbare energiebronnen, en de interconnectie van elektriciteitsnetwerken. Tegenwoordig zijn MMC-gebaseerde MTDC-systemen met succes ontwikkeld in verschillende projecten wereldwijd en wordt verwacht dat ze een belangrijke rol zullen spelen in toekomstige elektriciteitstransport systemen.

Ondanks de voordelen van MMC-gebaseerde MTDC-systemen, doen zich diverse technische uitdagingen voor. Bijvoorbeeld, in geval van een gelijkstroomstoring op HVDC-transmissielijnen, daalt de gelijkspanning aanzienlijk en bereikt de foutstroom binnen enkele milliseconden zijn piekwaarde, wat ernstige gevolgen heeft voor de systeemstabiliteit. Deze foutstromen kunnen elektronica gemakkelijk beschadigen en zelfs leiden tot een ineenstorting van het systeem als storingen niet snel worden verholpen. Daarom is het van vitaal belang om een snelle, selectieve, en betrouwbare beveiligingstechnologie tegen gelijkstroomstoringen te implementeren voor storingsdetectie. Na het oplossen van de storing, is het cruciaal om de exacte locatie ervan te bepalen, zodat defecte secties kunnen worden gerepareerd en het systeem kan worden hersteld. Een nauwkeurige lokalisatietechniek voor gelijkstroomstoringen is dan ook van het grootste belang voor MTDC-systemen, dat elektriciteitsverlies aanzienlijk kan minimaliseren en het herstelproces bij stroomuitval versnellen. Bovendien ontbreekt het aan standaardisatie in MMC-besturing, en wordt de meerderheid van de HVDC-projecten op een leverancier specifieke wijze gebouwd. Op dit moment is het onduidelijk hoe MMC-omzetters van verschillende fabrikanten met elkaar zullen samenwerken. Dit brengt nieuwe uitdagingen met zich mee voor de prestaties van HVDC-beveiliging en MMC-besturing en moeten worden aangepakt om de praktische haalbaarheid van dit systeem te waarborgen, te beschermen, en te versnellen.

Het doel van het onderzoek in dit proefschrift is om de tekortkomingen aan te pakken die nog niet zijn behandeld in de state-of-the-art, met name gerelateerd aan de uitdagingen die ontstaan wanneer gelijkstroomstoringen zich voordoen in MMC-gebaseerde MTDC-systemen. Op deze manier beoogt het onderzoek veelbelovende oplossingen te bieden voor toekomstige praktische MTDC-toepassingen. De hoofdonderwerpen zijn *MMC-besturing & interoperabiliteit, Beveiliging en Storingslokalisatie* voor het MMC-gebaseerde MTDC-systeem. Het proefschrift richt zich op het ontwerpen van een robuust beveiligingsschema, een methode voor het lokaliseren van storingen, en een onderzoek naar interoperabele MMC- regelaars.

De hoofdstukken zijn als volgt georganiseerd.

In hoofdstuk 1 demonstreren we eerst de technische voordelen van MMC-gebaseerde MTDC-systemen in vergelijking met traditionele LCC-HVDC en HVAC-systemen. Vervolgens presenteert dit hoofdstuk opkomende fenomenen en technische problemen die zich kunnen voordoen, wat diverse uitdagingen met zich meebrengt. Hierna volgt een

bespreking van de belangrijkste onderzoeksthema's en de state-of-the-art beveiligings- en besturingsmethoden, inclusief hun voor- en nadelen. Op basis hiervan, worden de kernonderzoeksvragen geformuleerd.

In hoofdstuk 2 introduceren we de kritieke componenten, zoals MMC's en DCCB's, binnen de MMC-gebaseerde MTDC-netten. Hun rollen en werkingsprincipes worden uitgelegd, wat een dieper inzicht biedt in deze complexe systemen. Daarnaast gebruiken we een voorbeeld om de reacties op gelijkstroomstoringen in een MTDC-systeem te analyseren, waarbij wordt gedemonstreerd hoe beveiliging, besturing, en DCCB's zich gedragen tijdens stroomstoringen en in de fase na de stroomstoring.

In hoofdstuk 3 introduceren we het modelleren en de stabiliteitsanalyse van niet-lineaire MMC-besturingsmethoden. De back-stepping control (BSC), sliding mode control (SMC), en advanced model predictive control (MPC) zijn gekozen om de MMC te modelleren. Het gedetailleerde modelleringsproces wordt toegelicht.

In hoofdstuk 4 bieden we een gedetailleerde introductie tot traveling wave storingsanalyse aan voor MTDC- systemen. Door gebruik te maken van de Peterson equivalent schakeling en de TWs theorie, worden de frequentie- en tijdsdomeinuitdrukkingen verkregen voor de lijnmodusspanning en de poolspanning TWs gemeten op verschillende relaiseenheden. Door overdrachtsfuncties te construeren, analyseert dit hoofdstuk de kenmerken van gemeten TWs in het hoogfrequente domein en hun beïnvloedende factoren.

In hoofdstuk 5 gaan we gedetailleerd in op de traveling wave analyse voor MTDC-netten in de fase na de stroomstoring. Door toepassing van de poolmodus transformatie en de Peterson equivalent schakeling, worden de frequentie- en tijddomeinuitdrukkingen van de lijnmodus- en poolspanning TW's verkregen onder verschillende gelijkstroomstoringsscenario's. Door het construeren van overdrachtsfuncties worden de kenmerken van gemeten TW's in het hoogfrequente domein en hun beïnvloedende factoren gedetailleerd beschreven. Op basis hiervan stellen we het op DWT-gebaseerde beveiligingsschema voor en valideren we de robuustheid ervan in een vier-terminal HVDC-model in PSCAD. De werking van de beveiliging en de principes voor het selecteren van drempelwaarden worden uitvoerig toegelicht. Op basis van de simulatieresultaten wordt de robuustheid van het voorgestelde beveiligingsalgoritme bepaald.

In hoofdstuk 6 leiden we eerst de uitdrukkingen af voor de achterwaartse lijnmodusstroom TW's die informatie bevat over de storingslocatie. Vervolgens wordt het adaptive multi-step Levenberg-Marquardt (AMLM) algoritme beschreven voor het oplossen van het niet-lineaire kleinste-kwadratenprobleem voor het afstellen van de parameters. Hierdoor kan de storingslocatie worden geschat op basis van de afgestelde coëfficiënt uit de bemonsterde discrete gegevens. Verder verifiëren we de voorgestelde methode met behulp van verschillende gemodelleerde MTDC-systemen in PSCAD en RTDS via talrijke simulaties. De resultaten geven aan dat de voorgestelde storingslokalisatie methode nauwkeurige schattingsprestaties heeft.

In hoofdstuk 7 onderzoeken we de interoperabiliteit van de MMC-besturing voor verschillende kortstondige processen. De meest voorkomende verstoringen in praktijk, zoals variaties in de richting van vermogensstroom en windsnelheid, en gelijk- en wisselstroomstoringen, worden gesimuleerd in RTDS met acht verschillende besturingsallocatie scenario's. Elk scenario toont verschillende besturingsmogelijkheden om de sta-

biliteit van het systeem te handhaven. Meer specifiek, de scenario's met niet-lineaire regelaars tonen een snellere vestigingstijd en minder variaties in gelijkstroomspanningen vermogen. Ook worden schakelingen van de besturing bereikt zonder grote systeemoscillaties te veroorzaken. Tot slot bieden we de optimale besturingsallocatie aan om met systeemverstoringen om te gaan.

In hoofdstuk 8 vatten we de conclusies samen en geven we de antwoorden op de onderzoeksvragen. Daarnaast worden ook enkele suggesties voor toekomstig onderzoek besproken.

1

INTRODUCTION

This chapter introduces the state-of-the-art knowledge and research gaps in the protection and control of the MMC-based MTDC transmission system. It first demonstrates the technical advantages of this system compared to traditional LCC-HVDC and HVAC systems. Then, this chapter presents newly emerged phenomena and technical issues that may arise, posing various challenges. This is followed by a discussion of the main research topics and the state-of-the-art protection and control methods, including their advantages and limitations. Based on this, the research questions are proposed with meaningful answers to be addressed in this thesis. Finally, the thesis outlines, and contributions are formulated.

1

1.1. BACKGROUND

MODern power transmission systems have evolved significantly over the past decades. The earliest power transmission technology was the High-Voltage Alternating Current (HVAC) system, which was introduced in the late 19th century. As this system could easily transform voltage levels using transformers, it became the backbone of power transmission, enabling long-distance power transfer. Furthermore, HVAC systems facilitate easy interconnection of various power systems, leading to the formation of integrated national and international grids. However, traditional HVAC transmission systems have some limitations, such as lower transmission efficiency over long distances, difficulties in interconnecting asynchronous grids, and matters related to cross-border and underwater/underground transmission. Additionally, under specific circumstances, they are vulnerable to instability problems when interconnecting large power grids [1].

Concerning these facts, Line Commutated Converter-based High Voltage Direct Current (LCC-HVDC) systems were developed in the mid-20th century [2]. LCC-HVDC transmission systems gained popularity due to their ability to transport large amounts of power over long distances with lower losses than HVAC systems. They also provided a practical solution for underwater power transmission and enabled stable interconnection of large power systems without the risk of cascading failures. However, LCC-HVDC systems also face several technical limitations. They require substantial reactive power support for the operation, particularly from shunt compensation devices. Additionally, LCC-HVDC systems cannot start independently, as they need an AC voltage source and lack the black-start capability [3]. They also have a relatively weak capability for regulating reactive power flow, fault ride-through, and grid synchronization. Despite these limitations, LCC-HVDC systems are widely used due to their mature technology, high power transmission capacity, and cost-effectiveness for certain applications.

The limitations of the LCC-HVDC systems have prompted the rapid development of Voltage Source Converter-based HVDC (VSC-HVDC) systems. ABB constructed the world's first VSC-HVDC demonstration project in Hällsjön, Sweden, thus introducing the VSC-HVDC technology in 1997 [4]. The VSC-HVDC transmission offers excellent performance of independent and flexible control of active and reactive power. This makes them an optimal solution for accessing fluctuating renewable power sources and transmitting electricity over long distances.

1.2. SUPERIOR PERFORMANCE OF VSC-HVDC SYSTEM

Compared to the traditional HVAC and LCC-HVDC transmission systems, the VSC-HVDC system provides the following key benefits both technically and economically.

1.2.1. HIGHER EFFICIENCY AND LOWER POWER LOSSES

VSC-HVDC systems are highly efficient, especially for long-distance submarine and underground power transmission. Unlike HVAC systems, VSC-HVDC systems have lower resistance and eliminate reactive power losses caused by the charging and discharging of the line capacitance in AC systems. Additionally, since HVDC systems transport power as a unidirectional power flow, they eliminate the skin effects [5]. Alternating current, however, tends to be concentrated at the surface of a conductor, causing higher power losses

in HVAC systems over long distances. They eliminate the need for a series of phase-shifting transformers and reactive power compensation equipment, typically required in HVAC systems to manage reactive power and control voltage over long distances. Generally, when the distances exceed 600 to 800 km, HVDC becomes more cost-effective than HVAC. [6]. The cost comparison between HVDC and HVAC transmission lines can be found in Figure 1.1.

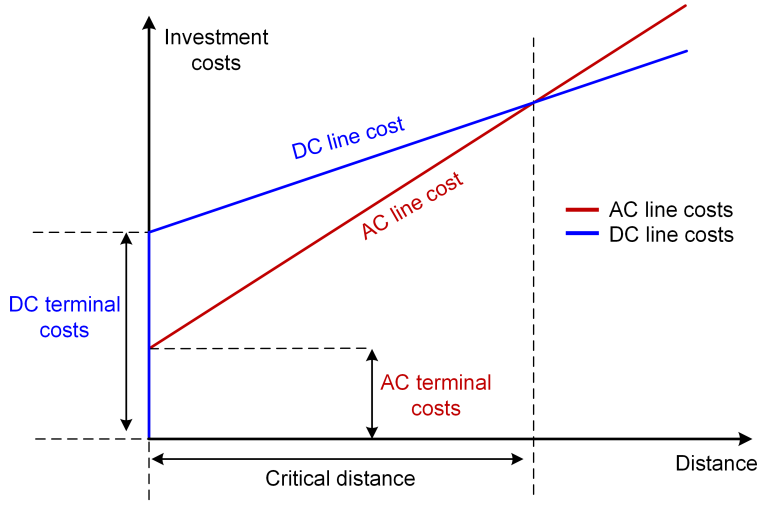

Figure 1.1: Costs comparison between HVDC and HVAC transmission systems.[6]

Unlike LCC-HVDC systems, which require significant reactive power support, VSC-HVDC systems have the ability to control active and reactive power independently. This leads to improved power system stability and, thus, increased transmission efficiency. It allows also VSC-HVDC systems to support the grid in the event of voltage dips, maintaining overall system stability. Although VSC-HVDC systems generally have a slightly higher converter loss compared to LCC-HVDC systems due to the use of insulated-gate bipolar transistors (IGBTs), advancements in converter technology are consistently improving the efficiency of VSC-HVDC systems. Additionally, the use of Pulse Width Modulation (PWM) in VSC-HVDC converters can help reduce the amount of undesired harmonics, thereby reducing the need for specific filters and minimizing associated losses. VSC-HVDC systems do not need to synchronize with the grid frequency, unlike HVAC and LCC-HVDC systems. This improves the overall efficiency by simplifying the control schemes. Moreover, VSC-HVDC systems have better fault ride-through capability, which means they can handle network disturbances more efficiently and contribute to grid stability.

In summary, the overall efficiency results from reduced transmission losses, better long-distance transmission capability, independent control of active and reactive power, and superior fault ride-through capability making VSC-HVDC systems a highly efficient solution for modern power transmission needs.

1.2.2. REDUCED RIGHT-OF-WAY ISSUES

The right of way (ROW) issues in the context of the power transmission system refers to the land over which transmission lines are constructed. Due to the compact size of the VSCs and the absence of heavy overhead lines, VSC-HVDC systems require narrower corridors [5], offering reduced ROW issues compared to LCC-HVDC and HVAC systems. VSC-HVDC requires a smaller physical footprint and less land for installation due to the utilization of compact and modular converters. In comparison, LCC-HVDC stations are larger and require more space. Similarly, HVAC systems require extensive ROW for overhead transmission lines, which can disrupt land use and pose visual and environmental impacts. The compact nature of VSC-HVDC allows for easier integration into existing infrastructure, minimizing the impact on the environment and associated costs. The reduced ROW requirements of VSC-HVDC make it more suitable for constrained or densely populated areas, addressing concerns related to land use, and community impact and reducing the associated costs [7].

1.2.3. LIMITTING SHORT-CIRCUIT CURRENT

VSC-HVDC systems offer substantial benefits over both LCC-HVDC and HVAC systems in limiting the short-circuit currents on the DC side and MMCs. VSC-HVDC utilizes IGBTs that enable the independent and swift control of active and reactive power, thereby reducing the risk of high short-circuit currents [8]. Additionally, VSC-HVDC systems can operate in weak or isolated grids, effectively reducing fault currents.

In contrast, LCC-HVDC relies on a strong external synchronized AC system for commutation, which feeds short-circuit currents into LCC-HVDC during faults, thereby destabilizing the grid. Moreover, LCC-HVDC lacks the black-start capability that VSC-HVDC possesses. This can cause high short-circuit currents during system restarts. Similarly, HVAC systems have inherent limitations in short-circuit current control due to their sinusoidal voltage, current waveforms, and dependency on grid strength. The rapid control and flexibility of VSC-HVDC systems ensure superior limitation of short-circuit currents compared to LCC-HVDC and HVAC.

In summary, the advanced IGBT technology and independent and superior power control flexibility inherent in VSC-HVDC systems provide more efficient management and mitigation of short-circuit currents than the traditional LCC-HVDC and HVAC systems.

1.2.4. BETTER CONTROLLABILITY AND GRID STABILITY

VSC-HVDC systems offer enhanced controllability and stability compared to LCC-HVDC and HVAC systems [9]. VSC-HVDC's superior active and reactive power control facilitates better power flow management and grid stability. The power transmitted can be controlled actively and rapidly by adjusting the converter controls, which is particularly useful for handling power system contingencies, power trading, and integrating fluctuating renewable energy sources. It allows for improved stability and performance of interconnected AC grids, facilitates the transfer of power between asynchronous grids, helps balance load distribution, and enhances grid resilience. It also possesses a 'black start' capability [9], allowing the system to restore power after a complete blackout. These features are not possessed by LCC-HVDC and HVAC systems.

1.2.5. INTERCONNECTION OF UNSYNCHRONIZED GRIDS

VSC-HVDC allows for the interconnection of grids that operate at different frequencies or that are not synchronized.

In comparison, commutation in LCC-HVDC relies on a strong AC system. VSC-HVDC converters can operate even with no or weak AC systems. This advanced control flexibility contributes to the overall grid stability and reliability, making VSC-HVDC a preferred choice for unsynchronized grid interconnections than LCC-HVDC [10]. Unlike HVAC systems, which require synchronization of frequency and phase, VSC-HVDC systems can facilitate the exchange of power between networks operating at different frequencies or phases. With advanced control and the ability to adapt rapidly to changes in network conditions, VSC-HVDC enhances grid stability. Thus, VSC-HVDC is an advantageous choice over HVAC for interconnecting unsynchronized grids. Some typical projects in the practice of VSC-HVDC include the NordLink Interconnector (Norway-Germany), the Eastern Link in the UK, and the North Sea Link (Norway-UK) [11]. There are also several Back-to-back (B2B) projects using VSC-HVDC to connect unsynchronized grids, such as the Bentwisch B2B, Yu-E B2B, and Rio Madeira B2B projects [12].

By capitalizing on these advantages, VSC-HVDC systems offer a flexible and efficient solution for long-distance power transmission, integration of renewable energy sources, and interconnection of power grids. They have been successfully deployed in various projects worldwide and continue to play a significant role in shaping the future of electrical power systems.

1.3. FUTURE DEVELOPMENT OF HVDC SYSTEMS

In recent years, Europe has built many HVDC projects, and these HVDCs are expected to play an increasingly significant role in future power system transmissions.

The North Sea in Europe is a massive, shared wind resource. The map in Figure 1.2 describes how the North Sea might look like and the full opportunities for expanding the North Sea electricity highways towards 2050 [13]. In the near future, a North Sea wind power expansion could be a reality, connecting Germany, the Netherlands, and Denmark via offshore energy hubs and electrical transmissions. Each hub, managed by system operators like TenneT, Gasunie, and Energinet, would have a direct onshore link, ensuring a steady, resilient energy supply for Europe. In the long run, this project could include Belgium, Norway, and the UK, increasing the number of connected hubs and interconnectors, which prompt the energy infrastructure and the potential to explore more of the North Sea's renewable energy. A core design principle is the 'hub-and-spoke,' introducing an innovative concept: the energy hub. These hubs accumulate offshore wind energy and distribute the energy through submarine cables and interconnectors to different countries. The goal is to transform the North Sea into a centralized green power plant serving various energy markets, not isolated plants serving specific nations [13]. Among these, due to the technical and economic advantages of connecting wind power and other renewable energy sources, HVDC will play a very important role in future North Sea energy hubs.

To connect different countries over long distances and efficiently transmit wind energy, it is expected to see a large amount of HVDC infrastructure being built in the North Sea. Specifically, 154 transmission projects, as seen in Figure 1.3, are assessed by 'The

1

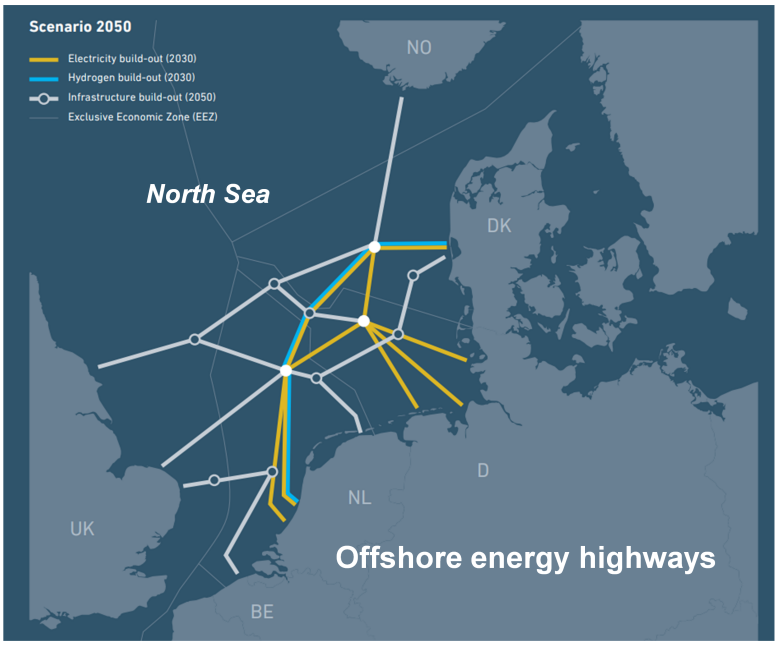

Figure 1.2: North Sea wind energy hub. [13]

TYNDP' [14], which relates to 37 countries. The TYNDP 2020 expects that over 46000 km of new or upgraded cables and lines are needed, of which 19000 km are AC and 27 000 km are DC. It is expected that half of the projects to come into service shortly, while the other half would commission between 2025 and 2035. This offers the advantage of reducing losses when transmitting electricity over long distances while entailing significantly higher costs. When the HVDC links are connected and form a meshed DC grid, they can act as a new backbone grid of the European power system, also referred to as an overlay or super grid. The resulting system will form a hybrid AC/DC network. Examples of this type of HVDC systems are the BorWin, DolWin, and NorNed offshore projects in the North Sea [11].

China's HVDC has experienced significant development in the past 15 years due to the following driving factors. The vast renewable energy resources, particularly wind and solar, are primarily located in remote, less-populated regions, far from major urban load centers. It is known that over 80% of energy resources are distributed in the western and northern regions, while over 70% of energy consumption is concentrated in the eastern and central regions. Considering the expansive geographical landscape and rapidly growing urban population, China faces a unique challenge in distributing its energy resources. This has promoted the development of HVDC projects to effectively transport clean energy across long distances (thousands of kilometers) to meet the growing demand in urban areas. Some existing projects are the Qinghai-Henan project, the Wudongde-Guangxi-Guangdong project, the Zhundong-Wannan project, and many others as reported in [12]. Furthermore, these HVDC projects can also con-

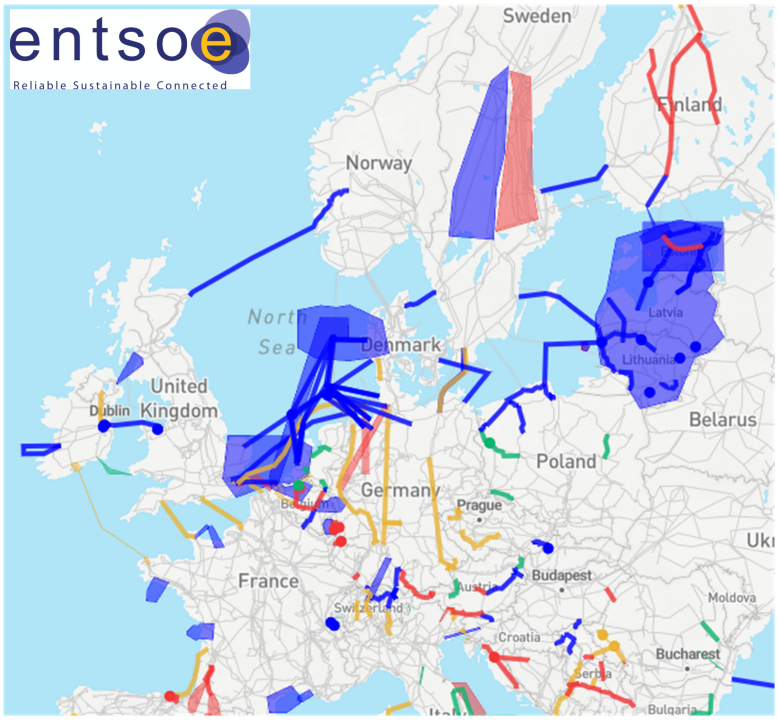

Figure 1.3: TYNDP-E 2020 transmission projects in Europe [14].

tribute to grid stability. They can efficiently manage the intermittent nature of renewable energy sources and ensure a consistent power supply. The flexibility and resilience of HVDC interconnections can improve the reliability of China's grid system. Furthermore, in the larger context of environmental sustainability is China's commitment to reducing its greenhouse gas emissions under the Paris Agreement. The Chinese government is committed to ensuring that by 2030, the proportion of non-fossil energy consumption will reach about 25%, and the carbon dioxide emissions per unit of GDP will be more than 65% lower than in 2005, successfully achieving the carbon peak target before 2030. By facilitating the integration of renewable energy into the grid, these HVDC projects help lower China's carbon footprint and combat climate change. Therefore, HVDC projects are a significant step towards a safe, low-carbon, sustainable, and economical future energy supply and consumption system for China. In 2020, China built the world's largest AC/DC hybrid transmission system, including 30 HVDC/HVAC projects. The total length has reached 35868 km, and more than 430 billion RMB has been invested in these projects.

1.4. RELATED WORKS AND RESEARCH CHALLENGES

In the context described above, the analysis of the MMC-based MTDC grid is the focus of this thesis. Despite the benefits provided by the MMC-based MTDC system, various

emerging technical problems exist. These pose new challenges to the performance of HVDC protection and MMC control and need to be addressed to manage, safeguard, and accelerate the practical feasibility of this system. As such, developing advanced DC protection and fault location strategies, as well as interoperable MMC controllers, is crucial, as conventional technologies are inadequate to maintain the stable operation of the MMC-MTDC system during vulnerable system transient conditions.

The main topics in this thesis are ***MMC control & interoperability***, ***Protection***, and ***Fault location*** for the MMC-based MTDC system, as shown in Figure.1.4.

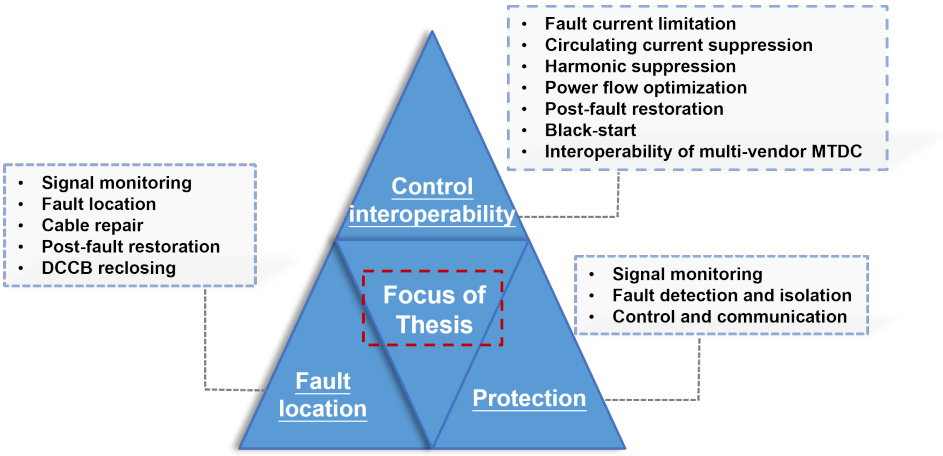

Figure 1.4: Main topics within this thesis.

This section briefly overviews the advantages and shortcomings of existing methods. These provide the starting point and motivation for the research presented in this thesis.

1.4.1. STATE OF THE ART OF HVDC PROTECTIONS

The most common reason for the occurrence of a DC short circuit fault is insulation failure [15]. For example, aging of the cable or mechanical damage can weaken the insulation, which isolates the conductor from the surroundings and creates a path for the current to flow into the ground, resulting in DC faults. When these DC faults are not promptly and accurately located, they can cause significant disruptions, posing a risk of widespread blackouts and substantial economic losses.

In the MTDC grid, different protection zones (taking one terminal as an example) can be configured as shown in Figure 1.5, including AC grid protection, busbar protection, converter protection, and DC line protection. All protection zones are critical for the fault detection and protection of the MTDC system. In the following chapters, it is noted that the focus of this thesis is on DC line protection.

So far, extensive research has been conducted on HVDC line protection. Present methodologies can be classified into two categories: unit- and non-unit protections.

Unit protection relies on communication channels to exchange measurement data between the relays at both ends of a transmission line. Several methods for unit protection have been proposed, including those based on current differential [16], impedance

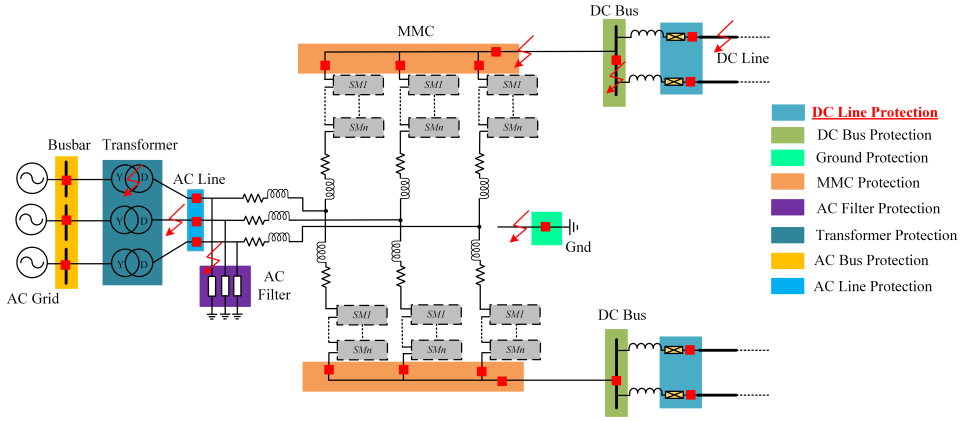

Figure 1.5: DC line protection zone in the MMC-based MTDC system.

differential [17], waveform similarity [18], and others. The key advantage of this protection category is its absolute selectivity, which means that in multi-zone transmission systems, only the protections in the faulty zones operate to detect the faults. However, unit protection requires precise and synchronized measurement data from multiple relay terminals, which can be challenging to achieve over long distances (e.g., 1489 km in the Wudongde project) or in the event of communication network failures. Data exchange between relays causes delays in detecting faults and tripping the DCCBs. Additionally, implementing and maintaining unit protection inquires substantial costs due to the need for specialized equipment and communication channels.

By contrast, another category of non-unit protection does not require a communication channel and can identify the faulty line with only local measurements.

- **Time Domain TW-Based protection**

  In [19], a fault detection scheme is proposed by applying the locally measured rate of change of voltage (ROCOV). To enhance the performance of fault type discrimination, the protection in [20] was achieved by computing the ratio of transient voltage (ROTV). Undervoltage, DC voltage derivative, and directional overcurrent criteria are combined to design the protection scheme [21]. Practical HVDC projects typically utilize the derivative of pole/ground-mode waves, or voltage/current-based TWPs [22], as the primary protections. Although these methods offer fast detection (within 3 ms excluding the DCCBs operations) and eliminate protection dead zones, they heavily rely on TW amplitudes, which impose low sensitivity under HIF and, as such, are susceptible to noise. Therefore, these methods have the advantages of fast detection and no dead protection zone. However, they suffer from poor performances under HIF and noise interference.

- **DC Inductor Voltage-Based Protection**

  In practical MTDC systems, DC limiting inductors are often installed at each line terminal, forming a boundary around the DC transmission line. The protection

schemes in [23], [24] detect faults using the inductor voltage change rate and the inductor voltage differences between the negative and positive poles, respectively. However, the scheme in [23] cannot identify PTG faults, and the method in [24] fails to detect HIF [25]. Based on the modal-domain analysis, the method in [26] adopts the line-mode inductor voltage of the fault detection and zero-mode voltage for fault type discrimination. Compared to time-domain TW-based methods, these methods are easy to implement, robust to noise interference, and do not require a high sampling frequency. However, the sensitivity performance for HIF is still a concern and can be further improved. To conclude, compared with time-domain TW-based methods, the DC inductor voltage based-methods improve the robustness to noise disturbance and require low sampling frequency, however, the sensitivity performances during HIF should be improved. Furthermore, these methods are dependent on the presence of a DC inductor. Besides, the threshold values selection is complicated, especially considering the faults near line terminals.

- **Time-Frequency Analyses-Based Protection**

  DC inductors attenuate specific harmonics and excessive high-frequency components at the line terminals. The significant presence of high-frequency components between the faulty and healthy lines can be utilized to identify faults. Various time-frequency analyses have been conducted for fault detection. Short-time Fourier Transform (SFFT) [27] and Fast Fourier Transform (FFT) [28] based protections have been proposed. Despite their fast processing speed, SFFT and FFT have a limited ability to capture time-frequency information, and a fixed window length and noise restricts SFFT's performance. The Stockwell transform (ST)-based protection [29] achieves high accuracy with a fast response and low computational burden. However, it requires further improvement in robustness against fault conditions, e.c., serious noise interference. The authors of [30], [31] applied Hilbert Huang Transform (HHT) and empirical mode decomposition (EMD) to decompose the measured signals into data sets with different frequency ranges for transient signal analysis. These methods are usually noise-sensitive, and, their resolution can be limited by the selection of intrinsic mode functions (IMFs), making them less suitable for industrial applications. Compared to previous time-frequency analysis methods, the wavelet transform (WT) offers exceptional noise-filtering ability, enabling precise signal decomposition into distinct frequency components. It also delivers excellent time-frequency resolution with fast processing [25]. In [32], the current TWs are analyzed using the continuous wavelet transform (CWT), however, it requires a very high sampling frequency (2 MHz) and additional synchronization devices. Moreover, the method in [32] does not include robustness tests dealing with high-impedance faults. Similarly, previous works [33], [34] use WT to extract transient signal frequency components, and they lack specific fault type discrimination in their protection schemes, and the sensitivity against HIF, maximum detectable 200 Ω, in [35] can be improved.

To conclude, yet HVDC protection methods need to be addressed and enhanced and this is particularly important for HIF fault detection, fault type identification, and noise

interference elimination.

Table 1.1: Overview of the existing HVDC protection methods

Methods	Strengths	Drawbacks
Unit protections		
Current differential [16] Impedance differential [17] Waveform similarity [18]	• Easy to implement • High selectivity	• Synchronized measurements • Long time delays • High costs
Non-unit protections: Time domain TWs-based methods		
Rate of change of voltage[19] Ratio of transient voltage[20] • Under-voltage • DC voltage derivative • Directional current [21] Voltage/current TWs [22] Pole/ground-mode TWs [22]	• Easy to implement • High selectivity • Simple and fast • No dead zone	• Susceptible to noise • Low selectivity • Low sensitivity to HIF • High sampling frequency
Non-unit protections: DC inductor voltage-based methods		
Inductor voltage change rate [23] Inductor voltage differences [24] Line/zero mode inductor voltage [26]	• Easy to implement • High selectivity • Simple and fast	• Susceptible to noise • Low sensitivity to HIF • Thresholds design
Non-unit protections: Time-frequency analyzing-based methods		
SFFT-based protection [27] FFT-based protection [28] ST-based protection [29] HHT-based protection [30] EMD-based protection[31] CWT-based protection [32] DWT-based protection [33], [34]	• High selectivity • Fast detection • High reliability	• Easy to implement • Low time-frequency resolution • Restricted to time-window length • Susceptible to noise • Computation burden • Thresholds design
Non-unit protections: Other methods		
MAD-based protection [36] MRMG-based protection [37]	• High reliability • Fast detection	• Susceptible to noise • Low selectivity • Low sensitivity to HIF • Computation burden

1.4.2. STATE OF THE ART OF FAULT LOCATION METHODS

Existing research on HVDC fault location mainly includes natural frequency-, fault analysis-, active injection-, and traveling wave-based methods.

- **1. Natural Frequency-Based Method**

  Natural frequency-based methods are proposed in [38]–[40]. These methods first analyze the relationship between natural frequency, fault distance, and reflection coefficient. The dominant natural frequency of voltage TWs is then used to calculate the velocity of the TWs and the reflection coefficient for estimating the fault point. Methods as such utilize the MUSIC or PRONY algorithm [38]–[40] to ex-

tract the natural or specific frequency components contained in post-fault voltage/current TWs. Generally, these methods require a high sampling frequency and fail to discriminate the fault location when the fault point is close to the line terminal due to the "dead zone".

- **Active Injection-Based Method**

  The active injection-based methods are proposed in [41]–[43]. In such methods, a specific detecting signal is actively injected at the line terminal, and the characteristics of the reflected signals from the fault point are used to identify the fault location. However, an additional device or a control loop for signal injection is generally required. Apart from this, the injected signal may cause ac power fluctuations due to the coupled AC/DC systems. Moreover, the accuracy of these methods can be affected by the fault resistance and the size of the DC inductor. These methods are with a limited application to only monopolar HVDC systems with ground returns as both healthy and faulty poles are connected to the same MMC [43].

- **Fault Analysis-Based Method**

  Fault analysis-based methods are introduced in [44], [45]. In these methods, the voltage and current TWs expressions are computed at any point, thereby locating the fault based on the fault characteristics of measured voltages and currents TWs. The authors in [44] reconstructed the current signal using a curve-fitting approach, and eliminating the effect of the distributed capacitance. The fault distance is determined by estimating the line inductance. In [45], a simplified $R-L$ representation is proposed to model a detailed frequency-dependent transmission line by calculating the $R-L$ parameters for fault location. These methods do not require a high sampling frequency to capture the wavefront of TWs. However, they are based on the aggregated transmission line model, which neglects the propagation process of TWs. As a result, the accuracy of the fault analysis method depends on the parameters of the transmission line. As such, the accuracy of these methods cannot be guaranteed when applied to long transmission distances.

- **Traveling Wave-Based Method**

  Traveling wave-based methods are characterized by high precision and reliability, and they are not affected by the value of the fault resistance. By using TW's law, one can establish the mathematical relationship between the propagation time, velocity, and fault distance of the TWs. There are two categories of TW-based methods: single-ended and double-ended. Despite the performance of double-ended methods [46], [47], they may have some inherent shortcomings, e.g., the measured TWs signals at different relay units must be exchanged, which can be affected by communication interruption or delays. Thus, this method can only be applied in systems with accurate signal measurements and high-fidelity synchronized communication channels, which increases the overall investments and the risk of data damage during the synchronization. For the single-ended methods presented in [32], [48]–[51], the fault distance is determined based on the time interval between two consecutive wavefronts of the fault-induced TWs. Thus, an extremely high sampling frequency (e.g., [51] uses 500 kHz) is needed to estimate the TW's precise

velocity and injecting/reflecting points. Besides, the accuracy of these methods is susceptible to noise intervention.

Based on the provided overview, it can be seen that there is still a need for the development of an accurate fault location algorithm applying communication devices and estimations of the TW velocity. Moreover, the algorithm should be robust against noise, detect HIF and use a low sampling frequency.

1.4.3. STATE OF THE ART OF INTEROPERABLE MMC CONTROLS

The future MTDC grids will be modular[52]. The practical project InterOPERA [52] aims to achieve the interoperability of multi-vendor HVDC grids by developing all relevant frameworks and performing the full scope of necessary activities to implement a real-time physical demonstrator by 2030. By doing so, in future multi-vendor MTDC-based super grids in the North Sea, different components like converters, controllers, protections, and CB devices will be supplied from different manufacturers, each with its own control algorithms and communication protocols. These components will be integrated seamlessly and operate together. However, if these different modular systems cannot be compatible to each other or interpret each other's signals correctly, it could lead to inefficient operation or even can cause failure of the MTDC system.

Specifically, control interoperability refers to the ability of MMC controllers, each possibly designed by different vendors, to operate together and interact in a compatible manner. Control interoperability becomes crucial in the future, given the increasingly complex and interconnected features of the MTDC systems.

Several benefits can be achieved when control interoperability is accomplished, including enhanced system stability, efficiency, and flexibility. Furthermore, interoperable controls can better manage the dynamics between different components, maintaining grid stability even under system transients. It allows different control systems to work together smoothly and guarantees optimal controller allocation, leading to greater overall system stability [53]. It also allows for integrating new vendor's technologies without significantly disrupting the existing system. Finally, the MMC controller interoperability helps expand the system by understanding how additional converters interact with existing ones.

However, at the current stage, it remains a significant challenge to achieve control of interoperability in the MTDC system. A thorough performance assessment of the different controllers for the MMC units interacting through an MTDC using detailed models is needed.

The emphasis of the presented thesis is on a comprehensive assessment of the interaction of the MMC units' inner and outer control functions under classical PI methods in [54] and non-linear control methods [55]. The controller interoperability study within this thesis is analyzed following non-linear control methods:

- Model Predictive Control (MPC) has been known for the last 20 years in mechanical and aerospace applications. The Multiple Input Multiple Output (MIMO) characteristics, robust and fast response made these algorithms popular in power electronic applications where the MPC is classified into two major categories; Direct and indirect MPC [56]–[58]. This classification is made based on the presence or

absence of a modulator. In the literature, most indirect MPC has been investigated for HVDC - MMC application in offline simulations. Thus, the dependence on-the time is removed. Further, there is little research conducted on the MPC-based MMC-MTDC system, and the interaction of the MPC with the different control has not been analyzed.

- Back-Stepping Control (BSC) has a systematic and recursive design methodology, which links the design of the Lyapunov function with a feedback controller and ensures global asymptotic stability. The BSC approaches outlined in [59], [60] utilize the energy controller to deliver the set-point to the grid current controller. A disturbance-tracking-based backstepping control is proposed in [61]. However, the feasibility of the aforementioned methods in the MTDC system needs further investigation. The authors of [62] designed the BSC method based on the simplified transmission model, and the interaction of wind farms is also considered. However, due to the imprecision of the model, the control's effectiveness needs to be further verified.

- The Sliding Mode Control (SMC) has the merits of high robustness against system uncertainties and prompt transient response. Recently, the second-order SMC (SOSMC) became popular since it not only preserves the robustness properties of the classical SMC, but also overcomes the shortcomings of high-frequency chattering and infinite time convergence, of which the most feasible solutions for practical projects are the twisting controller and super-twisting sliding mode controllers (STSMC) [63], [64]

Since the control settling interoperability of the MMC-based MTDC system has not been achieved previously, this thesis presents the original first study interoperability analysis of various controllers in an MMC-based MTDC system via different system transients tests. The findings have profound significance for the cooperation between different MMC controllers in practical vendor-specific MTDC engineering.

1.5. RESEARCH QUESTIONS

The research conducted in this thesis is motivated by the objectives that have not been addressed in the state of the art, mainly related to the challenges arising when DC faults occur in the MMC MTDC grids. The research deals with designing a robust protection scheme, a fault location method, and an investigation of the interoperable nonlinear MMC controllers which will provide stable system operation during and after the fault. The proposed methodologies aim to address the shortcomings and limitations of presently available methods and, as such, could provide promising solutions for future practical applications.

To obtain in-depth results and clear the research path, the following **key research questions** are defined:

Q1: What are the strategies to achieve control interoperability in the MTDC grid, considering vendor-specific control systems? Additionally, how can these strategies be evaluated and optimized for overall grid performance and stability?

In recent years, researchers have proposed various advanced MMC controllers to enhance the performance of classical MMC controls. However, there is a lack of standardization in MMC control, and the majority of HVDC projects are constructed in a vendor-specific manner. As of today, it is unclear how power electronic converters from different manufacturers will interoperate and what information should be exchanged between control and protection units. The challenges and difficulties of realizing the interoperable control in MTDC are summarized in Table 1.2.

Table 1.2: Challenges for achieving control interoperability in MMC-MTDC system

Challenges	**Difficulties**
Control design	• Control performance, response time, stability. • Controller hierarchy
Standardization	• Lack of standardized testing and validation procedures
Complex system dynamics	• Coordinate all the controllers work effectively • Different vendors in different converters (e.g., MMC1 uses ABB and MMC2 uses SIEMENS)
Control coordination	• Coordinate all the controllers from different vendors
Voltage/current balancing	• Using different control algorithms and hardware
Communications	• Lack of communication protocols and standards • Difficult to exchange data and commands effectively
Maintenance and Upgrades	• Ensure reliability and safety • Coordination between multiple vendors • Ensuring the interoperable control systems
Hardware incompatibility	• Incompatibility of vendor hardware. e.g., sensors

Operational incompatibility among different MMC technologies may present unprecedented phenomena, as evidenced in a few recent preliminary studies. In [65], slower abnormal oscillations are reported due to the interaction of multi-vendor VSCs, which can be damped by DC voltage control. The lower bandwidth of the converter's outer voltage control loop significantly affects rotor angle stability during minor disturbances. Moreover, this control loop greatly influences voltage stability. In contrast, the inner current control loop can lead to fast-interaction, converter-driven stability issues. These problems can be mitigated by utilizing non-linear controllers. Nevertheless, it is very challenging to thoroughly assess the performance of different controllers interacting through an MTDC system using detailed models. Consequently, interoperable MMC control strategies are of utmost importance for further development of the multi-vendor MTDC systems.

Q2: How can we develop robust protection schemes to detect DC faults promptly, and how can we ensure their selectivity, sensitivity, and reliability?

To accelerate the practical feasibility of HVDC systems, advanced DC protection technologies play an important role.

For a protection scheme, 'speed, sensitivity, reliability, and selectivity' are the four key requirements to assess its robust performance.

Firstly, a protection scheme should be able to detect faults promptly, including the faulty line and fault type, typically within two milliseconds, and then send a tripping command to the DC circuit breaker. Failure to isolate the fault rapidly can result in a swift rise of the fault current, bringing significant difficulties to the DCCB to interrupt it and placing substantial stress on the converter's valve tolerance. In the most severe cases, the system may risk cascading failures and collapse. Besides, the protection algorithms involved in the data processing should be simple and fast to meet the speed requirement. Otherwise, it will increase the computational burden and time delay for the hardware processor. Secondly, in MTDC systems, there are multiple DC line areas, and the DC protection is typically installed at the line terminal. When a fault occurs on one line, the fault signals measured by the protection on the adjacent line are relatively close, especially when the DC fault is near the end of the line. As such, it is quite challenging to identify the faulty area. Therefore, DC protection is required to have selective capability in fault detection. In addition, due to the frequent presence of high-resistance faults (HIF) and the significant and random noise interference in signal measurements, it is very challenging to design protection schemes, especially the selection of threshold values to guarantee sensitivity in detecting these faults. Lastly, the protection device must always be reliable. Regardless of the DC fault scenario and system disturbances, the protection, when required to operate, must be correctly activated and provide a trip command to the DC circuit breaker on time. Conversely, when the operation is not required, the protection device must avoid false operations. Unreliable operations under these conditions could seriously affect system stability, such as removing healthy lines or failing to isolate faulty lines.

For this reason, it is quite challenging to design a suitable protection scheme for the complicated MTDC system. These four criteria are normally not met with the same burden, and as such, the performance of the developed protection scheme has some limitations. Thus, it is always a trade-off to balance the performance of the protection scheme. This brings the question: How to bring these requirements to a higher level so that the protection scheme increases its robustness from the perspective of 'speed, sensitivity, reliability, and selectivity '?

Q3: Which methodology can be used to develop accurate and refined fault locators?

Following **Q2**, the protection only identifies the faulty area and types on the protected DC lines. DCCB will disconnect the entire faulty line. However, this only prevents the fault from damaging the converters and collapsing the system. In practice, it is important to know the exact fault location to repair the faulty sections, especially for the submarine/underground cables.

As such, developing improved models for precise DC fault locations is important for the secure operation of the MTDC grid. An accurate fault location algorithm reduces the need for exhaustive searches along the cable, minimizes repairing time, and extends the reliability and lifetime of the cable and associated grid infrastructure. Understanding where and why a fault occurred can also help in designing the system in a way to avoid the occurrence of similar faults in the future.

1.6. THESIS OUTLINE

The thesis structure is illustrated by the research flowchart shown in Figure 1.6. The main contents discussed in each chapter of the thesis are outlined as follows:

- **Chapter** 2 deals with a comprehensive introduction to the modeling and building of the MMC-MTDC system. Initially, the chapter provides a detailed examination of the principles of critical components, such as MMCs and DCCBs, within the system. Next, this chapter concludes with an in-depth analysis of the system's responses to faults.

- **Chapter** 3 firstly introduces the MMC and its state-space modeling in detail. Afterward, this chapter models the most commonly adopted proportional-integral (PI) control and other non-linear controllers, e.g., MPC, BSC, and SMC for the constructed MMC.

- **Chapter** 4 describes the basic electrical TWs theory. Based on the MTDC simulation model, an equivalent circuit of the system is constructed following a DC line fault. This circuit is used to analyze the characteristics of the voltage and current TWs both in time and frequency domains. Detailed expressions of TW signals detected at the relay units are then determined. This chapter sets the basis of the proposed DC protection methods and fault location techniques that will be addressed in the subsequent chapters.

- **Chapter** 5 firstly analyzes the equivalent circuit of the system following a DC fault. Specific time-domain and S-domain expressions for the voltage and current traveling waves, measured at the relay units, are derived. Using these results, the characteristics of the high-frequency components are investigated in both the line mode and pole voltage. Next, a detailed analysis of the high-frequency components in these voltage TWs is presented. Furthermore, this chapter introduces a novel DC line protection scheme with an explanation of the principles for selecting protection threshold values. The proposed protection scheme is simulated using the PSCAD simulation platform under various fault conditions. Finally, we conduct a comparative analysis with other DC protection methods to demonstrate the superiority of the proposed scheme.

- **Chapter** 6 introduces a new single-ended DC fault location method utilizing backward line-mode current TWs of MTDC systems. It begins by presenting an approximation that the backward line-mode current TWs can be represented by an exponential function with a parameter that includes the fault location. Following this, the Adaptive Multistep Levenberg Marquardt (AMLM) algorithm is employed for parameter fitting, and the computation process of this algorithm is comprehensive. The chapter concludes with a demonstration of the effectiveness of the proposed method through performance validation, which is carried out on both PSCAD/EMTDC and RTDS platforms.

- **Chapter** 7 deals with the interoperability simulations in an MTDC system in an RTDS environment. The most frequent transients of the practical projects, e.g.,

power flow changing, wind speed changing, and DC/AC grid faults, are simulated through eight different scenarios. Each scenario presents different control capabilities in maintaining system stability, more precisely, the scenarios with nonlinear controllers show faster settling time and fewer DC voltage and power variations. Controller switchings are also achieved without bringing large system oscillations. This chapter provides the optimal allocation strategy of controllers to cope with system transients.

- **Chapter** 8 summarizes the conclusions of the thesis and recommends several future research directions.

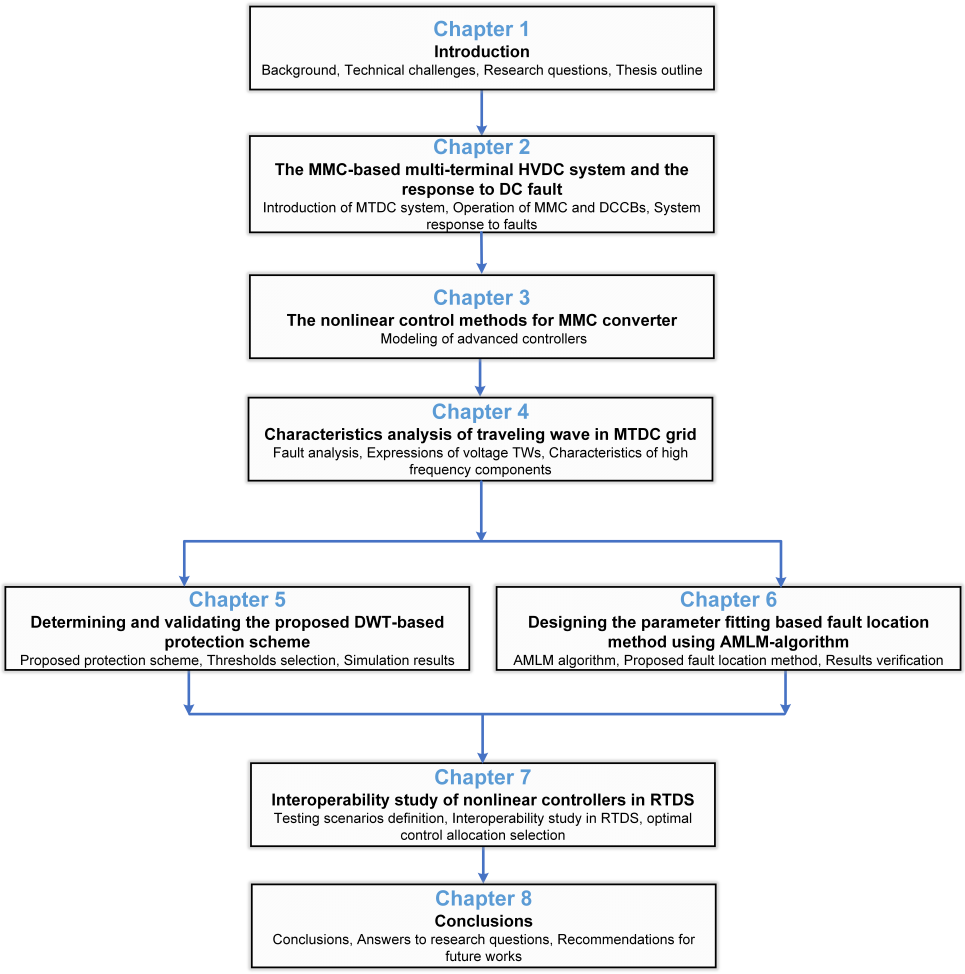

Figure 1.6: Chapter's outline within the thesis

2

THE MMC-BASED MTDC SYSTEM AND DC FAULT RESPONSE

This chapter deals with a detailed introduction to the critical components, e.c., MMCs and DCCBs, within the MMC-based MTDC grids. Their roles and working principles are explained, providing a deep understanding of these complex systems. In addition, an example is shown to analyze the DC fault responses in an MTDC system, demonstrating how protection, control, and DCCBs behave during fault and the post-fault stage.

Parts of this chapter have been published in [53], [66].

2.1. OVERVIEW OF THE MMC-MTDC SYSTEMS

2.1.1. BENEFITS OF MULTI-TERMINAL CONNECTIONS

Converter stations utilizing VSC-HVDC technology can be implemented in various configurations, primarily including the following: monopolar, bipolar, point-to-point connections, back-to-back connections, and multi-terminal connections. MTDC systems provide several benefits over traditional connection methods.

Firstly, the MTDC system exhibits superior flexibility in controlling power flows, capable of promptly directing power according to changes in demand or supply. It also facilitates the integration of renewable energy sources like wind and solar. These sources are often geographically dispersed and intermittent, and the MTDC system efficiently links and manages their fluctuating generation. The stability of the connected AC grids is significantly improved through the MTDC system by offering additional power flow paths, enabling power transfer control, and better voltage control. Moreover, MTDC systems facilitate the interconnection of asynchronous multi-grids and renewable resources, thus broadening the geographical scope of power exchange and trading. Finally, MTDC systems enhance resiliency against faults by offering alternative power flow paths, thus guaranteeing a consistent power supply even when one line is disconnected.

The above benefits make the MMC-based MTDC systems regarded as one of the most cost-effective and promising solutions for long-distance, bulk power transmission and the integration of large-scale renewable energy sources and building hybrid HVDC/HVAC systems [66].

2.1.2. ONSHORE MMC-BASED MTDC GRIDS

MMC-based MTDC grids comprise various critical components, each serving a unique and indispensable role.

Based on the location or placement of the system, the MMC-based MTDC system can be divided into two main parts: onshore and offshore grids. The onshore part refers to its installation on land or near the shore, and it is commonly applied when connecting HVDC transmission lines to the main AC grid. The offshore part involves its installation at sea, usually integrating with large offshore wind farms or other offshore energy sources.

A typical onshore MMC-based HVDC grid is shown in Figure 2.1.

In the context of renewable energy, onshore MMC-based MTDC grids integrate large-scale renewable power sources in geographically dispersed areas into the main grid. The MMC operates in a grid-following mode, designed to follow the voltage and frequency of the grid. It acts as a controlled current source. This means that the MMC converter relies on the grid to provide a stable reference for its operation. The converters are not responsible for voltage and frequency regulation; Instead, they inject or absorb active and reactive power. The control objectives of onshore-MMCs are mainly to regulate the DC link voltage and to control the power exchange with the AC grid [67].

The converter station studied in this thesis is the half bridge (HB)-MMC, which cannot clear faults like full bridge (FB)-MMC. Therefore, the DC protection algorithms are implemented at the relay units (indicated by the red block) to monitor the electrical signals and determine whether a fault has occurred. Once the fault is detected, the pro-

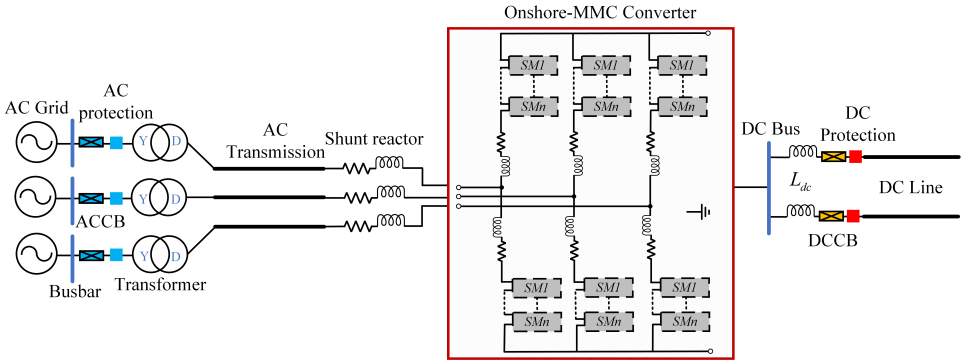

Figure 2.1: Onshore MMC-based HVDC grid.

tection devices send the command signals to DCCBs. DCCBs then interrupt the fault currents and isolate the faulty line. To suppress the rising rate and peak of the fault current, the DC inductor L_{dc} [66] is usually installed at the line terminal. The L_{dc} can also be considered as a filter and can be used as a boundary component for the protections to design the protection algorithm. The actual number of converter stations, the control strategies, the connection methods of the DC lines, and the installation locations of the DC inductors depend on the specific requirements of the MTDC project.

On the AC side, there is usually a shunt reactor at the outlet of the MMC station. The shunt reactor [68] is used to regulate the voltage. During low-load or no-load conditions, the shunt reactor absorbs reactive power, which helps maintain the voltage within acceptable limits. It also helps generate or compensate the reactive power according to the system's needs. Besides, the shunt reactors can reduce the harmonics in the system by absorbing the harmonic currents generated by the converter stations, improving the power quality in the AC grids. Finally, the renewable energy is delivered to the distribution network and user side through the HVAC transmission network and transformers.

For an MMC-based MTDC following typical AC short-circuit faults, the balance of the AC grid is broken. Whether it is a grid-following or grid-forming MMC, the AC side voltage, active/reactive power, and frequency are closely linked to the inherent controllers of the MMC, and the normal operating condition of MMC converters will no longer exist. When the faults in the AC grid cannot be cleared quickly, the faults will spread rapidly to the converter station, causing the converter station to block. The DC protection may also detect faults due to low voltage or overcurrent, and the DCCBs will remove the corresponding DC line. Ultimately, this evolves into a cascading fault on both the AC and DC sides. Hence, the AC protection devices and AC circuit breakers are also essential to detect possible faults in the AC network and will play a significant role in preventing blackouts and cascading faults resulting from the AC side fault.

2.1.3. OFFSHORE MMC-BASED MTDC GRIDS

Offshore grids are located at sea, typically serving to connect offshore wind farms to onshore grids. The main technical features and operation of both onshore and offshore

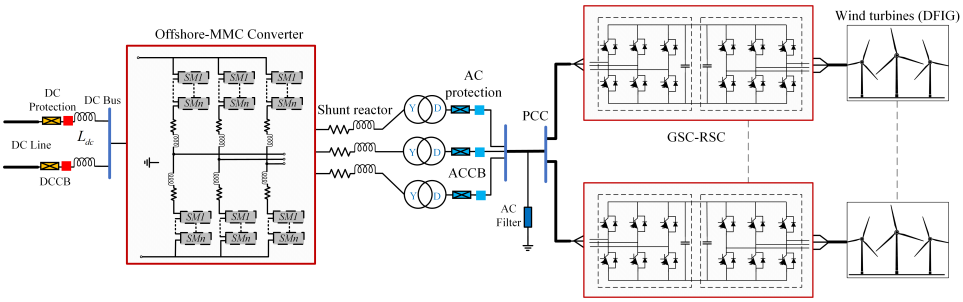

Figure 2.2: Offshore MMC-based HVDC grid.

MTDC grids are generally similar. However, the operational and control modes of the MMC stations and the characteristics of the AC grid are the primary areas of difference.

More specifically, the MMC in offshore grids primarily operates in a grid-forming mode acting as the controlled voltage source. This contrasts with MMCs in onshore grids, which typically follow the grid. Instead, it establishes the voltage and frequency reference for other grid-following MMCs to follow. As such, this capability becomes important when integrating high penetrations of power electronic-interfaced offshore wind power plants, where the offshore MMC converter needs to support the grid. The control principle of onshore and offshore MMCs will be introduced in detail in the following section.

Moreover, to integrate offshore wind farms, particularly those employing Doubly-Fed Induction Generators (DFIG), the back-to-back Grid-Side Converters (GSCs) and Rotor-Side Converters (RSCs) are typically utilized [69]. This setup is illustrated in Figure 2.2. The GSC connects the wind turbine system and the DC busbar, thereby regulating the stable DC bus voltage to a constant level, achieving sinusoidal grid current waveforms, and adjusting the power factor close to unity [70]. It also controls the active power flow between the wind turbine and the converter side. In doing so, it helps manage power exchange with the grid. Furthermore, the GSC facilitates reactive power compensation at the Point of Common Coupling (PCC) by providing or absorbing reactive power as needed. The RSC is directly connected to the rotor of the DFIG. It modulates the rotor current to manage the rotor speed, enabling the wind turbine to operate at its maximum power point under varying wind speeds. By controlling the rotor current, the RSC regulates the active and reactive power supplied by the rotor [67], [71].

2.2. WORKING PRINCIPLE OF MMC

The MMC, a particular topology for VSCs, has become a favored choice in recent years due to several key advantages.

Its modularity and scalability are notable strengths, with the system's structure allowing easy scaling by adjusting the number of Submodules (SMs) per arm to adapt to different voltage levels. Coupled with its PWM-based switching operations, the MMC operates with higher efficiency and lower losses than other VSC converters. Further, it can generate high-quality, near-sinusoidal voltage waveforms with limited harmonics, reducing

the need of harmonic filters and paving the way for more compact, straightforward, and cost-effective system designs. The MMC does not need large DC-link capacitors since the capacitor voltages in the SMs can be independently controlled, offering enhanced system performance and flexible control. Its modular design enhances fault tolerance and redundancy, allowing faults in individual modules to be bypassed or isolated without shutting down the whole converter, ensuring service continuity, increased reliability, robustness, and reduced maintenance costs. Although MMC technology requires more complex design and control strategies, the above benefits make it an increasingly preferred solution for many modern HVDC applications.

2.2.1. MMC BASIC STRUCTURE AND COMPONENTS

In this thesis, the main focus is on the HVDC protection study. As such, the type of HB-MMC is used for study purposes. Figure 2.3 depicts the classical structure of the HB-MMC converter and the stationary reference frame using vector representation [53].

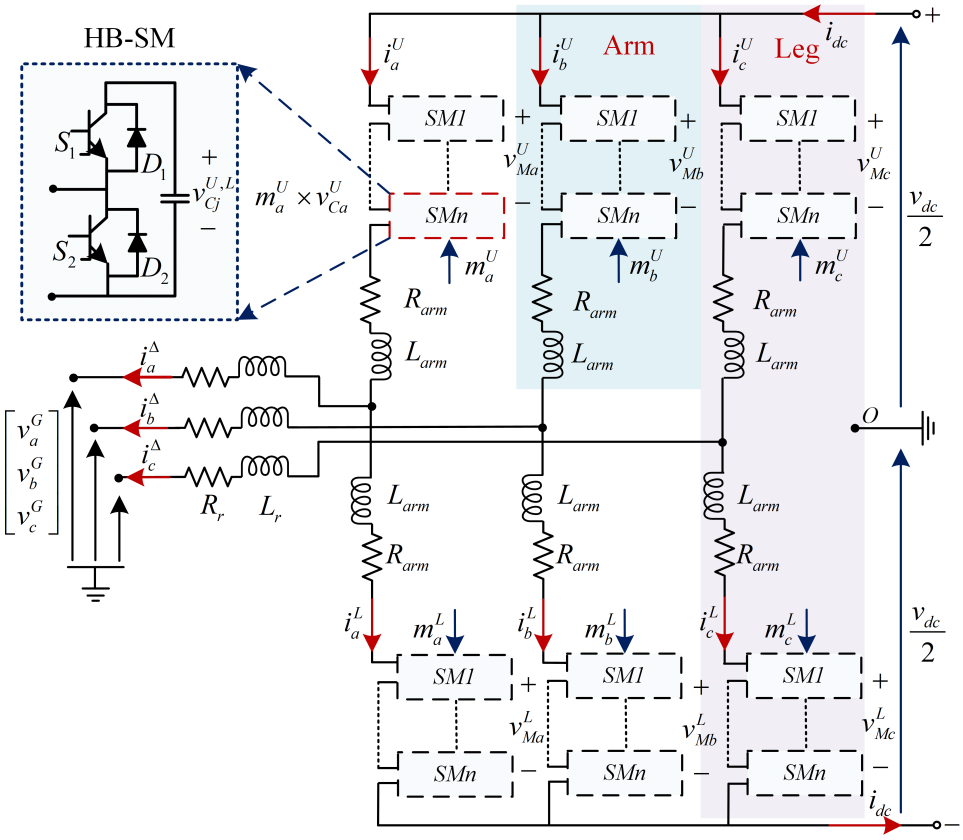

Figure 2.3: Structure of HB-MMC converter.

In Figure.2.3, two identical arms are connected to the upper (denoted as *U*) and

lower (denoted as L) arms, forming one leg of each phase $j \in \{a, b, c\}$. N represents the number of half-bridge SMs of each arm, and the L_{arm} and R_{arm} denote the equivalent series arm inductance and resistance, respectively. The AC-side interface is assumed as an equivalent resistance and inductance, denoted as R_r and L_r, respectively. Here, the L_r is also known as the shunt reactor, of which the primary function is to absorb the reactive power. It is used to increase the overall system's power factor and help maintain or control the voltage. The R_r is generally a small value and can be neglected.

The most essential element of the MMC structure is an SM. Each half-bridge SM consists of four semiconductor switches (S_1,S_2,D_1,D_2) with an anti-paralleled capacitor, of which the voltage is recorded as $v_{Cj}^{U,L}$. Each SM is responsible for converting DC voltage to AC voltage or vice versa. The operation of these SMs is crucial for the overall functionality of the MMC. As seen in Figure 2.4, the working conditions of SMs include the bypassed mode, active mode, and blocked mode [72]. To be specific,

- **Active Mode**: During normal operation, the SMs are actively involved in the voltage conversion process. The pulse-width modulation (PWM) regulates the output voltage. The SMs capacitors are charged and discharged in response to the PWM signals, allowing the MMC to generate desired voltage levels. If the current direction (denoted as the blue arrow in Figure 2.4) is positive, the capacitor charges, and in the negative current direction, the capacitor discharges. In both cases, the SM output voltage will be equivalent to the SM capacitor voltage. In this mode, the current flows through S_1 or D_1 and the capacitor, and the SM output voltage is the capacitor voltage v_c.

- **Bypassed Mode**: In this mode, the SMs are effectively disconnected from the MMC circuit and bypassed. This condition is typically used during start-up, shutdown, or certain fault conditions to allow current to flow through bypass paths, avoiding excessive voltage across the SM. The capacitor is not discharged or charged as the capacitor is isolated from the system. The current flows through S_2 or D_2. The SM output voltage will be zero regardless of the current direction.

- **Blocked Mode**: In this mode, the IGBTs of S_1,S_2 in SM are effectively disabled or blocked from participating in the voltage conversion process. This condition might be used during the initial capacitor charging state or for protection purposes during AC or DC faults to isolate a problematic SM and protect the MMC from further damage. The current can only flow through these two free-wheel anti-paralleled diodes D_1,D_2, and the current direction depends on the external circuit. The capacitor can only be charged through diode D_1 when the SM output voltage is higher than the capacitor voltage. Besides, the capacitor cannot discharge, so this blocked mode is only possible before pre-energization.

2.2.2. CONTROL HIERARCHY OF MMC

In this thesis, the inner/outer loops of the control hierarchy [53] for the MMC are adopted. The outer loop provides the reference current, which depends on the MMC's working mode, such as DC voltage/active power control and AC voltage/reactive power control

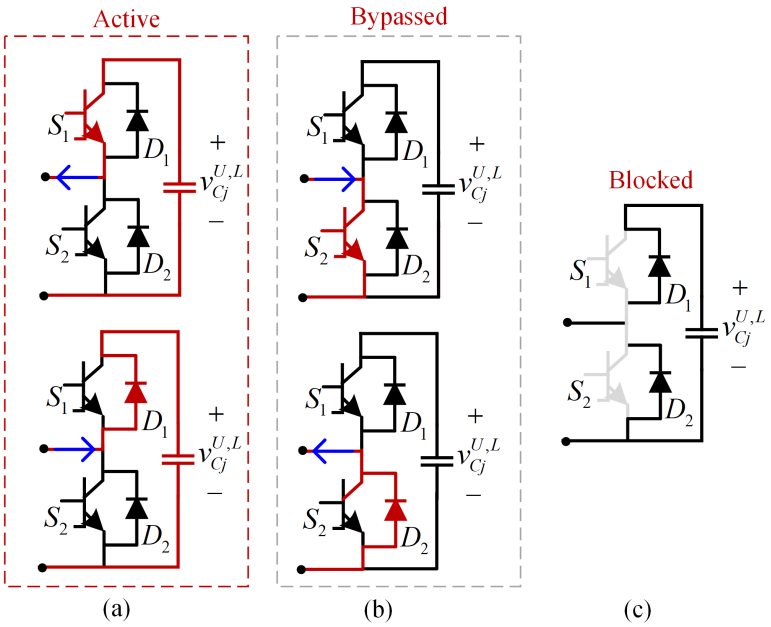

Figure 2.4: SMs working mode. (a). active mode; (b). bypassed mode; (c). blocked mode.

modes. Based on the reference signals from the outer loop, the inner loop control provides voltage reference signals for the capacitor voltage balancing controller. This controller generates the SM firing signals using PWM and ensures that the voltage of each cell capacitor remains constant and is in line with the predetermined rated value. The schematic of the MMC control loops is depicted in Figure 2.5.

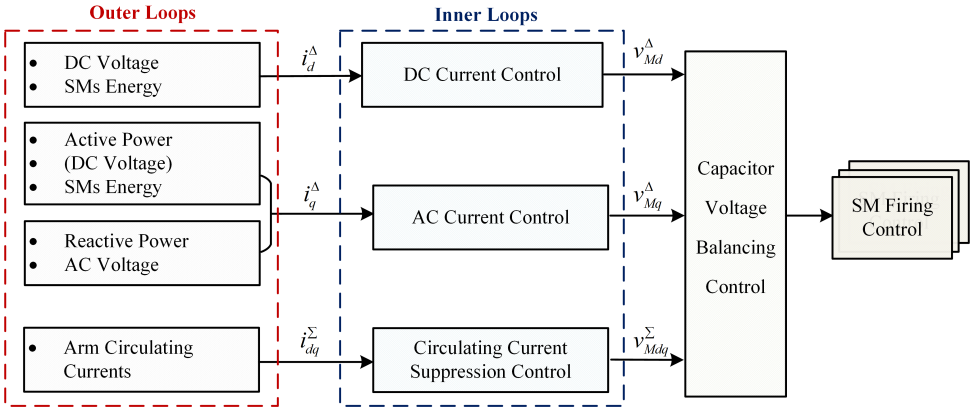

Figure 2.5: MMC outer and inner control loops

2.2.3. STATE-SPACE MODELLING OF MMC IN $\Sigma-\Delta$ REPRESENTATION

In Figure 2.3, SMs are considered with their average equivalents, and thus, the modulated currents $i_{Mj}^{U,L}$ and voltages $v_{Mj}^{U,L}$ of the upper and lower arm of a generic phase j, can be expressed as follows:

$$v_{Mj}^{U,L} = m_j^{U,L} \cdot v_{Cj}^{U,L}, \qquad i_j^{U,L} = m_j^{U,L} \cdot i_{Cj}^{U,L} \tag{2.1}$$

where $m_j^{U,L}$ are called the modulation indices of the upper and lower arms for all three phases. The values of $v_{Cj}^{U,L}$ and $i_{Cj}^{U,L}$ refer to the voltages and currents of the equivalent capacitance in the upper and lower arm.

As mentioned before, the adopted state-space modeling uses the $\Sigma-\Delta$ representation instead of the commonly used Upper-Lower form. For the MMC configuration in Figure 2.3, the $\Sigma-\Delta$ variables in the upper and lower arms can be presented as follows:

$$v_{Cj}^{\Delta} = \left(v_{Cj}^{U} - v_{Cj}^{L}\right)/2, \qquad v_{Cj}^{\Sigma} = \left(v_{Cj}^{U} + v_{Cj}^{L}\right)/2, \tag{2.2a}$$

$$m_j^{\Delta} = m_j^{U} - m_j^{L}, \qquad m_j^{\Sigma} = m_j^{U} + m_j^{L}, \tag{2.2b}$$

$$v_{Mj}^{\Delta} = \left(-v_{Mj}^{U} + v_{Mj}^{L}\right)/2 = -\left(m_j^{\Delta} v_{Cj}^{\Sigma} + m_j^{\Sigma} v_{Cj}^{\Delta}\right)/2, \tag{2.2c}$$

$$v_{Mj}^{\Sigma} = \left(v_{Mj}^{U} + v_{Mj}^{L}\right)/2 = \left(m_j^{\Sigma} v_{Cj}^{\Sigma} + m_j^{\Delta} v_{Cj}^{\Delta}\right)/2. \tag{2.2d}$$

Then, the AC gird current dynamics i_j^{Δ} and MMC circulating currents i_j^{Σ} for the three-phase case can be defined as:

$$i_j^{\Delta} = i_j^{U} - i_j^{L}, \qquad i_j^{\Sigma} = \left(i_j^{U} + i_j^{L}\right)/2. \tag{2.3}$$

By using Kirchhoff voltage law (KVL) in the MMC equivalent circuit depicted in Figure 2.3, one can immediately obtain the grid current and circulating current dynamics as:

$$L_{eq}^{ac} \frac{d}{dt}\left(\vec{i}_j^{\Delta}\right) = \vec{v}_{Mj}^{\Delta} - R_{eq}^{ac}\vec{i}_j^{\Delta} - \vec{v}_j^{G}, \tag{2.4a}$$

$$L_{arm} \frac{d}{dt}\left(\vec{i}_j^{\Sigma}\right) = \frac{v_{dc}}{2} - \vec{v}_{Mj}^{\Sigma} - R_{arm}\vec{i}_j^{\Sigma}, \tag{2.4b}$$

where, L_{eq}^{ac} and R_{eq}^{ac} are the equivalent inductance and resistance in the AC grid, which are calculated by $L_{eq}^{ac} = L_{arm}/2 + L_r$ and $R_{eq}^{ac} = R_{arm}/2 + R_r$, respectively. $\vec{v}_{Mj}^{\Delta}$ is the modulated voltage at the interfacing point between MMC and AC-grid side and $\vec{v}_j^{G}$ is the three-phase AC grid voltage.

It is worthwhile mentioning that the Δ variables are associated with the fundamental angular frequency ω, and the third harmonic 3ω components. In comparison, the Σ variables are associated with -2ω harmonics and contain a DC component.

After applying Park's transformation, the grid currents $\vec{i}_{dq}^{\Delta}$ and circulating currents

$\vec{i}^{\Sigma}_{dq}$ dynamics can be defined as:

$$\frac{d}{dt}\left(\vec{i}^{\Delta}_{dq}\right) = \frac{1}{L^{ac}_{eq}}\left(\vec{v}^{\Delta}_{Mdq} - \left(\omega L^{ac}_{eq} J_2 + R^{ac}_{eq} I_2\right)\vec{i}^{\Delta}_{dq} - \vec{v}^{G}_{dq}\right), \tag{2.5a}$$

$$\frac{d}{dt}\left(\vec{i}^{\Sigma}_{dq}\right) = -\frac{1}{L_{arm}}\left(\vec{v}^{\Sigma}_{Mdq} + (R_{arm} I_2 - 2\omega L_{arm} J_2)\,\vec{i}^{\Sigma}_{dq}\right), \tag{2.5b}$$

where $\vec{v}^{\Delta}_{Mdq}$ and $\vec{v}^{\Sigma}_{Mdq}$ are the modulated voltages in grid current and circulating current controller, respectively. I_2 is the identity matrix with size 2×2, and $J_2 = \begin{bmatrix} 0 & 1 \\ -1 & 0 \end{bmatrix}$.

The operating points of the converter can be obtained by solving the MMC differential equation. Here, P_{ac} and Q_{ac} as active and reactive powers of the AC grid, V_m and θ as the magnitude and phase of AC voltage, P_{dc} as the active power of DC side, V_{dc} as the DC voltage. The reference values for the operating point of the converter are determined as [73], [74]:

$$\begin{aligned} &P_{ac,ref} = P, \qquad Q_{ac,ref} = Q, \\ &i^{\Delta}_{d,ref} = \frac{2(v^{G}_{d} P + v^{Q}_{q} Q)}{3(v^{G^2}_{d} + v^{Q^2}_{q})}, \qquad i^{\Delta}_{q,ref} = \frac{2(v^{G}_{q} P - v^{Q}_{d} Q)}{3(v^{G^2}_{d} + v^{Q^2}_{q})}, \\ &v_{dc,ref} = V_{dc}, v^{G}_{d} = V_m \cos(\theta), \qquad v^{G}_{q} = -V_m \sin(\theta). \end{aligned} \tag{2.6}$$

The active and reactive powers for the MMC are:

$$P_{ac} = \frac{3}{2}(v^{G}_{d} i^{\Delta}_{d} + v^{G}_{q} i^{\Delta}_{q}), \qquad Q_{ac} = \frac{3}{2}(-v^{G}_{d} i^{\Delta}_{q} + v^{G}_{q} i^{\Delta}_{d}). \tag{2.7}$$

2.2.4. MMC CONTROL FORMULATION

This section presents the detailed MMC modeling process using a classical PI control.

The upper and lower controls of MMCs are based on the PI control published in Cigre B4.57 [75]. Inner current and outer controls depend on the operating mode of the MMC in the MTDC system. The onshore MMC adopts the grid-following mode, and the offshore MMC uses the grid-forming mode. The overall PI control schemes can be described as follows. Figure. 2.6. (a) and (b) describe the grid-following control for the onshore grid MMC station. Figure 2.6. (c) introduces the grid-forming control for offshore gird MMC station, Figure 2.6. (d) illustrates the CCSC controller, Figure 2.6. (e) explains the final modulation indices' generation control, in which the modulated indices are produced for each SMs.

OUTER CONTROL LOOPS

The outer control loop of the MMC plays a crucial role in determining the converter's operational mode and maintaining the necessary stability. The functionality of the outer control loop revolves around generating reference current signals to the inner loop. Two common operational modes dictated by the outer loop in MMCs are DC voltage/active power control and AC voltage/reactive power control modes.

In DC voltage/active power control mode, the outer control loop is designed to maintain the DC-link voltage at a constant reference level. It does so by controlling the active

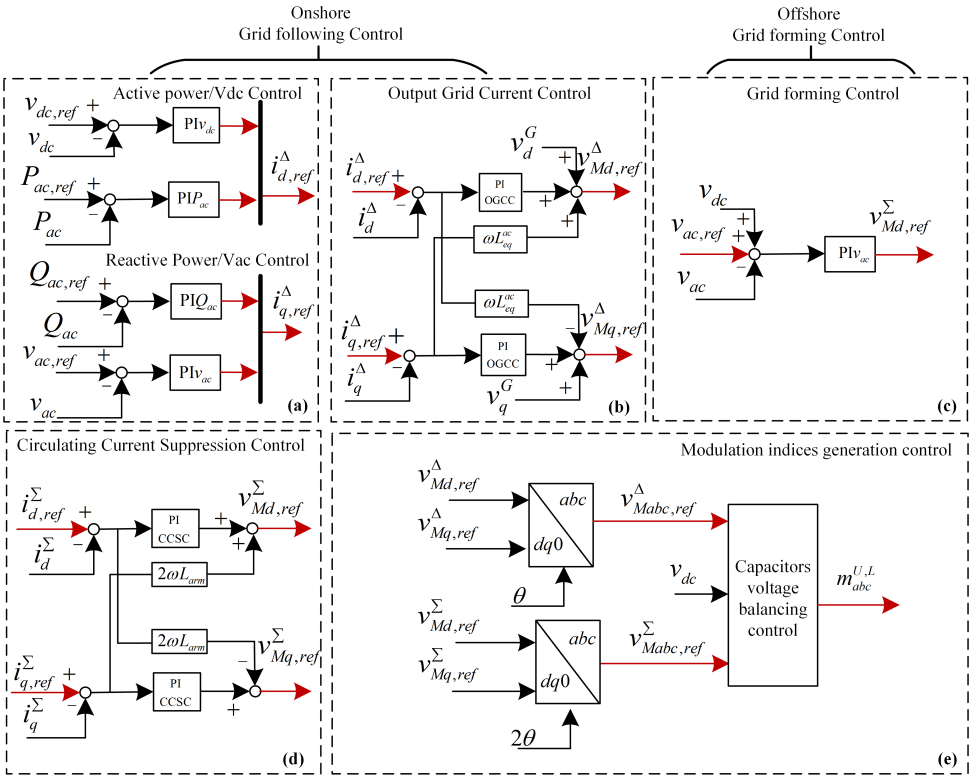

Figure 2.6: PI control scheme.(a) Outer control loop. (b) OGCC loop. (c) grid-forming control. (d) CCSC loop. (e) modulation indices generation control.

power flowing through the converter. If there is any variation between the desired $v_{dc,ref}$ and actual DC-link voltage v_{dc}, it modifies the active power reference accordingly to errors, thus ensuring the DC voltage remains constant. In AC voltage/reactive power control mode, the outer loop controls the grid side AC voltage v_{ac} by regulating the reactive power Q_{ac} exchanged with the grid. By adjusting the reactive power reference $Q_{ac,ref}$, the outer control loop can mitigate deviations in the AC voltage and maintain it at the desired level.

Specifically, in the case of grid-following MMC, the outer control loops use the DC voltage/active power control to provide the reference signal: $i^{\Delta}_{d,ref}$ for the d-axis grid current, depending on the variation of v_{dc} or P_{ac}, which can be seen as [67]:

$$\dot{\xi}_{v_{dc}} = v_{dc,ref} - v_{dc}, i^{\Delta}_{d,ref} = -K_{P,v_{dc}}\left(v_{dc,ref} - v_{dc}\right) - K_{I,v_{dc}}\xi_{v_{dc}}, \tag{2.8a}$$

$$\dot{\xi}_{P} = P_{ac,ref} - P_{ac} i^{\Delta}_{d,ref} = K_{P,P_{ac}}\left(P_{ac,ref} - P_{ac}\right) + K_{I,P_{ac}}\xi_{P} \tag{2.8b}$$

where the $K_{P,I,v_{dc}}$ and $K_{P,I,P_{ac}}$ are the control gains of the DC voltage and active power controllers, respectively.

For the reference value $i^{\Delta}_{q,ref}$ of the q-axis grid current, the variation of Q_{ac} or v_{ac} of

AC gird can be utilized as [53], [74]:

$$\dot{\xi}_Q = Q_{ac,ref} - Q_{ac}, i^{\Delta}_{q,\text{ref}} = -K_{P,Q_{ac}}\left(Q_{ac,ref} - Q_{ac}\right) + K_{I,Q_{ac}}\xi_Q \tag{2.9a}$$

$$\dot{\xi}_{v_{ac}} = v_{ac,ref} - v_{ac}, i^{\Delta}_{q,ref} = -K_{P,v_{ac}}\left(v_{ac,ref} - v_{ac}\right) - K_{I,v_{ac}}\xi_{v_{ac}} \tag{2.9b}$$

where the $K_{P,I,Q_{ac}}$ and $K_{P,I,v_{ac}}$ are the control gains of the reactive power and AC voltage controller.

In both operational modes, the outer control loops continuously monitor the converter's performance, compare it with the reference values, and adjust the converter's operational parameters as needed. The reference current signals are then passed to the inner control loops.

OUTPUT GRID CURRENT CONTROL (OGCC) LOOPS

The OGCC ensures the current waveforms maintain high quality, conform to grid codes and regulations, and respond swiftly to changes in operating conditions or reference signals from the outer loops.

The OGCC loops work primarily by comparing the actual grid current waveform with the reference current waveforms $\vec{i}^{\Delta}_{dq,ref}$ provided by the outer loop, defined based on the MMC's working mode. The variations between the actual and reference currents are then used to generate an error signal. Finally, the OGCC transfers the error information into modulation voltage signals to determine the necessary switching PWM signals for the MMC SMs, controlling the generation and conduction of the converter's output current. In this way, the OGCC loop ensures that the grid current closely follows the reference waveform.

The control of OGCC adopts the equations of [53], [74]:

$$\dot{\vec{\xi}}^{\Delta}_{dq} = \vec{i}^{\Delta}_{dq,ref} - \vec{i}^{\Delta}_{dq}, \tag{2.10a}$$

$$\vec{v}^{\Delta}_{Mdq,ref} = K^{\Delta}_{I,dq}\vec{\xi}^{\Delta}_{dq} + K^{\Delta}_{P,dq}\left(\vec{i}^{\Delta}_{dq,ref} - \vec{i}^{\Delta}_{dq}\right) + \omega L^{ac}_{eq} J_2 \vec{i}^{\Delta}_{dq} + \vec{v}^{G}_{dq}, \tag{2.10b}$$

where the $K^{\Delta}_{P,I,dq}$ are the control gains for the OGCC controllers.

For the offshore grid, the MMC is controlled by the grid forming control to support wind turbine based on the direct Voltage (V_{ac}/f) control [76], which can be described in the following equations:

$$\dot{\xi}_{v_{ac}} = v_{ac,ref} - v_{ac}, \tag{2.11a}$$

$$v^{\Delta}_{Md,ref} = K_{I,gf}\xi_{v_{ac}} + K_{P,gf}\dot{\xi}_{v_{ac}} + v_{dc}, v^{\Delta}_{Mq,ref} = 0, \tag{2.11b}$$

where the $K_{P,gf}$ and $K_{I,gf}$ are the control gains for the grid forming controller.Further, equation (2.11) is applied to the inverse dq-transformation to obtain a three-phase modulating waveform. Due to the absence of the offshore grid reference, we need a self-synchronization mechanism. Hence, an oscillator is used, which provides an angle θ for the inverse dq-transformation.

CIRCULATING CURRENT SUPPRESSION CONTROL (CCSC) LOOPS

Circulating current suppression control aims to regulate and suppress circulating currents within the MMC converter.

These circulating currents arise due to the mismatch between the different voltage levels of the SMs or between the input and output voltages of the converter. While circulating currents do not contribute to the power transfer between the DC and AC sides, they can lead to increased power losses and thermal stress, potentially reducing the converter's efficiency and lifespan. These currents also cause voltage ripples in the SM and distort the current through the arm. As a result, it influences the rating of SM capacitance and IGBT switches.

The CCSC is constructed to set the circulating currents to their reference values, which are assumed to be $\vec{i}^{\Sigma}_{dq,ref} = [0,0]^T$. The specific equations of CCSC adopted are presented as follows [53], [74],

$$\dot{\vec{\xi}}^{\Sigma}_{dq} = \vec{i}^{\Sigma}_{dq,ref} - \vec{i}^{\Sigma}_{dq}, \tag{2.12a}$$

$$\vec{v}^{\Sigma}_{Mdq,ref} = -K^{\Sigma}_{I}\vec{\xi}^{\Sigma}_{dq} - K^{\Sigma}_{P}\left(\vec{i}^{\Sigma}_{dq,ref} - \vec{i}^{\Sigma}_{dq}\right) + 2\omega L_{arm} J_2 \vec{i}^{\Sigma}_{dq}, \tag{2.12b}$$

where K^{Σ}_{p} and K^{Σ}_{I} are the control gains of CCSC loop.

The generated voltage reference is then used to control the converter's SMs switching, adjusting the voltage levels to mitigate the circulating current.

According to Eq.(2.12) and Figure 2.6, it is noted that the circulating currents flow in a negative sequence with a frequency of 2ω, the ω comes from the PLL in the outer control loops.

2.3. INTRODUCTION TO DCCBS

DCCBs are supposed to be widely utilized in the HB-MMC-based MTDC system and interact with DC protections to clear the DC faults and isolate the faulty lines.

Unlike AC systems, DC systems do not have a zero-crossing point. Consequently, DCCBs must generate a zero-crossing point to interrupt the fault current. The fast transient oscillations and high short-circuit currents make interrupting DC faults more challenging. To prevent MMC blocking and further propagation of DC faults, both the response time and fault-clearance time of a DCCB must be achieved within an extremely short period. These technical challenges make the design of DCCBs more difficult compared to ACCBs [77], [78].

Ongoing research on HVDC DCCBs can be classified into two main types [79]: mechanical DCCBs and hybrid DCCBs [80]. During normal conditions, the mechanical switch carries the line current. During a fault, the line current is temporarily transferred to a parallel branch. In the hybrid breaker, this branch extinguishes the fault current using the turn-off capability of a string of series-connected semiconductor devices (e.g., IGBTs) [78]. Mechanical circuit breakers utilize a parallel "current injection branch" to inject an additional current component causing the current zero-crossing of the fault current in the mechanical switch [81].

The mechanical DCCB has the advantage of low conduction losses. However, the performance is limited by the switching speed and long operational delay, which cannot meet the requirements of fast current interruption in MMC-based MTDC grids [82].

The hybrid DCCB is capable of fast current interruption and low on-state losses as it comprises both semiconductors and mechanical interrupter components. However, the series-connected semiconductor devices need to withstand the very high TIV, resulting in relatively high component costs for hybrid DCCBs. As such, high costs make them less favored in practice.

Due to the fast current interruption performance, the newly emerging DCCB concept, the voltage-source converter resonant current (VARC) DCCB proposed in [78], [83], is primarily implemented for the study of this thesis. The configuration of the VARC DCCB can be seen in Figure. 2.7.

Before the DCCB operates, the VSC energy storage capacitor C_{DC} is pre-charged. After the fault occurrence, the protection detects the fault and trips the VARC DCCB. The ultra-fast actuator starts to drive the separation of contacts, reaching a sufficient gap to withstand the TIV. The VSC is activated to generate high-frequency oscillating currents, of which the amplitude increases until zero-crossing is created in the arc current. The VI stops conducting, and the fault current is commutated to the current injection branch until the voltage of the branch capacitor reaches the clamping voltage of SA. Next, the SA starts to conduct, and the line current is commutated into the energy absorption branch. The SA current then decreases until it drops to zero. After the fault current is interrupted, the residual circuit breaker facilitates the clearing of the leakage current and separates the breaker main circuit from the DC grid.

The detailed description of the VARC DCCB operation can be found in [83]. The parameters of the VARC DCCBs in [83] are scaled into the studied system within the thesis following the approach introduced in [84]. The fault currents will be interrupted within 3 ms.

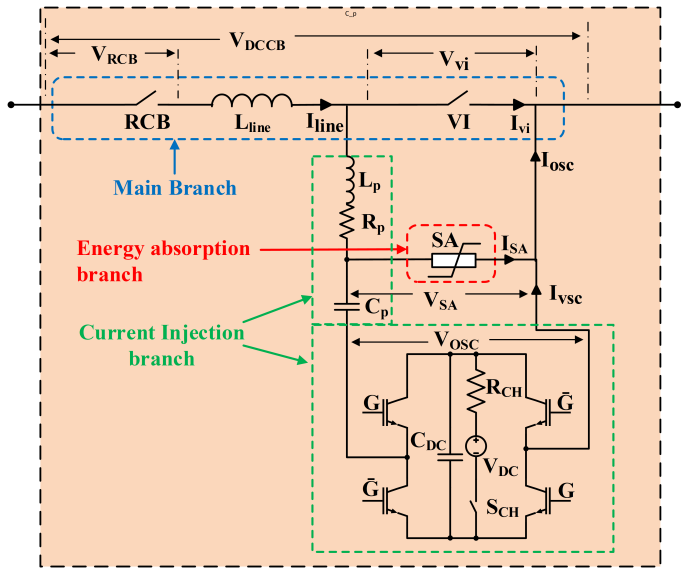

Figure 2.7: Configuration of VARC DCCB. [83]

2.4. FAULT RESPONSES OF THE MTDC SYSTEM

In an HVDC system, whether it involves a cable transmission line or an overhead transmission line, the occurrence of DC faults is inevitable and unpredictable [66]. That is to say, at any moment and at any location, various types of DC faults may occur due to the destruction of the line, lightning strikes, or the insulation layer. The short circuit fault is one of the critical contingencies for the MMC-based MTDC system.

2.4.1. TESTING SYSTEM

In this section, the four-terminal **DCS2** testing system, proposed by the Cigre B4.57 group, is used as a case study. The system's configuration can be seen in Figure 2.8. This section aims to demonstrate the response of the MMC-based MTDC system during the post-fault stage, emphasizing the need for protection, control, and DCCB performance. Hence, the actions of the protection and DCCBs are not considered in the **DCS2** system. The controllers are implemented using the classical PI controller, as previously explained.

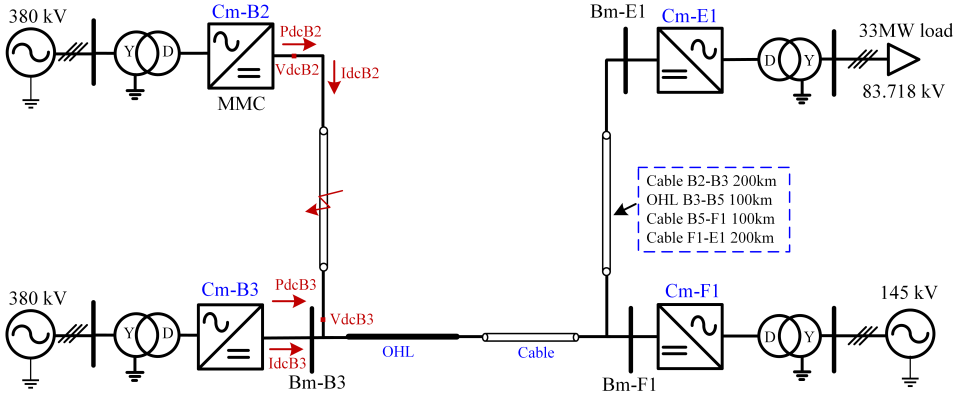

Figure 2.8: Configuration of Cigre DCS2 testing system.

The most serious DC fault, Pole-to-Pole Short Circuit (PTP), occurs in Cable B2-B3. The fault takes place 10 km from MMC Cm-B2. It is a metallic and permanent fault occurring at 1.0s. The sampling frequency is set to 50 kHz. The converters will be blocked when the valve currents exceed 6 kA. The ACCB in the AC grid will operate if the absolute value of AC grid voltage is lower than 0.1 p.u with a time delay of 20 ms. It is noted in the **DCS2** testing system the CLR is not implemented.

2.4.2. RESPONSE ON DC SIDES

The transient responses of DC currents, voltages, and power flows are seen in Figure 2.9. In the steady state, the DC currents, voltages, and power flows remain constant. After the fault, the DC currents IdcB2 and IdcB3, as seen in Figure. 2.9 (a), increase immediately when the fault-induced TWs arrive at the cable terminals. IdcB2 reaches the peak value of 7.31 kA at 0.36 ms, while IdcB3 reaches the peak value of 6.21 kA at 1.62 ms, respec-

tively. The fault currents mainly originate from the MMC arm capacitors' discharging currents at this stage. When the MMCs are blocked due to the valve overcurrent protection, the cable currents will increase again, fed by the AC grids through the free-wheeling diodes. The series DC inductors contribute to decreasing the rise speed and peak value of fault current, extending the time of fault clearing. However, the time frame remains within several milliseconds. To this end, it is very clear from Figure 2.9 that when the DC protection and DCCBs do not operate to interrupt the fault currents, the fault currents continue to increase to an extremely high value, which may easily damage the power electronic devices, e.g., converter valves and increase the difficulties to cut it off.

For the DC voltages demonstrated in Figure 2.9 (b), as the fault is closer to the MMC Cm-B2 (10km), the DC waveform of voltage VdcB2 experiences more violent oscillations, caused by the voltage TWs injections and reflections between the converter Cm-B2 and the fault point. Similar results are also found in VdcB3 with different numbers of reflections. Finally, the voltages of VdcB2 and VdcB3 drop to zero as the fault type is PTP. The active power PdcB2 supplied by the MMC Cm-B2 decreases to zero when the voltage VdcB2 drops to zero. The MMC Cm-B3 absorbs the power of 830 MW from MMC Cm-B2 and MMC Cm-F1 in a steady state. After the fault is removed, the MMC Cm-B2 injects power into the fault circuit. The power flow distribution is disordered, as shown in Figure 2.9. (c).

2.4.3. RESPONSES OF MMC AND AC GRIDS

The transient responses of MMC converters Cm-B2 and Cm-B3 and AC grid phase currents can be seen in Figure. 2.10 and Figure. 2.11. The MMC-based MTDC system is a low-inertia [85] system due to the high participation of renewable energy and power electronic devices. Before the failure begins, the MMC arm currents remain balanced and stable. After the fault, the DC capacitors of the converters will discharge rapidly, and these discharging currents flow toward the fault point through the IGBTs. The two converter stations each reach 6 kA within 2 ms. The converter Cm-B2 and Cm-B3 are blocked, preventing them from being damaged by the huge transient energy, and the SMs switch to the blocked mode shown in Figure 2.4. As shown in Figure 2.11 and Figure 2.12, the balanced operation of AC grids also collapsed due to the uncontrollable bridge of MMC. The AC grids begin to continuously inject current towards the fault point through the reverse-parallel diodes of the IGBTs in the SMs, causing the fault current to increase further, as shown previously in Figure 2.9 (a). The AC grid voltages also experience oscillations after the fault occurs. The low-voltage protection starts operating at 1.048s and 1.047s of MMC Cm-B2 and Cm-B3, respectively. The DCCB then isolates the AC grids from the MMC and DC grids with a 20 ms, as shown in Figure 2.11 and Figure 2.12.

If the AC protection and ACCBs do not operate to isolate the AC grid from the MMCs and DC grids, the fault currents will continue to increase, resulting in cascaded AC/DC faults until the entire MTDC system collapses. If the AC grid protection and ACCBs operate to isolate from connecting the faulty sections (without the operations of DC protections and DCCBs), the AC grids will stop feeding the fault currents, as shown in Figure 2.11. However, the DC voltages, currents, and active powers on the DC sides will be zero in grids within 50-70 ms after the fault occurs, depending on the exact AC protection

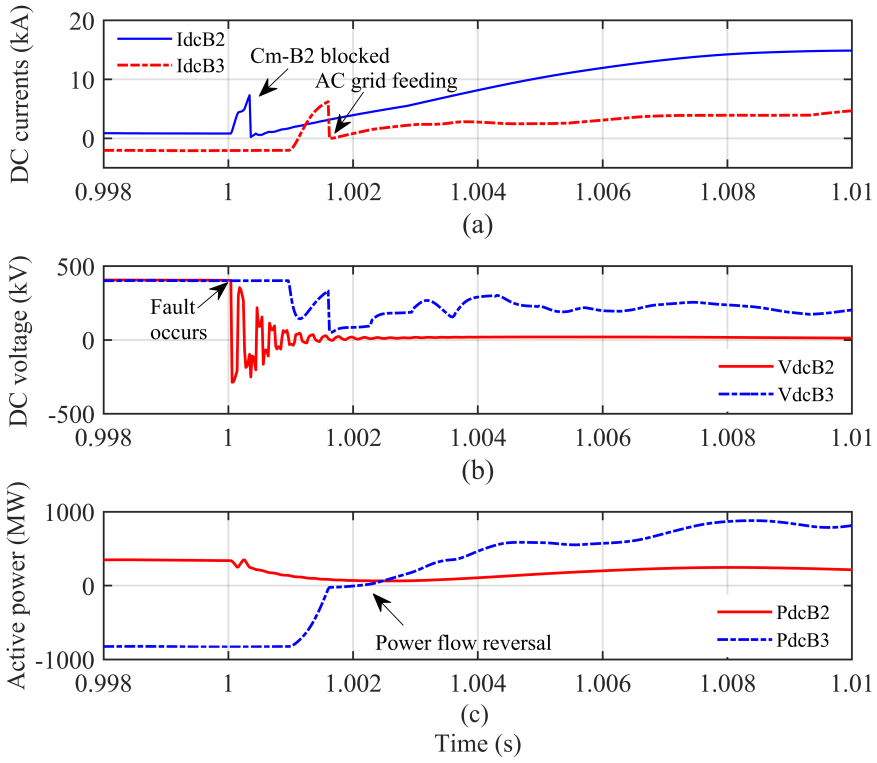

Figure 2.9: Response of DC side. (a). DC currents; (b). DC voltages; (c). Power plow.

thresholds and design. The entire MTDC system is shut down, which is also unacceptable in practice. As such, the best option is still to apply DC protection and DCCBs to isolate the fault at the beginning of the post-fault stage. For DC faults, the AC-side protection and circuit breakers can only serve as the last line of defense to isolate DC faults for system safety.

To conclude, the steady-state operation of the faulty cable B2-B3 experiences serious damage due to the PTP fault. The MMCs are blocked due to the huge value of valve currents, and the steady state of the main AC grids is also affected, injecting the fault currents into the faulty DC cable. The entire MTDC system faces the risks of collapse, cascading faults, and in the most serious scenarios, a blackout may occur. This outcome is not expected in a practical MTDC project, where ensuring power supply reliability is the priority. As such, robust DC protections and fast DCCBs must be implemented to interrupt fault currents and isolate the faulty cable immediately, preventing the wider spread of the DC fault.

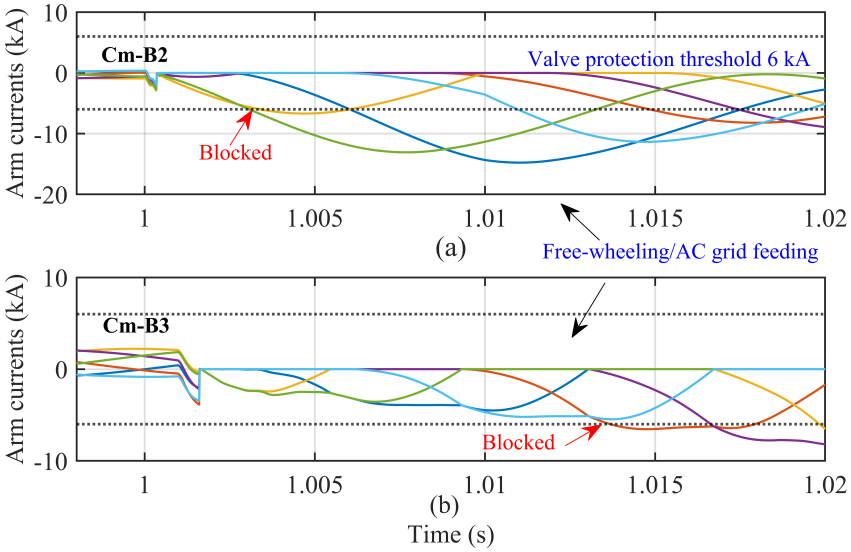

Figure 2.10: MMC arm currents. (a).MMC Cm-B2; (b). MMC Cm-B3.

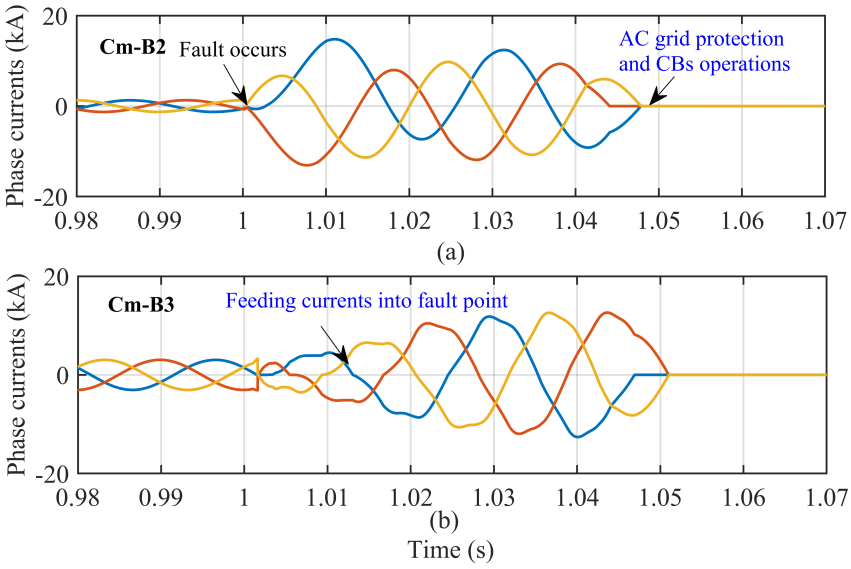

Figure 2.11: MMC phase currents. (a).MMC Cm-B2; (b). MMC Cm-B3.

2.5. ROLES OF PROTECTION, CONTROL AND FAULT LOCATIONS

Figure 2.13 illustrates the detailed roles of DCCBs, DC protections, MMC controllers, and fault locators during the transient phases from the initial steady-state to re-stabilization

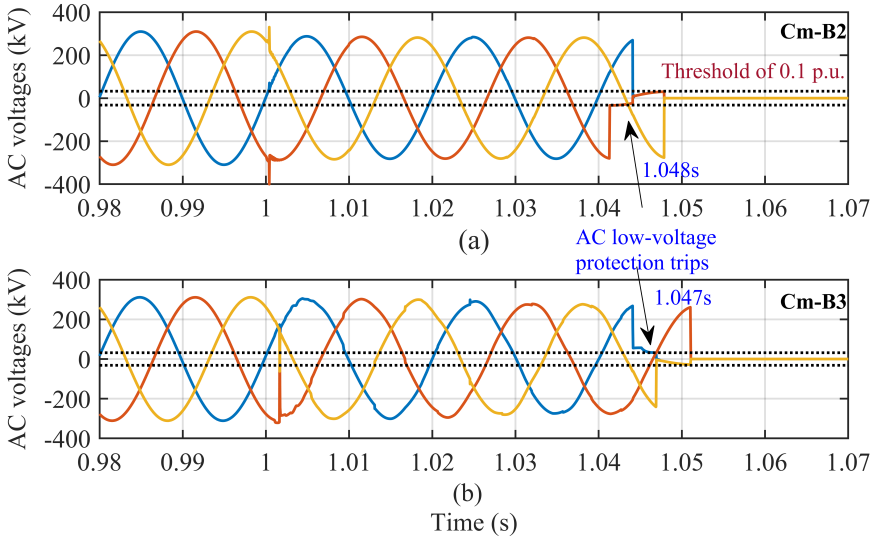

Figure 2.12: AC grid voltages. (a).MMC Cm-B2; (b). MMC Cm-B3.

after a DC fault.

- Phase I: Starting from t_0, the MTDC system operates at a steady state. All the voltages, currents, power flows, and AC grid frequencies are at rated values.
- Phase II: Assuming a DC fault occurs on a DC transmission line at t_1, the fault-induced TWs propagate along the transmission lines. The DC protection, installed at line terminals, detects the faulty lines and fault types using the implemented protection algorithms within 2-3 ms [66]. The DC inductor helps to limit the fault currents, and tripping signals from protection relays are sent to the corresponding DCCBs. This phase primarily focuses on fault detection.
- Phase III: When the DCCBs receive the tripping signal at t_2, they will interrupt the fault currents, absorb the electromagnetic energy, and isolate the fault lines. This process generally takes 3-6 ms [25]. During this phase, the voltages/currents and power flow experience significant oscillations. Advanced MMC controllers maintain the system operation at rated values and reduce these oscillations. Additionally, fault location algorithms operate to estimate the actual fault location within the faulty line and to determine whether the fault is temporary or permanent.
- Phase IV&V: At instant t_3, if the fault is temporary, the DCCBs will reclose to reconnect the faulty cable at t_4, thus avoiding power supply discontinuity. However, if the fault is permanent, the protection system will trip the DCCBs again, and the faulty line will remain disconnected until the cable is repaired.
- Phase VI: Assuming the faulty line is reconnected at t_5, the system begins a new transient stage, returning to its initial steady state. The voltage, current, and power

flow on the faulty line will be re-energized to their rated values. Advanced MMC controllers dominate this phase, contributing to increased system stability, accelerated restoration, and reduced system oscillations [53].

- Phase VII: The system is restored from the fault condition and operates again in the steady state.

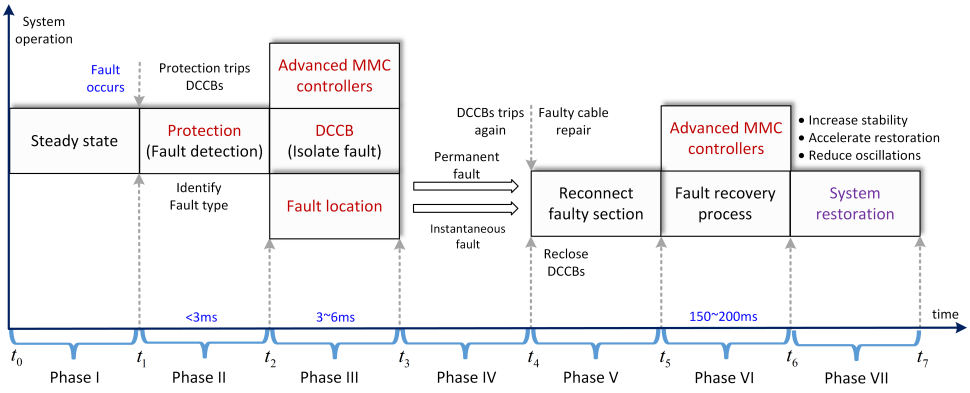

Figure 2.13: Entire transient phases in the post-fault stage.

2.6. CONCLUSION

This chapter first provides a detailed introduction to the technical superiority of the multi-terminal connection of the MMC-HVDC system, dividing MTDC into two parts of the power grid: onshore and offshore. It describes the functionalities, operating principles, and other aspects of the key components within these grids. Thus far, the research background and research model of this paper have been formulated.

Subsequently, the chapter organizes the basic structure, operating principles, working modes, and control strategies of MMCs, and elaborately introduces the principles of traditional PI control for each circuit of MMC. Additionally, DCCBs are also one of the key components studied in this thesis. The chapter provides a detailed description of the working principles of DCCBs and introduces the operating principles and basic structure of the VARC DCCBs used.

The chapter adopts a classical PTP DC fault simulated in the Cigre DCS2 testing system as an example. It analyzes the transient responses of the DC cables, MMCs converter stations, and AC grids in the post-fault stage. Without the application of the DC protection and DCCBs, the DC currents will continue to rise, the DC voltage will collapse to zero, and the power flow supplied from the MMCs will reverse. The system stable operation is severely impacted, with the risk of cascading faults and system collapse. This highlights the importance of the control and protection study in subsequent chapters.

Finally, this chapter addresses the specific roles of advanced control strategies, protection, and fault location in the post-fault stage, laying the groundwork for subsequent chapters.

3

THE NON-LINEAR CONTROL METHODS FOR MMCS

This chapter introduces the modeling and stability analysis of non-linear MMC control methods. Three non-linear control methods, back-stepping control (BSC), sliding mode control (SMC), and advanced model predictive control (MPC), are selected to model the MMC. The detailed modeling process is introduced.

Parts of this chapter have been published in [53], [86].

Classical PI controllers introduced in Chapter II have been widely used for many control applications due to their simplicity and ease of implementation. However, for MMC systems, especially in the context of system transients, several drawbacks are associated with using classical PI controllers. For example, the PI controllers may not respond quickly enough to transient disturbances. During large disturbances like AC or DC faults, the delayed response of PI controllers can lead to undesirable system behaviors during rapid changes.

In this case, this chapter provides a detailed introduction to the modeling process and stability analysis of three advanced non-linear control methods for MMC, including the BSC, SMC, and MPC, to provide optimal MMC control solutions.

3.1. MODELING OF BACK-STEPPING CONTROL

This section emphasizes the modeling of the MMC converter utilizing the BSC approach. The *Lyapunov* stability analysis is also provided to ensure the system stability.

3.2. STATE-SPACE BSC FORMULATION

Recall that the MMC grid- and circulating currents dynamics are:

$$\frac{d}{dt}\left(\vec{i}_{dq}^{\Delta}\right) = \frac{1}{L_{eq}^{ac}}\left(\vec{v}_{Mdq}^{\Delta} - \left(\omega L_{eq}^{ac} J_2 + R_{eq}^{ac} I_2\right)\vec{i}_{dq}^{\Delta} - \vec{v}_{dq}^{G}\right), \tag{3.1a}$$

$$\frac{d}{dt}\left(\vec{i}_{dq}^{\Sigma}\right) = -\frac{1}{L_{arm}}\left(\vec{v}_{Mdq}^{\Sigma} + \left(R_{arm} I_2 - 2\omega L_{arm} J_2\right)\vec{i}_{dq}^{\Sigma}\right), \tag{3.1b}$$

Since the BSC approach exhibits more desired performance for modeling the systems with higher layers, the CCSC and outer q-axis grid current control loop adopts classical PI controllers as described in detail previously. Only the grid currents loop is formulated using the BSC approach.

In this work, the proposed BSC loop contains three state variables, which are the d-q frame grid currents i_d^{Δ}, i_q^{Δ} and the energy W_z stored in the capacitor of each MMC's sub-module. As such, the state variables $\vec{x}$ and control variables $\vec{u}$ can be defined as follows:

$$\vec{x} = \begin{bmatrix} x_1 & x_2 & x_3 \end{bmatrix}^T = \begin{bmatrix} W_z & i_d^{\Delta} & i_q^{\Delta} \end{bmatrix}^T, \tag{3.2a}$$

$$\vec{u} = \begin{bmatrix} u_1 & u_2 \end{bmatrix}^T = \begin{bmatrix} v_{Md}^{\Delta} & v_{Mq}^{\Delta} \end{bmatrix}^T, \tag{3.2b}$$

where W_z provides a virtual reference for the state variable i_d^{Δ} and can be calculated as: $W_z = 3C(V_{dc})^2/N$, and C is the capacitance of each sub-module.

The AC and DC power flows across the MMC are used to link the state variable W_z. The AC power P_{ac} can be expressed as:

$$P_{ac} = \frac{3}{2}(v_d^G i_d^{\Delta} + v_q^G i_q^{\Delta}) \tag{3.3}$$

Considering that the v_q^G after the PLL loop is zero, the MMC's dynamics can be pre-

sented as follows:

$$\dot{x}_1 = P_{ac} - P_{dc} = \frac{3}{2} v_d^G i_d^\Delta - P_{dc} \tag{3.4a}$$

$$\dot{x}_2 = \frac{1}{L_{eq}^{ac}} \left(v_{Md}^\Delta - R_{eq}^{ac} i_d^\Delta - \omega L_{eq}^{ac} i_q^\Delta - v_d^G \right) \tag{3.4b}$$

$$\dot{x}_3 = \frac{1}{L_{eq}^{ac}} \left(v_{Mq}^\Delta - R_{eq}^{ac} i_q^\Delta + \omega L_{eq}^{ac} i_d^\Delta - v_q^G \right) \tag{3.4c}$$

We define the error variables e and their time derivatives $\dot{\boldsymbol{e}}$ as follow:

$$\boldsymbol{e} = \begin{bmatrix} e_1 & e_2 & e_3 \end{bmatrix}^T = \begin{bmatrix} W_{\text{zef}} - W_z & e_v - i_d^\Delta & i_{q,ref}^\Delta - i_q^\Delta \end{bmatrix}^T \tag{3.5a}$$

$$\dot{\boldsymbol{e}} = \begin{bmatrix} \dot{e}_1 & \dot{e}_2 & \dot{e}_3 \end{bmatrix}^T = \begin{bmatrix} \dot{W}_{\text{zef}} - \dot{W}_z & \dot{e}_v - \dot{i}_d^\Delta & \dot{i}_{q,ref}^\Delta - \dot{i}_q^\Delta \end{bmatrix}^T \tag{3.5b}$$

where e_v is the virtual control variable from the energy controller, which corresponds to the reference value of the state variable x_2 (i_d^Δ).

3.2.1. STABILITY ANALYSIS

INTRODUCTION OF THE LYAPUNOV SECOND METHOD

Lyapunov's second method [87]–[89], commonly referred to as the "*Lyapunov* direct method," is an important tool in studying the stability of dynamical systems. It's especially useful because it can determine stability without solving the system's dynamic equations. The *Lyapunov* stability theory is introduced as follows [87]–[89].

Considering a system of differential equations described as:

$$\dot{x}(t) = f(x(t)) \tag{3.6}$$

where $x \in \mathbb{R}^n$ is the state variable and $f : \mathbb{R}^n \to \mathbb{R}^n$ is the system function. The point that $x = 0$ is an equilibrium point of the system if $f(0) = 0$.

Definition 1.1. ***Lyapunov* function:** The key of the second method is the *Lyapunov* function, a scalar function $V : \mathbb{R}^n \to \mathbb{R}^n$ that is:

- Positive definite (PD): $V(0) = 0$ and $V(x) > 0$ for all $x \neq 0$.
- Radially unbounded: $V(x) \to \infty$ as $\|x\| \to \infty$.

Definition 1.2. Stability definitions: For the equilibrium point $x = 0$, two stability conditions are defined:

- Asymptotic Stability: The equilibrium is said to be asymptotically stable if it is stable, and all trajectories that start sufficiently close to the equilibrium tend to it as $t \to \infty$.
- Global Asymptotic Stability: The equilibrium is said to be globally asymptotically stable if it is stable, and all trajectories tend to the equilibrium as $t \to \infty$, regardless of the initial condition.

Definition 1.3. ***Lyapunov's* Direct Method Theorems** are:

- Stability: If there exists a Lyapunov function V such that its derivative along the system trajectories $\dot{V}(x)$ is non-positive ($\dot{V}(x) \leq 0$) for all $x \neq 0$, then the equilibrium $x = 0$ is stable.

• Asymptotic stability: If in addition to the above condition on $\dot{V}(x) \leq 0$, there exists a region where $\dot{V}(x) < 0$ for all $x \neq 0$ (strictly negative definite (ND)), then the equilibrium $x = 0$ is asymptotically stable within that region.

• Global Asymptotic Stability: if V is radially unbounded and $\dot{V}(x) < 0$ for all $x \neq 0$, then $x = 0$ is globally asymptotically stable.

LYAPUNOV STABILITY ANALYSIS

To prove the stability of (3.5) using the introduced theory, the key step is to select the proper candidate of the *Lyapunov* function, which plays a critical role in the analysis of the stability of dynamical systems.

Finding a proper *Lyapunov* candidate for a system's stability analysis can be challenging. There are several common *Lyapunov* candidates, such as the quadratic functions [90], the sum of squares [91], and the norm functions [92]. This thesis adopts the sum of squares candidate [53], [86] among these candidates since it is a powerful, simple, and flexible choice in most applications for analyzing the stability of nonlinear systems.

As such, the following *Lyapunov* function [53] is constructed:

$$\mathrm{V}(x) = \frac{1}{2}e_1^2 + \frac{1}{2}e_2^2 + \frac{1}{2}e_3^2. \tag{3.7}$$

It is straightforward to conclude that $\mathrm{V}(x)$ is positive for all $e_1, e_2, e_3 \neq 0$, and is met only when the system is operating in steady-state condition ($e_1, e_2, e_3 = 0$).

According to *Lyapunov*'s direct method, the transient stability analysis is used to determine whether the *Lyapunov* function is decreasing along the system's trajectories. Given that the constructed *Lyapunov* function $\mathrm{V}(x)$ is differentiable everywhere, the stability of MMC operation can be ensured if the time derivative of $\mathrm{V}(x)$ is negative everywhere except in the equilibrium point, which is calculated as:

$$\dot{\mathrm{V}}(x) = e_1\dot{e}_1 + e_2\dot{e}_2 + e_3\dot{e}_3. \tag{3.8}$$

Let us first consider the item $e_1\dot{e}_1$. The $\dot{e}_1$ can be expressed as $\dot{e}_1 = \dot{W}_{zref} - 3v_d^G i_d^\Delta/2 + P_{dc}$ according to (3.4). It is worthwhile to highlight that the energy reference W_{zef} is set as a constant value, which gives that the derivative $\dot{W}_{zef} = 0$. To ensure the item $e_1\dot{e}_1$ is strictly negative, we can define the item $\dot{e}_1$ as $-k_1e_1$. Thus, the desired value of i_d^Δ, which refers to the variable e_v, should be:

$$e_v = 2\left(k_1e_1 + P_{dc}\right)/3v_d^G \tag{3.9}$$

Therefore, $e_1\dot{e}_1$ is always negative and can be expressed as $-k_1e_1^2$ for $k_1 > 0$, where one can obtain:

$$\dot{\mathrm{V}}(x) = e_1(-3v_d^G(e_v - e_2)/2 + P_{dc}) + \dot{e}_2 + e_3\dot{e}_3 \tag{3.10}$$

If the following conditions are satisfied and we guarantee that $k_2, k_3 > 0$, then the *Lyapunov* function is ND ($\dot{V}(x) < 0$) [53], [86]:

$$\dot{e}_2 - e_1v_d^G/2 = -k_2e_2, \tag{3.11a}$$

$$i_{qref}^\Delta - \left(v_{Mq}^\Delta - R_{eq}^{ac}i_q^\Delta + \omega L_{eq}^{ac}i_d^\Delta - v_q^G\right)/L_{eq}^{ac} = -k_3e_3. \tag{3.11b}$$

To further eliminate the steady-state errors, additional adaptive terms θ_d and θ_q are considered [62]:

$$\theta_d = -\int k_{di} e_2 dt, \quad \theta_q = -\int k_{qi} e_3 dt, \tag{3.12}$$

where the k_{di} and k_{qi} are the control gains of the adaptive terms. It is noted that all adaptive terms would be zero in the steady state. With the adaptive terms, the adaptive BSC approach ensures the system has fewer overshoots and undershoots during transients. We have the final expressions of control variables v_{Md}^{Δ} and v_{Mq}^{Δ} as [86]:

$$\begin{aligned} v_{Md}^{\Delta} &= L_{eq}^{ac}(\dot{e}_v + k_2 e_2) - R_{eq}^{ac} i_d^{\Delta} - L_{eq}^{ac} i_q^{\Delta} \omega - v_d^G - \int k_{di} e_2 dt, \\ v_{Mq}^{\Delta} &= \left(\dot{i}_{qref}^{\Delta} + k_3 e_3\right) L_{eq}^{ac} + R_{eq}^{ac} i_q^{\Delta} - L_{eq}^{ac} i_d^{\Delta} \omega + v_q^G - \int k_{qi} e_3 dt. \end{aligned} \tag{3.13}$$

Up to this point, we have proved that $\dot{V}(x)$ is strictly negative everywhere, which can be expressed as $\dot{V}(x) = -k_1 e_1^2 - k_2 e_2^2 - k_3 e_3^2$. As such, the designed BSC for MMC is stable.

The control gains of BSC in this thesis are set as $k_1 = 0.48$, $k_2 = 0.5$, $k_3 = 0.48$, $k_{di} = 20.0$, and $k_{qi} = 20.0$, respectively.

To this end, the overall BSC scheme can be described as shown in Figure 3.1:

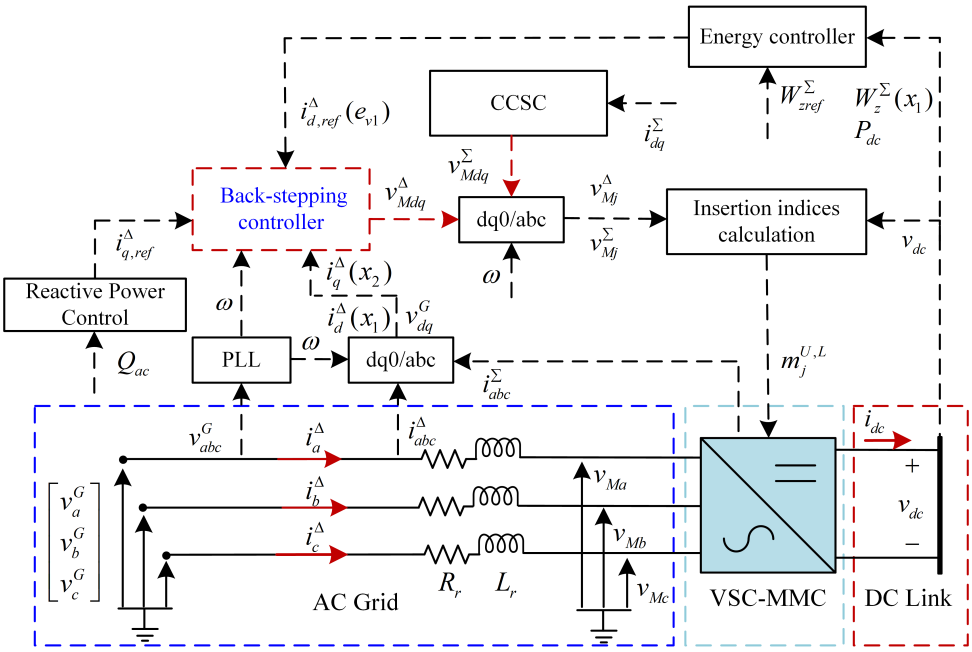

Figure 3.1: Flowchart of BSC controller.

3.3. SLIDING MODE CONTROL FORMULATION

The SMC formulations for MMC are introduced in this section. The second-order super-twisting slide mode is implemented in this thesis, which produces a continuous control

action and preserves the accuracy and robustness features of classic SMC. Moreover, this method does not require a time derivative of the sliding surface function $\dot{S}$, which is another important feature of this method.

The proposed SMC control law follows the super-twisting controller introduced in [63], [64], [93]:

$$\dot{S}\left(i_{d,q}^{\Delta}\right) = -\alpha'\sqrt{x_{d,q}}\,\mathrm{sgn}(x_{d,q}) - \beta'\int \mathrm{sgn}(x_{d,q}),\ \alpha' > \beta' > 0, \tag{3.14}$$

where $\alpha' = 1.5\sqrt{H}$ and $\beta' = 1.1H$. H is the upper bound of the system disturbance. The value of H is fixed at 10. The $x_{d,q}$ are the corresponding outputs of the grid current controller, defined as:

$$\dot{\vec{\zeta}}_{dq}^{\Delta} = \vec{i}_{dq,ref}^{\Delta} - \vec{i}_{dq}^{\Delta}, \vec{x}_{dq}^{\Delta} = K_i^{\Delta}\vec{\boldsymbol{\zeta}}_{dq} + K_p^{\Delta}\dot{\vec{\boldsymbol{\zeta}}}_{dq}^{\Delta}. \tag{3.15}$$

It is obvious that both terms of the control input are continuous, and the chattering is attenuated.

To minimize the steady-state error and process a faster transient response, the following sliding surface of degree one is considered:

$$\begin{aligned} S(e_{vo},t) &= \dot{e}_{vo} + \lambda e_{vo}, \\ \dot{S}(e_{vo},t) &= \varphi_1 + \gamma v_{inv} + h(t). \end{aligned} \tag{3.16}$$

The final control law that must fulfill the attractivity in the presence of uncertainties and disturbances: $S(S\dot{S} \leftarrow \eta|S|, S \neq 0, \eta > 0)$, which can be calculated as [93]:

$$\dot{S}(e_{vo},t) = h(t) = \varphi_1 + \gamma v_{eq} \rightarrow v_{eq} = \frac{-\varphi_1}{\gamma}. \tag{3.17}$$

And thus, the final control law can be rewritten as:

$$\begin{aligned} &v_{\text{inv}} = v_{eq} + v_{\text{un}} = -\gamma^{-1}\left(\varphi_1 + \alpha\sqrt{S}\mathrm{sgn}(S) + \beta\int \mathrm{sgn}(S)\,dt\right), \\ &\alpha > \beta > 0. \end{aligned} \tag{3.18}$$

Taking into account the MMC dynamics in (3.4), the reference voltage is calculated as:

$$\vec{\boldsymbol{v}}_{Mdq}^{\Delta} = -L_{eq}^{ac}\dot{\vec{\boldsymbol{S}}}\left(\vec{i}_{dq}^{\Delta}\right) + R_{eq}^{ac}\vec{i}_{dq,ref}^{\Delta} + \omega L_{eq}^{ac}\mathbf{J}_2\vec{i}_{dq,ref}^{\Delta} + \vec{\boldsymbol{v}}_{dq}^{G}, \tag{3.19}$$

$$s\left(\vec{\zeta}_{dq}^{\Delta}, t\right) = k_p\dot{\vec{\zeta}}_{dq}^{\Delta} + k_p\int \vec{\zeta}_{dq}^{\Delta}\,dt. \tag{3.20}$$

Thus, the time derivative of the sliding variable results in

$$\dot{s}(e_{vo},t) = \ddot{e}_{vo} + \lambda\dot{e}_{vo} + \frac{\lambda^2}{4}e_{vo} = \varphi_2 + \gamma v_{inv} + h(t), \tag{3.21}$$

where $\varphi_2 = \varphi_1 + \frac{\lambda^2}{4}e_{vo}$.

The equivalent control law is then

$$\dot{s}(e_{vo},t) = h(t) = 0 \rightarrow \varphi_2 + \gamma v_{eq} = 0 \rightarrow v_{eq} = \frac{-\varphi_2}{\gamma}. \tag{3.22}$$

Again the final control law that must fulfill the attraction of $s(s\dot{s} \leftarrow \eta|s|, s \neq 0, \eta > 0)$ in the presence of uncertainties and disturbances, which can be calculated as follows [53], [93]:

$$v_{inv} = v_{eq} + v_{un} = \frac{-\varphi_2}{\gamma} - \frac{k}{\gamma} \times \text{sgn}(s), \quad k > H + \eta. \tag{3.23}$$

The above SMC is defined as an extension of the grid current controller. Thus, instead of using an active power controller and output grid current controller, the structure relies on the sliding surface, which is defined as an extended output current controller. Namely, the integral sliding surface for the output current's d-q component and the corresponding time derivative is defined as [93], [94]:

$$\begin{aligned} S\left(i_{d,q}^{\Delta}\right) &= i_{d,q,ref}^{\Delta} - i_{d,q}^{\Delta}, \\ \dot{S}\left(i_{d,q}^{\Delta}\right) &= -\dot{i}_{d,q}^{\Delta} = -\sqrt{U}\sqrt{\left|x_{d,q}^{\Delta}\right|}\,\text{sgn}\left(x_{d,q}^{\Delta}\right) - 1.1Ux_{d,q}^{\Delta}, \end{aligned} \tag{3.24}$$

with the positive constant U and where $x_{d,q}$ are the corresponding outputs of the output current controller, defined as follows:

$$\dot{\vec{\zeta}}_{dq}^{\Delta} = \vec{i}_{dq,ref}^{\Delta} - \vec{i}_{dq} \tag{3.25}$$

Taking into account the MMC dynamics, the reference voltage is calculated as follows:

$$\vec{\boldsymbol{v}}_{Mdq}^{\Delta} = -L_{eq}^{ac}\dot{\vec{\mathbf{S}}}\left(\vec{i}_{dq}^{\Delta}\right) + R_{eq}^{ac}\vec{i}_{dq,ref}^{\Delta} + \omega L_{eq}^{ac}\mathbf{J}_2\vec{i}_{dq,ref}^{\Delta} + \vec{\boldsymbol{v}}_{dq}^{G}. \tag{3.26}$$

Since the SMC is a well-known sliding mode control method, and thus, stability proof is avoided here [53].

3.4. MODEL PREDICTIVE CONTROL FORMULATION

MPC is an optimization control approach that can be applied beyond linear systems, with its effectiveness relying on the selection of the cost function. By properly designing the cost function according to the system model, MPC can derive PWM signals without needing a synchronization block.

The MPC [55] is implemented for two cascaded controllers: inner and outer loop. Inner loop MPC controls MMC's currents, while the output loop sets DC voltage. The plant is discretized using the zero-order hold discretization method using an exact solution of the differential equations. Upon discretization, the system is defined with difference equations $\vec{x}(k+1) = A_d\vec{x}(k) + B_d\Delta\vec{u}(k)$, with state variables $\vec{x}$, inputs $\vec{u}$, for k-th instance [55]. Matrices A_d and B_d represent the discrete state and input matrices. The continuous state and input matrices for respective inner and outer loops are defined in the last chapter.

Inputs $\Delta\vec{u}(k)$ are represented using orthonormal Laguerre functions [55]. In orthonormal Laguerre functions, the removal of the dependency on the control horizon gives an advantage for real-time applications, as the number of parameters is reduced. With La-

guerre's function, the control parameter changes to $\vec{\eta}$ from $\Delta\vec{u}(k)$:

$$\Delta\vec{u}(k+m|k) = \begin{bmatrix} L_1(m)^T & o_1^T & \cdots & o_M^T \\ o_1^T & L_2(m)^T & \cdots & o_M^T \\ \vdots & \vdots & \ddots & \vdots \\ o_1^T & o_2^T & \cdots & L_M(m)^T \end{bmatrix} \vec{\eta}, \tag{3.27a}$$

$$L(k+1) = A_l L(k), \tag{3.27b}$$

$$A_l = \begin{bmatrix} a & 0 & 0 & 0 \\ \beta & a & 0 & 0 \\ -a\beta & \beta & a & 0 \\ \vdots & \vdots & \vdots & \ddots \end{bmatrix}, \tag{3.27c}$$

$$L(0) = \sqrt{\beta}\begin{bmatrix} 1 & -a & a^2 & \cdots & (-1)^{N-1}a^{N-1} \end{bmatrix}, \tag{3.27d}$$

$$\vec{\eta} = \begin{bmatrix} c_1 & c_2 & \cdots & c_N \end{bmatrix}^T, \tag{3.27e}$$

where o_k^T represents zero block raw vector with an identical dimension to $L_k(m)^T$. Matrix $L(k) = [l_1(k), l_2(k), \cdots, l_N(k)]^T$, and $l_i(k)$ is the discrete Laguerre function determined using the inverse z transformation of $\Gamma_i(z)$. Function in z domain $\Gamma(z)$ is defined as $\Gamma_i(z) = \Gamma_{i-1}(z)\frac{z^{-1}-a}{1-az^{-1}}$, and $\Gamma_1(z) = \frac{\sqrt{1-a^2}}{1-az^{-1}}$. Here, a is called Laguerre's network pole with a value $0 < a < 1$ for safeguarding the network's stability, $\beta = \sqrt{1-a^2}$, and N is the number of terms required to represent the approximate system response. Notation $\vec{f}(k+m|k)$ denotes discrete value of the vector $\vec{f}$ at the instance $k+m$ estimated during sampling instance k.

The value of η is calculated by minimizing the objective (cost) function, subject to equality and inequality constraints. The cost function is formulated considering the Linear Quadratic Regulator (LQR) as a base. Hence, the cost function is given by [55]:

$$\min_{\vec{\eta}} J = \sum_{m=1}^{N_p} \vec{x}(k+m|k)^T Q\vec{x}(k+m|k) + \vec{\eta}^T R\vec{\eta}, \tag{3.28a}$$

$$\text{subject to } M\vec{\eta} \le b, \tag{3.28b}$$

$$\vec{x}(k+m|k) = \vec{r}(k) - \vec{y}_m(k+m|k), \tag{3.28c}$$

where $Q \succeq 0$ and $R \succ 0$ are weighting matrices, and N_p is the prediction horizon. The terminal constraint $\vec{x}(k+N_p|k)$ is set to = 0. For variables $\vec{x}(k)$, vector $r(k)$ is a reference signal. The matrix M and vector b correspond to constraint information on rate and amplitude as given [95]. Further, the value of input rate and constraints are given by [53]:

$$M = \begin{bmatrix} M_{\Delta U} & o & o & o \\ o & M_{\Delta U} & o & o \\ o & o & -M_U & o \\ o & o & o & -M_U \end{bmatrix}, \quad b = \begin{bmatrix} \Delta U_{max} \\ -\Delta U_{max} \\ U_{max} - \vec{u}(k-1) \\ -U_{min} + \vec{u}(k-1) \end{bmatrix} \tag{3.29}$$

$$M_{\Delta U} = \begin{bmatrix} L_1(m)^T & o & \cdots & o \\ o & L_2(m)^T & \cdots & o \\ \vdots & \vdots & \ddots & \vdots \\ o & o & \cdots & L_m(m)^T \end{bmatrix} \tag{3.30}$$

$$M_U = \begin{bmatrix} \sum_{i=0}^{N-1} L_1(i)^T & o & \cdots & o \\ o & \sum_{i=0}^{N-1} L_2(i)^T & \cdots & o \\ \vdots & \vdots & \ddots & \vdots \\ o & o & \cdots & \sum_{i=0}^{N-1} L_m(i)^T \end{bmatrix} \tag{3.31}$$

$$\begin{aligned} \Delta U_{max} &= 0.3 \times \vec{1}, \quad \Delta U_{min} = 0.3 \times \vec{1} \\ U_{max} &= 0.8 \times \vec{1}, \qquad U_{min} = 0.3 \times \vec{1} \end{aligned} \tag{3.32}$$

where $\vec{1}$ is vector of all ones.

The quadratic programming problem (3.28) is solved by making use of Hildreth's quadratic programming procedure [96]. MPC given with equation (3.28) is stable, which is shown in [95].

INNER MPC LOOP DESIGN

The inner MPC loop is represented in the discretized form as in [95], where the corresponding continuous matrices are:

$$A = \begin{bmatrix} -\frac{R_{arm}}{L_{arm}} & 2\omega & 0 & 0 & 0 \\ -2\omega & -\frac{R_{arm}}{L_{arm}} & 0 & 0 & 0 \\ 0 & 0 & -\frac{R_{arm}}{L_{arm}} & 0 & 0 \\ 0 & 0 & 0 & -\frac{R_{eq}^{ac}}{L_{eq}^{ac}} & -\omega \\ 0 & 0 & 0 & \omega & -\frac{R_{eq}^{ac}}{L_{eq}^{ac}} \end{bmatrix}, \tag{3.33a}$$

$$B = \text{diag}\left\{ -\frac{1}{L_{arm}}, -\frac{1}{L_{arm}}, -\frac{1}{L_{arm}}, \frac{1}{L_{eq}^{ac}}, \frac{1}{L_{eq}^{ac}} \right\}, \tag{3.33b}$$

and vector $\vec{x} = [i_d^{\Sigma}, i_q^{\Sigma}, i_z^{\Sigma}, i_d^{\Delta}, i_q^{\Delta}]^T$ represents continuous state variables, while $\vec{u} = [v_{Md}^{\Sigma}, v_{Mq}^{\Sigma}, v_{Mz}^{\Sigma} - \frac{v_{dc}}{2}, v_{Md} - v_d^{\Delta}, v_{Mq} - v_q^{\Delta}]^T$ represents continuous system inputs.

OUTER MPC LOOP DESIGN

This MPC loop is used to control the DC voltage of the MTDC system. This loop maintains rated DC voltage at MMC1. To make the inner MPC controller dynamic, linearization is avoided. Thus, the outer loop is added to consider other system variables, which indirectly derive the inner MPC loop state variables. The continuous state space representation matrices are [53]:

$$A = \left[\frac{-1}{k_{dc} \times T_{dc}} \right], \quad B = \left[\frac{1}{k_{dc}} \right]. \tag{3.34}$$

The vector $\vec{x} = [v_{dc\,ref} - v_{dc}]$ represents the continuous state variable, while $\vec{u} = \left[i_d^{\Delta}\right]$ represents continuous system input. The k_{dc} and T_{dc} are 6.5 and 0.0035 respectively. The discretization method remains the same as for the inner MPC loop. The cost function minimizes the control signal to eliminate any deviation from the rated DC link voltage.

3.5. CONCLUSION

This chapter introduces the modeling processes for three non-linear control methods: BSC, SMC, and MPC. When compared to traditional PI-based control algorithms, these methods offer faster and more robust transient responses for MMC converters within the context of MTDC systems. The applications of these three non-linear algorithms will serve as valuable references for future multi-vendor MTDC systems. The performance of the MMC controllers, as well as the interoperability between different controllers, will be detailed and demonstrated through various system scenarios in the RTDS environment in Chapter VII.

4

TRAVELING WAVE ANALYSIS IN MTDC GRIDS

This chapter provides a detailed introduction to traveling wave fault analysis for MTDC grids. Applying the Peterson equivalent circuit and the TWs theory, the frequency and time domain expressions of the line-mode voltage TWs and pole voltage TWs measured at different relay units are obtained. By constructing transfer functions, this chapter analyzes the characteristics of measured TWs in the high-frequency domain and their influencing factors. Based on this, the obtained concluding remarks set up the theoretical foundation for designing the protection scheme and fault location algorithm.

Parts of this chapter have been published in [66], [97].

The role of the transient fault analysis is indispensable. By deeply understanding the potential fault scenarios and the characteristics of measured TW signals in relay units, robust protections and accurate fault location algorithms for MTDC systems can be formulated, thereby enhancing the resilience and reliability of the MTDC system.

This chapter deals with a comprehensive TW fault analysis for MTDC systems. Detailed expressions of TWs measured at relay units for both internal and external lines are analyzed. The features of high-frequency components contained in the voltage TWs are identified, which can then be used for the design of the protection method in Chapter V. The detailed expressions of TWs measured at the relays units will be used for the purpose of fault location, which is detailed discussed in Chapter VI.

4.1. TESTING SYSTEM SET UP

A ±525 kV four-terminal meshed MMC-HVDC system with a bipolar configuration is modeled in PSCAD/EMTDC. The presented model is used to study the characteristics of TWs after the DC fault occurrence and to demonstrate the performance of the proposed protection scheme in the Chapter V.

The configuration of the studied MTDC system is shown in Figure 4.1.

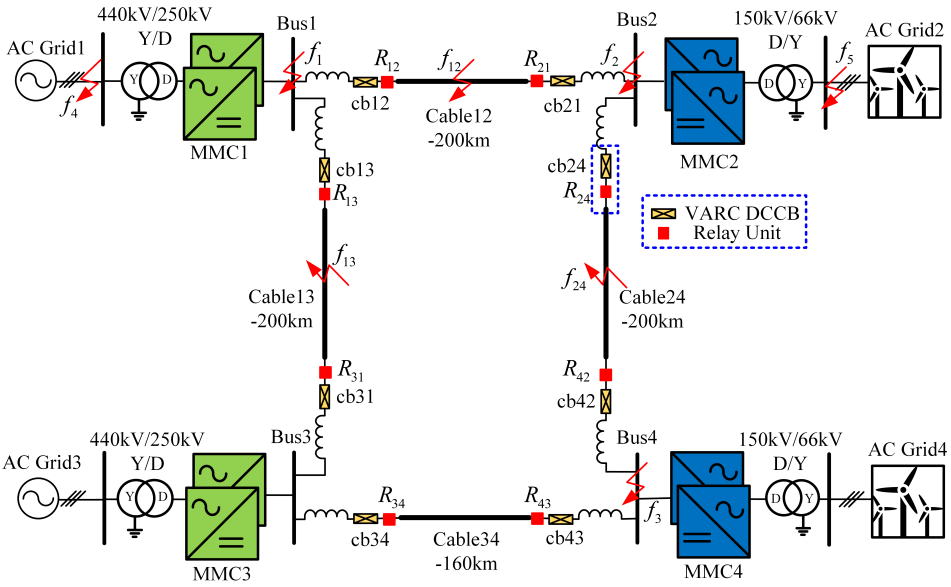

Figure 4.1: Configuration of studied system.

The MMC converters in the studied system connect the AC to the DC grids. Among these, MMC1 and MMC3 have grid-following control regulating the DC voltage and the active power, and the rated capacity is 2000 MW. MMC2 and MMC4 are modeled using the grid-forming control supporting the wind farm energy. The inner and the outer control loops for all MMCs adopt classical PI controls. All converters are with a bipolar

configuration.

At each end of the DC cable, two relay units (denoted in red) are installed both on the positive and the negative poles, respectively. All relay units are used to measure the voltage and current TWs and use the protection scheme explained in Chapter V.

To obtain accurate transient responses of TWs, the transmission lines of the testing system are simulated by applying a frequency-dependent cable model. The configuration of the cable model is based on CIGRE B4.57 [98].

The VARC DCCBs, which are introduced in Chapter II, are implemented at each cable terminal, following the approach proposed in [78]. The protection will trip the corresponding DCCBs to interrupt the fault currents when the DC fault is detected. The VARC DCCB makes use of a vacuum interrupter which has short arcing times, normally in the range of microseconds. Thus, simulations are performed in PSCAD/EMTDC with a solution time step of 1 μs [78] to ensure all important signals of VARC DCCB can be precisely taken into account.

Table 4.1: VARC DCCB Parameters for 525 kV System

Item	L_{dc} (mH)	L_p (μH)	C_p (μF)	Surge arrester (SA) rated voltage (kV)	$V_{in}C_p$ (kV)
320kV [78]	80	300	0.66	320/480	24
525kV	120	492.18	0.40	525/787.5	39.37

The parameters of the current injection branch of the VARC DCCBs reported in [78] are scaled to a 525 kV system and are presented in Table. 4.1, where L_p and C_p are the oscillating inductor and capacitor, respectively. $V_{in}C_p$ is the initial voltage across capacitor C_p. Particularly, the DC inductor, L_{dc}, is set to 120 mH to limit the rate of rise and peak value of the fault current, ensuring that the VARC DCCB can effectively interrupt the fault current.

A comprehensive list of the system parameters in a PSCAD/EMTDC environment can be found in Table. 4.2.

4.2. INITIAL VALUE OF LINE-MODE VOLTAGE AT FAULT POINT

In the symmetrical bipolar power transmission line, the pole voltages and currents are coupled. To simplify the fault analysis, it generally decomposes the bipolar system into its line-zero mode networks. In this way, only the line- or zero-mode component is relevant, which avoids the analysis of the full complexity of the system. Also, by decoupling the system into its zero/line components, it is easier to analyze and understand the behavior of the system during post-fault conditions.

As such, the pole voltages u_p and u_n and currents i_p and i_n can be transformed into zero-mode u_0, i_0 and line-mode components u_1, i_1 via [66], [97]:

$$\begin{bmatrix} u_0 \\ u_1 \end{bmatrix} = \frac{1}{\sqrt{2}} \begin{bmatrix} 1 & 1 \\ 1 & -1 \end{bmatrix} \begin{bmatrix} u_p \\ u_n \end{bmatrix}, \begin{bmatrix} i_0 \\ i_1 \end{bmatrix} = \frac{1}{\sqrt{2}} \begin{bmatrix} 1 & 1 \\ 1 & -1 \end{bmatrix} \begin{bmatrix} i_p \\ i_n \end{bmatrix} \tag{4.1}$$

Table 4.2: Parameters of The Four-terminal HVDC System In Pscad

Item	MMC1&3	MMC2&4
Nominal system frequency (Hz)	50	50
MMC (one pole) rated capacity (MVA)	2000	2000
Transformer ratio (D/Y$_n$)	400/250	66/150
Transformer leakage inductance (p.u.)	0.18	0.18
Number of arm sub-module (SM)	175	175
Arm inductance L_{arm} (mH)	4.2	4.2
Capacitance of each SM $C_{sm}(\mu F)$	15000	15000
On-state arm resistance R_{on} (Ω)	0.001361	0.001361
Arm resistance R_{arm} (Ω)	0.08	0.08
SM capacitor voltage rating (kV)	2.0	2.0
DC inductor L_{dc} (mH)	120	120

As such, the symmetrical bipolar transmission system can be represented as an independent line and a zero-mode network.

By combining the zero- and line-mode sequence network, the initial fault values of the line-mode and zero-mode voltages (Δv_{F1}, Δv_{F0}) at the fault point for a typical pole-to-pole fault (PTP), a positive pole-to-ground (PTG) fault, and a negative pole-to-ground (NTG) fault are listed in Table. 4.3:

Table 4.3: Line- And Zero-Mode Initial Voltages At Fault Point[99], [100]

Item	PTP	PTG	NTG
Δv_{F1}	$\frac{-\sqrt{2}V_f Z_{c(1)}}{Z_{c(1)}+R_f}$	$\frac{-\sqrt{2}V_f Z_{c(1)}}{Z_{c(1)}+Z_{c(0)}+4R_f}$	$\frac{-\sqrt{2}V_f Z_{c(1)}}{Z_{c(1)}+Z_{c(0)}+4R_f}$
Δv_{F0}	0	$\frac{-\sqrt{2}V_f Z_{c(0)}}{Z_{c(1)}+Z_{c(0)}+4R_f}$	$\frac{\sqrt{2}V_f Z_{c(0)}}{Z_{c(1)}+Z_{c(0)}+4R_f}$

where V_f denotes the rated DC line voltage, R_f, refers to fault resistance, $Z_{c(1)}$ and $Z_{c(0)}$ represent the line- and zero-mode characteristic impedances, respectively. For the used cable model, we have $Z_{c(1)} = 60.714\Omega$, and $Z_{c(0)} = 169.587\Omega$.

In the subsequent analysis of this Chapter, the line-mode components are used to highlight the propagation characteristics of TWs for the following reasons:

1. From Table. 4.3, it is evident that the initial value of the zero-mode components, Δv_{F0} is always zero for the PTP fault type. Consequently, in the zero-mode network, the zero-mode voltage/current TWs are also zero. This makes Δv_{F0} unsuitable for distinguishing PTP faults and used for the fault location analysis.

2. In the TWs propagation process, the line-mode components have smaller attenuation constants and higher propagation velocities than the zero-mode compo-

nents. Consequently, the line-mode components reach the relay units faster than the zero-mode components, leading to faster protection detection and tripping of the DCCBs.

4.3. EXPRESSION OF LINE-MODE COMPONENTS AT INTERNAL AND EXTERNAL MEASURING RELAYS

For the case study elaborated in this Chapter, cable 12 in Figure 4.1 is selected to be the faulty cable. Accordingly, R_{12} and R_{21} are the observed relay units. Figure 4.2 describes the lattice diagram of an internal DC fault f_{12} in the line-mode network.

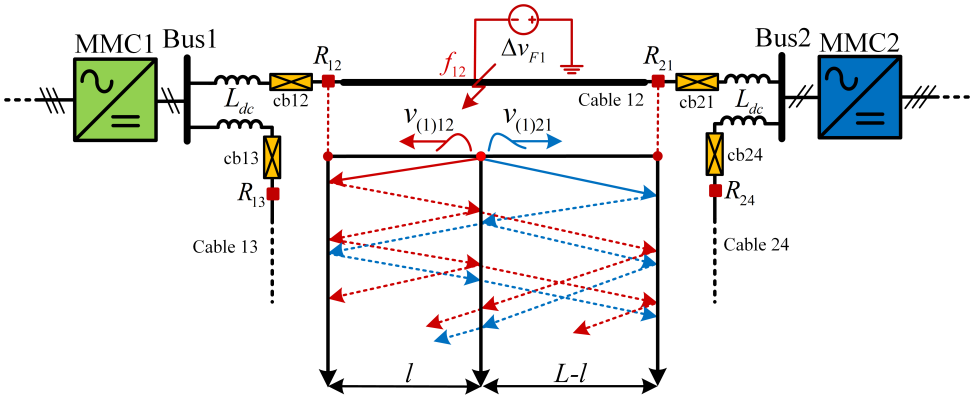

Figure 4.2: Lattice diagram for a cable fault in the line-mode network.

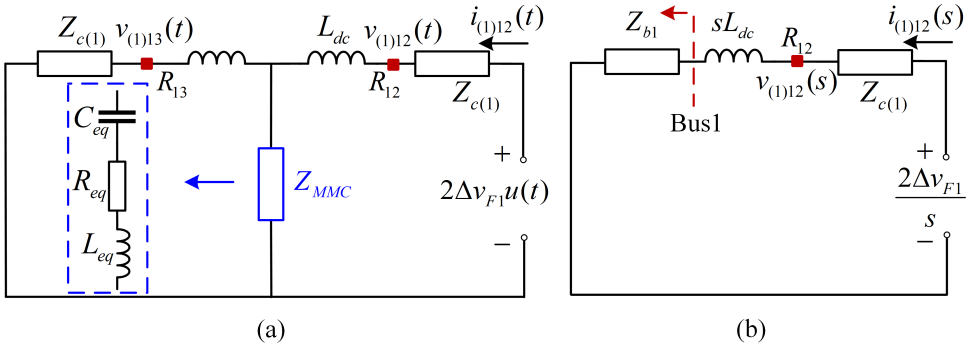

Figure 4.3: (a) *Peterson* equivalent circuit; and (b) simplified circuit in S-domain.

In Figure 4.2, the fault f_{12} occurs at a distance l from relay unit R_{12}. According to the superposition theorem, the fault can be regarded as a reverse voltage source with a value of Δv_{F1}. The fault-induced voltage TWs in the line-mode network, $v_{(1)12}$, and $v_{(1)21}$ are initiated at the fault point and propagate along the cable toward the cable terminal.

When the wave impedance is not continuous, the TWs will be partly reflected back to the fault point and partly injected into the MMC converter and neighboring cables.

The corresponding line-mode fault components of the *Peterson* equivalent circuit and its simplified circuit can be seen in Figure 4.3. In Figure 4.3(a), the voltage source is two times the initial voltage Δv_{F1} at the fault inception point. Z_{MMC} represents the equivalent impedance of the MMC converter, which is modeled as a series RLC circuit [101]:

$$R_{eq} = \frac{2(R_{arm} + R_{on})}{3}, \quad L_{eq} = \frac{2L_{arm}}{3}, \quad C_{eq} = \frac{6C_{sm}}{N}, \tag{4.2}$$

where R_{eq}, L_{eq}, and C_{eq} represent the MMC equivalent resistance, inductance, and capacitance, respectively. According to the values shown in Table. 4.2, $R_{eq} = 0.0542\Omega$, $C_{eq} = 0.5142 \times 10^3 \mu$F, $L_{eq} = 2.8$mH in the studied system.

By applying the *Laplace* transform to the circuit, the MMC impedance can be simplified as $Z_{MMC}(s) = 1/sC_{eq} + sL_{eq}$, as the impact of R_{eq} is negligible. The impact of VARC DCCB is neglected in Figure 4.3(a) as the DCCB is not initialized by the protection before the measured line-mode voltage TW arrives at the relay. Therefore, the circuit shown in Figure 4.3(a) can be simplified by defining equivalent impedance Z_{b1} at bus1 as:

$$Z_{b1} = \frac{(Z_{c(1)} + sL_{dc})\left(\frac{1}{sC_{eq}} + sL_{eq}\right)}{Z_{c(1)} + sL_{dc} + \frac{1}{sC_{eq}} + sL_{eq}} \tag{4.3}$$

According to Figure 4.3(b), one can obtain the S-domain expression for the line-mode voltage $v_{(1)12}(s)$ as follows:

$$\begin{aligned} v_{(1)12}(s) &= \frac{2\Delta v_{F1}}{s}\left(1 - \frac{Z_{c(1)}}{Z_{c(1)} + sL_{dc} + Z_{b1}}\right) \\ &= \frac{2\Delta v_{F1}}{s}\left(1 - \frac{Z_{c(1)}(s - z_1)(s - z_2)}{(Z_{c(1)} + sL_{dc})(s - p_1)(s - p_2)}\right), \end{aligned} \tag{4.4}$$

where z_1, z_2, p_1, and p_2 in (4.4) are calculated as follows:

$$\begin{cases} z_{1,2} = \dfrac{-Z_{c(1)}C_{eq} \pm \sqrt{(Z_{c(1)}C_{eq})^2 - 4C_{eq}(L_{dc} + L_{eq})}}{2C_{eq}(L_{dc} + L_{eq})}, \\ p_{1,2} = \dfrac{-Z_{c(1)}C_{eq} \pm \sqrt{(Z_{c(1)}C_{eq})^2 - 8C_{eq}(L_{dc} + 2L_{eq})}}{2C_{eq}(L_{dc} + 2L_{eq})}. \end{cases} \tag{4.5}$$

For the studied system, the following parameters are applied: $L_{dc} = 120$mH, $Z_{c(1)} = 60.714\Omega$. As such, one can obtain that: $Z_{c(1)}^2 C_{eq}^2 = 947.63 \times 10^6 \gg 8C_{eq}(2L_{eq} + L_{dc}) = 516.67 \times 10^3 > 4C_{eq}(L_{dc} + L_{eq}) = 252.57 \times 10^3$. Accordingly, the roots in (4.5) can be simplified as: $z_1 = p_1 \approx 0$, $z_2 \approx -Z_{c(1)}/(L_{dc} + L_{eq})$, $p_2 \approx -Z_{c(1)}/(L_{dc} + 2L_{eq})$. Thereby, we have:

$$v_{(1)12}(s) = \frac{2\Delta v_{F1}}{s}\left(1 - \frac{Z_{c(1)}(s + \frac{Z_{c(1)}}{L_{dc}+L_{eq}})}{(Z_{c(1)} + sL_{dc})(s + \frac{Z_{c(1)}}{L_{dc}+2L_{eq}})}\right). \tag{4.6}$$

Given that $L_{dc}+L_{eq}$=122.8 mH $\approx L_{dc}+2L_{eq}$ = 125.6 mH. We can further simplify (4.6) as:

$$v_{(1)12}(s)=\frac{2\Delta v_{F1}}{s}\cdot\left(1-\frac{Z_{c(1)}}{Z_{c(1)}+sL_{dc}}\right). \tag{4.7}$$

To describe the attenuation effect of TWs along the traveling distance l, an exponential propagation function $e^{-\Gamma(s)l}$ [97], [102] is introduced:

$$e^{-\Gamma_1(s)l}=e^{-\sqrt{(r_0+sl_0)(g_0+sc_0)}l}\approx\frac{1-k_1 l}{1+s\cdot\tau_1 l}\cdot e^{-s\cdot\frac{l}{v_{(1)}}}, \tag{4.8}$$

where $\Gamma_1(s)l$ is the line-mode TW propagation coefficient representing the attenuation effect and phase shift along with traveling distance l. r_0, l_0 are the per-unit line resistance and inductance, and g_0, c_0 are the per-unit line-to-ground conductance and capacitance, respectively. $v_{(1)}$ is the propagation velocity of the line-mode TWs in the cable. The values for k_1 and τ_1 in [103] are modified into $k_1=5\times10^{-5}$/km, and $\tau_1=1.5\times10^{-8}$s/km considering the different distributed parameters between the DC cable and overhead line.

As such, the expression of $v_{(1)12}(s)$ with the fault distance l becomes:

$$v_{(1)12}(s)=\frac{2\Delta v_{F1}}{s}\left(1-\frac{Z_{c(1)}}{Z_{c(1)}+sL_{dc}}\right)\frac{1-k_1 l}{1+s\tau_1 l}e^{-s\frac{l}{v_{(1)}}}. \tag{4.9}$$

Due to the symmetrical system topology, the expression for $v_{(1)21}(s)$ monitored at relay unit R_{21} can be obtained by replacing l with $(L-l)$ in (4.9) as follows:

$$v_{(1)21}(s)=\frac{2\Delta v_{F1}}{s}(1-\frac{Z_{c(1)}}{Z_{c(1)}+sL_{dc}})\frac{1-k_1(L-l)}{1+s\tau_1(L-l)}e^{-s\frac{L-l}{v_{(1)}}}. \tag{4.10}$$

To obtain the time-domain expression for $v_{(1)12}(t)$, the $v_{(1)12}(s)$ in (4.9) could be rewritten as:

$$v_{(1)12}(s)=\left(\frac{A_1}{s+B_1}+\frac{A_2}{s+B_2}\right)\cdot e^{-s\cdot T_{d0}}, \tag{4.11}$$

where in (4.11), the items are calculated as follows:

$$\begin{cases} A_1=\dfrac{2\Delta v_{F1}(1-k_1 l)L_{dc}}{L_{dc}-Z_{c(1)}\tau_1 l}, B_1=\dfrac{Z_{c(1)}}{L_{dc}}, B_2=\dfrac{1}{\tau_1 l}, \\ A_2=\dfrac{2\Delta v_{F1}(1-k_1 l)L_{dc}}{Z_{c(1)}\tau_1 l-L_{dc}}, T_{d0}=l/v_{(1)}. \end{cases} \tag{4.12}$$

Using the Inverse *Laplace* Transform, we obtain the following time-domain expression for $v_{(1)12}(t)$:

$$\begin{aligned} v_{(1)12}(t)&=\left(A_1 e^{-B_1(t-T_{d0})}+A_2 e^{-B_2(t-T_{d0})}\right)u(t-T_{d0}) \\ &=\frac{2\Delta v_{F1}(1-k_1 l)L_{dc}}{L_{dc}-Z_{c(1)}\tau_1 l}\left(e^{-\frac{t-T_{d0}}{L_{dc}/Z_{c(1)}}}-e^{-\frac{t-T_{d0}}{\tau_1 l}}\right)u(t-T_{d0}). \end{aligned} \tag{4.13}$$

In (4.13), it is evident that the time domain expression of $v_{(1)12}(t)$ contains two exponential functions $A_1 e^{-B_1(t-T_{d0})}$ and $A_2 e^{-B_2(t-T_{d0})}$, resulting from the line boundary characteristics and line propagation characteristics, respectively.

Combining (4.13) and Table. 4.3, the amplitude of $v_{(1)12}(t)$ is affected by the fault type, fault distance l and fault resistance R_f, and size of L_{dc}.

To be specific:

1. The fault type affects the initial value of Δv_{F1}, as summarized in Table. 4.3. The PTP fault has higher initial values than the PTG and NTG faults.

2. The fault location l also affects the amplitude of the line-mode voltage. The larger the value of fault distance l, the smaller the amplitude of $v_{(1)12}$ measured at relay units due to the propagation attenuation.

Due to the symmetrical configuration, the above-analyzed features apply to line-mode voltage TWs measured in cable 24 and cable 34.

In order to satisfy the selectivity requirement of the protection, the analysis of TWs signals detected by external protections is also very important. The difference in measured signals between internal and external relays will be the core of the protection design.

A part of the TWs initiated by f_{12} at the fault point propagates into the neighboring cables.

According to Figure 4.3(a), $i_{(1)12}(s)$ can be expressed as:

$$i_{(1)12}(s) = \frac{2\Delta v_{F1}}{s(Z_{c(1)} + sL_{dc})} \cdot \frac{1 - k_1 l}{1 + s\tau_1 l} \cdot e^{-s \cdot \frac{l}{v_{(1)}}}. \tag{4.14}$$

Accordingly, $v_{(1)13}(s)$ measured at R_{13} is calculated as:

$$\begin{aligned} v_{(1)13}(s) &= \left(\frac{2\Delta v_{F1}}{s} - (Z_{c(1)} + sL_{dc}) i_{(1)12}(s) \right) \frac{Z_{c(1)}}{Z_{c(1)} + sL_{dc}} \\ &= \frac{2\Delta v_{F1} Z_{c(1)}}{s(Z_{c(1)} + sL_{dc})} \left(1 - \frac{1 - k_1 l}{1 + s\tau_1 l} e^{-s \cdot \frac{l}{v_{(1)}}} \right). \end{aligned} \tag{4.15}$$

4.4. DIFFERENCE OF HIGH-FREQUENCY COMPONENTS IN INTERNAL AND EXTERNAL LINE-MODE VOLTAGE TWS

By combining (4.9) and (4.15), the transfer function $H(s)$ representing the boundary effects of L_{dc} can be expressed as:

$$H(s) = \frac{v_{(1)12}(s)}{v_{(1)13}(s)} = \frac{1 - k_1 l}{k_1 l + s\tau_1 l} \cdot \frac{sL_{dc}}{Z_{c(1)}}. \tag{4.16}$$

To analyze the frequency-magnitude response, $H(j\omega)$ can be expressed as:

$$\begin{aligned} H(j\omega) &= \frac{(1 - k_1 l) L_{dc} j\omega}{\tau_1 l Z_{c(1)} j\omega + k_1 l Z_{c(1)}}, \\ \lim_{\omega \to \infty} |H(j\omega)| &= \frac{(1 - k_1 l) L_{dc}}{\tau_1 l Z_{c(1)}}. \end{aligned} \tag{4.17}$$

The magnitude of the frequency response of $H(j\omega)$ is shown in Figure 4.4 for different L_{dc} and fault distance l (where k_1 and τ_1 are constants in equation (4.17)). The L_{dc},

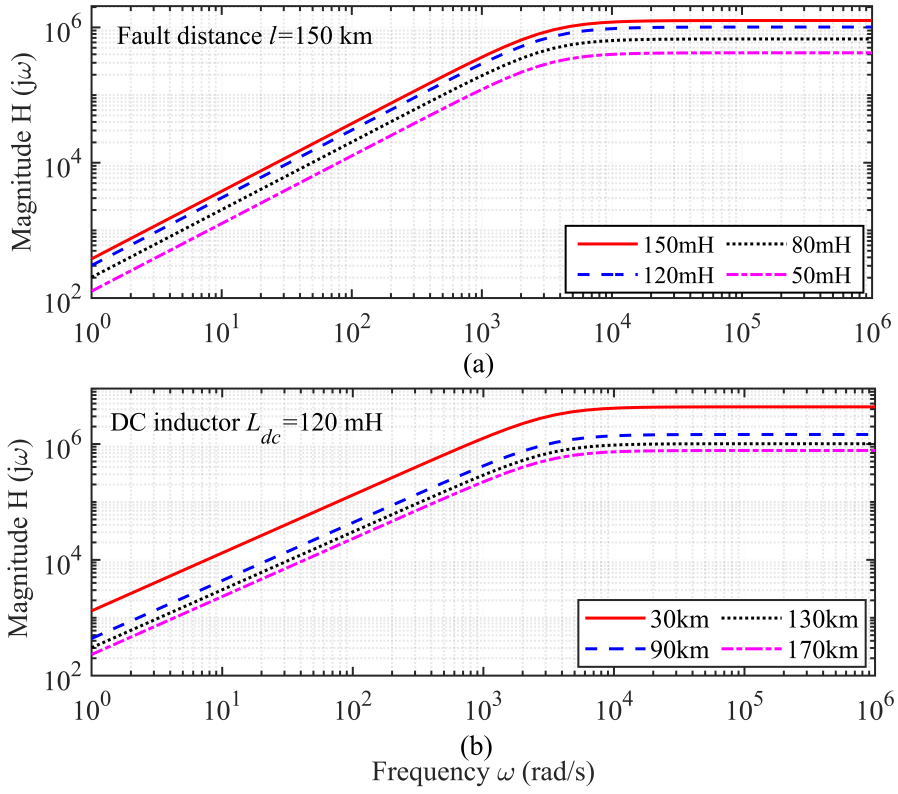

Figure 4.4: Magnitude-frequency response of $H(j\omega)$: (a) Impact of DC inductor L_{dc}; (b) Impact of fault distance l.

as a boundary element, filters out high-frequency components in $v_{(1)13}(s)$, which are measured at the external relays, leading to a significant difference in frequency response between $v_{(1)12}(s)$ and $v_{(1)13}(s)$.

In light of (4.17) and Figure 4.4, we can draw the conclusion that:

1. The magnitude of $H(j\omega)$ is influenced by the value of L_{dc} in the high-frequency range when $\omega = 2\pi f \to \infty$. As L_{dc} increases, the amplitude of the high-frequency components in $v_{(1)12}(s)$ increases, whereas the amplitude of $v_{(1)13}(s)$ decreases. Conversely, as L_{dc} decreases, the opposite effect is observed;

2. The fault location l also impacts $H(j\omega)$ by determining the extent of the attenuation of the TWs propagation process. A smaller value of l results in a higher amplitude of high-frequency components in $v_{(1)12}(s)$ and a lower amplitude in $v_{(1)13}(s)$, while the opposite is observed for a larger value of l;

3. When the size of L_{dc} is increased, the sensitivity and selectivity performance of the protection will also increase. This is because L_{dc} significantly impacts the transfer

function $H(j\omega)$ characteristics and the high-frequency components. In contrast, the opposite is observed for a smaller value of L_{dc}.

4. These characteristics hold for all fault types and other relays as well.

To demonstrate this, a PTP fault is applied at 1.2s in cable12. The waveforms of the line-mode voltages $v_{(1)12}$ and $v_{(1)13}$ and their high-frequency (HF) components are simulated in Figure 4.5. It is obvious that $v_{(1)12}$ experiences a deep sag due to the attenuation that takes place during the propagation process through cable12, whilst measured voltage $v_{(1)13}$ in the healthy cable13 is slightly affected by the fault. Voltage $v_{(1)12}$ consists of abundant frequency information, and its high-frequency component HF$v_{(1)12}$ will emerge and rise instantly to a distinguishable value when the TWs arrive at the relay unit. In contrast, the magnitude of the HF$v_{(1)13}$ is much smaller than that of a faulty cable12.

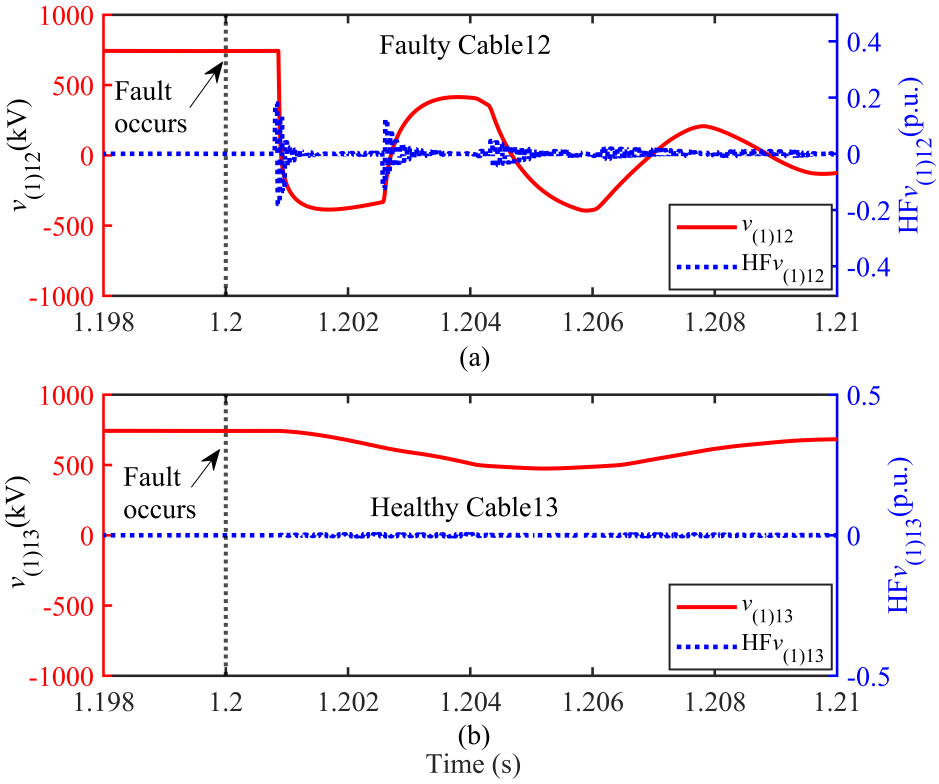

Figure 4.5: Simulation of line-mode voltage and its high-frequency components. (a).V_{112} in faulty cable12. (b). V_{113} in healthy cable13.

4.5. DIFFERENCE OF HIGH-FREQUENCY COMPONENTS IN FAULTY AND HEALTHY POLE VOLTAGES

The pole voltage of both positive and negative poles will dampen immediately after the PTP fault and have symmetrical waveforms. In the case of PTG or NTG fault, only the faulty pole voltage will decrease to zero instantaneously, whilst the non-faulty pole voltage is marginally damped.

To discriminate the fault type, this section studies the expressions of the voltages TWs measured at the positive and negative poles. Then, the features contained in the pole voltage TWs are analyzed.

According to (4.9) and Table. 4.3, the zero-mode voltage $v_{(0)12}(s)$ can be expressed as:

$$v_{(0)12}(s) = \frac{2\Delta v_{F0}}{s}\left(1 - \frac{Z_{c(0)}}{Z_{c(0)} + sL_{dc}}\right)\frac{1 - k_0 l}{1 + s\tau_0 l}e^{-s\frac{l}{v_{(0)}}}, \tag{4.18}$$

where $v_{(0)}$ is the propagation velocity of zero-mode TWs in the cable. The values are $k_0 = 7 \times 10^{-5}$/km, and $\tau_0 = 1.2 \times 10^{-8}$s/km as the zero-mode TWs have smaller velocity and larger attenuation constant.

By applying the mode-to-pole transformation (inverse of (4.1)), the pole voltages v_{p12}, v_{n12} are:

$$v_{p12} = \frac{v_{(0)12} - v_{(1)12}}{\sqrt{2}}, \qquad v_{n12} = \frac{v_{(1)12} + v_{(0)12}}{\sqrt{2}}. \tag{4.19}$$

By combining (4.9), (4.18) and (4.19) yields that:

$$\begin{cases} v_{p12}(s) = \dfrac{1}{\sqrt{2}}\left(\dfrac{2\Delta v_{F0}}{s}\dfrac{sL_{dc}}{Z_{c(0)} + sL_{dc}}\dfrac{1 - k_0 l}{1 + s\tau_0 l}e^{-s\frac{l}{v_{(0)}}} - \dfrac{2\Delta v_{F1}}{s}\dfrac{sL_{dc}}{Z_{c(1)} + sL_{dc}}\dfrac{1 - k_1 l}{1 + s\tau_1 l}e^{-s\frac{l}{v_{(1)}}}\right), \\ v_{n12}(s) = \dfrac{1}{\sqrt{2}}\left(\dfrac{2\Delta v_{F1}}{s}\dfrac{sL_{dc}}{Z_{c(1)} + sL_{dc}}\dfrac{1 - k_1 l}{1 + s\tau_1 l}e^{-s\frac{l}{v_{(1)}}} + \dfrac{2\Delta v_{F0}}{s}\dfrac{sL_{dc}}{Z_{c(0)} + sL_{dc}}\dfrac{1 - k_0 l}{1 + s\tau_0 l}e^{-s\frac{l}{v_{(0)}}}\right). \end{cases} \tag{4.20}$$

According to Table 4.3 and (4.20), Δv_{F0} is zero in the case of PTP fault. Thus, we have: $v_{p12}(s) = v_{n12}(s) = \frac{1}{\sqrt{2}}v_{(1)12}(s)$. The pole voltages $v_{p12}(s)$ and $v_{n12}(s)$ will drop rapidly when the TWs arrive at R_{12} and present a symmetrical transient behavior. While in the case of PTG or NTG fault, only the faulty pole voltage will decrease to zero instantaneously, whilst the non-faulty pole voltage is marginally damped.

If we neglect the attenuation effect of TWs in (4.20), we have the transfer function $G_{pn}(s) = v_{p12}(s)/v_{n12}(s)$ as:

$$\lim_{s\to\infty}|G_{pn}(s)| = \lim_{s\to\infty}\left|\frac{v_{p12}(s)}{v_{n12}(s)}\right| = \begin{cases} 1, & \text{PTP} \\ \left|\frac{Z_{c(0)} + Z_{c(1)}}{Z_{c(0)} - Z_{c(1)}}\right|, & \text{PTG} \\ \left|\frac{Z_{c(0)} - Z_{c(1)}}{Z_{c(0)} + Z_{c(1)}}\right|, & \text{NTG} \end{cases} \tag{4.21}$$

where $Z_{c(1)} = 60.714\Omega, Z_{c(0)} = 169.587\Omega$ in the tested cable.

As seen in (4.21), the magnitude of $|G_{pn}(s)|$ varies depending on the fault types when $s \to \infty$. The high-frequency components present in the voltage waveforms of the faulty

pole exhibit a larger amplitude than those of the healthy pole. To investigate this, three typical faults (PTP/ PTG/ NTG) are applied at 1.2s in cable12, and the waveforms of pole voltages v_{p12}, v_{n12} as well as their high-frequency components are demonstrated in Figure 4.6.

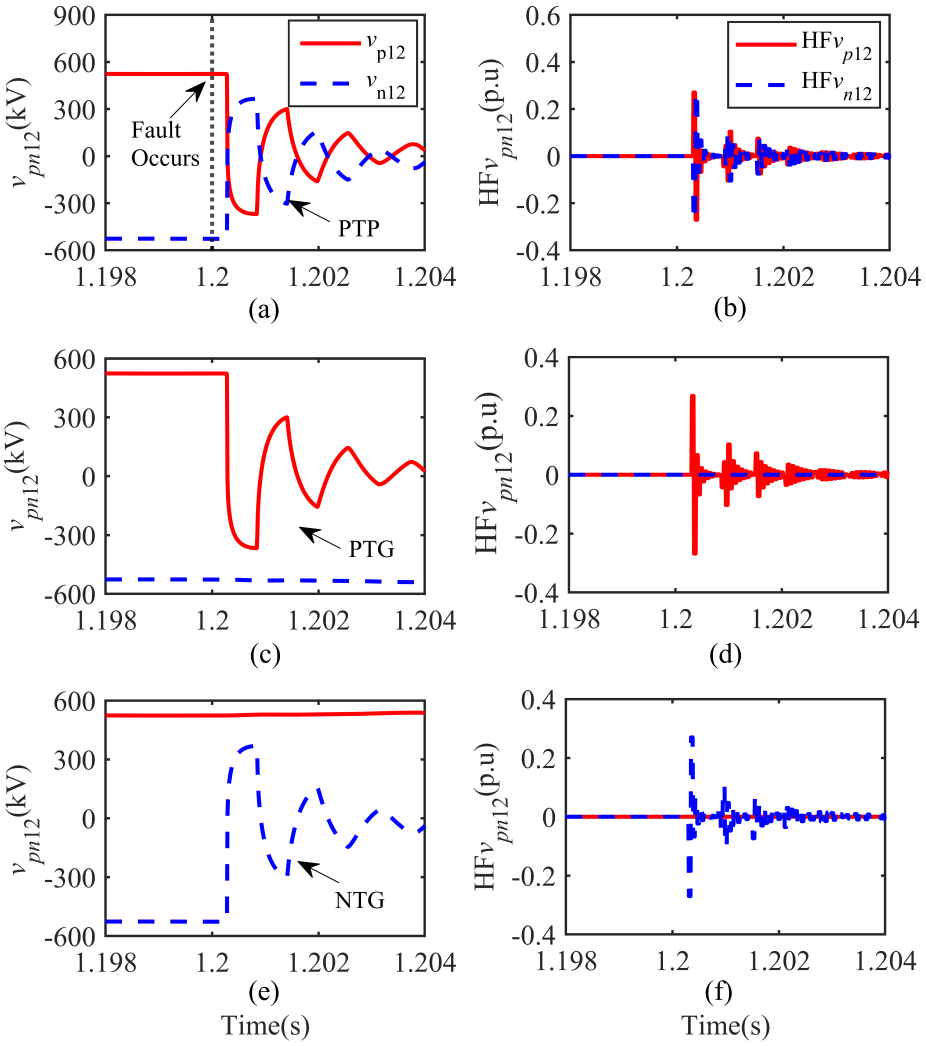

Figure 4.6: Simulation of pole voltage and its high-frequency components.

From Figure 4.6.(a), when the PTP fault occurs at cable12, the positive and negative pole voltages will drop rapidly when the TWs arrive at the relay unit R_{12}. The high-frequency components are seen in Figure 4.6.(b). Since the fault type is a PTP fault, the transient behavior of the positive and negative poles presents a symmetrical trend. How-

ever, in the case of a PTG or an NTG fault in Figure.4.6, the damping is only present in the faulty pole, and the non-faulty pole voltage is minimally affected by the fault. The results are in good agreement with the theoretical analysis in (4.21). It is shown that the high-frequency component surge immediately discriminates between the faulty and the non-faulty pole. By taking into account this feature, the specific fault type can be distinguished.

4.6. CONCLUSION

This chapter provides a detailed TWs fault analysis in an MTDC system. The main findings of the features of the high-frequency components contained in TWs will provide the base of the protection scheme design in Chapter V. The expressions of the TWs provide meaningful information for the fault location study in Chapter VI.

For an MTDC system, using the *Peterson* circuit and the decoupled line-mode network can effectively analyze the frequency domain expressions of the voltage and current TWs measured at different relay units. By using the inverse *Laplace* transform, the time-domain expressions are also easily elaborated. This analytical approach also applies to MTDC systems with different topological structures.

After analyzing the expression of line-mode voltages TWs for internal and external relays, the corresponding magnitude-frequency response $H(j\omega)$ can be constructed. It can be observed that the boundary component L_{dc} filters the high-frequency components contained in the TWs. As such, the high-frequency components only exist in the voltage TWs in internal faulty lines. When the frequency ω tends towards infinity (high-frequency range), this feature becomes even more apparent. Furthermore, the magnitude of the high-frequency components is also influenced by other factors, such as the fault distance, fault resistance, and DC inductor L_{dc}. As such, the faulty area can be discriminated against by the high-frequency components contained in line-mode voltages. Based on the expression of line/zero mode voltage TWs, the detailed expressions of the pole voltages in frequency and time domain can also be obtained. The features of the high-frequency components are analyzed by constructing the transfer function $G_{pn(s)}$. It is concluded that the high-frequency components only exist in the faulty poles. As a result, the fault type can be determined using the high-frequency components contained in the pole voltages. Besides, the detailed expressions of line mode TWs measured at the relay's locations contain the fault location l. These expressions will be further extended and studied in Chapter VI for the purpose of fault location algorithm design.

5

DETERMING AND VALIDATING THE PROPOSED DWT-BASED PROTECTION SCHEME

This chapter introduces the proposed Discrete Wavelet Transform (DWT)-based protection scheme and validates its robustness on PSCAD. Firstly, this chapter introduces the DWT as a time-frequency signal analysis tool to extract the high-frequency components used for measuring TWs. Then, a DWT-based protection scheme for MTDC systems is explained in detail, including its working steps and thresholds selecting principles. Numerous simulations have been performed to validate the robustness of the protection in a four-terminal MTDC system on PSCAD. Furthermore, the proposed protection scheme is compared to existing ones. The results indicate a superior performance of the developed protection scheme over the existing methods in terms of selectivity and sensitivity.

Parts of this chapter have been published in [66].

In Chapter IV, it was demonstrated that high-frequency components contained in the line-mode voltage TWs and pole voltages can be used to detect faulty lines and fault types. Based on these findings, this chapter introduces the proposed protection scheme, explains its robustness, and compares it with presently available methods.

This chapter is organized as follows. Section 5.1 introduces the DWT-based signal analyzing tool, including the mother wavelet selection and signal decomposition level settings. Section 5.2 and 5.3 describe the proposed protection scheme, including the protection working principles and threshold determinations. Section 5.4 validates the performance of the protection scheme in a PSCAD environment. Section 5.5 compares the proposed protection method with the existing methods. Finally, conclusions are elaborated in Section 5.6.

5.1. DWT-BASED SIGNAL ANALYZING TOOL

5.1.1. INTRODUCTION OF DWT AND MOTHER WAVELET SELECTION

The DWT is selected as a signal-processing tool. The DWT is a mathematical tool that decomposes signals into different frequency components or scales. It offers a multi-resolution analysis, which breaks down a signal into both its low-frequency and high-frequency components.

Compared to other signal-analyzing tools, the DWT-based method is computationally efficient in the time-frequency analysis for fault detection and has high computational speed and data compression capability for signal edge detection. To be specific:

1. The DWT offers the multi-resolution analysis of signals, which can decompose the measuring TWs with frequency bands and with different levels of time resolution. This is particularly useful for analysing fast incidental transient signals (e.g., voltage/current TWs after fault) that can decompose them promptly, as the DWT can capture these changes very fast, reducing the computational burden significantly. Other transforms like HHT and *S*-transform use fixed frequency bands and require the computation of the HHT or the FT at each frequency, and therefore is DWT much faster.

2. The DWT is based on a set of filter banks, which can efficiently compute the wavelet coefficients at different decomposition levels and requires fewer operations than HHT, *S*-transform and EMD-based methods.

3. The DWT is widely used and has many available libraries and different software packages. This reduces the computational burden compared to HHT, *S*-transform, and EMD-based methods, which makes it preferred for researchers and engineers to apply DWT-based protections in practice and research.

For a given discrete signal $f(k)$, the DWT algorithm can be obtained as,

$$DWT(f,m,n) = \frac{1}{\sqrt{a_0^m}} \sum_k f(k) \Psi^* \left(\frac{n - k b_0 a_0^m}{a_0^m} \right) \tag{5.1}$$

where Ψ is the selected mother wavelet, and the asterisk denotes a complex conjugate parameter. m and n are the scale and translation parameters. The wavelet function Ψ

would be shifted and scaled by factors a_0 and b_0, respectively. In this work, we adopt $a_0 = 2$ and $b_0 = 1$ [104] to ensure compatibility with the standard wavelet function of the "Haar" wavelet [105].

The actual implementation of the DWT is achieved by using the Dyadic Mallet Tree algorithm, which is depicted in Figure 5.1. The signal $f(k)$ is repeatedly decomposed by cascaded high- and low-pass filters ($H(k)$ and $L(k)$). To enhance the frequency resolution and ensure the time localization of each scaled level, the results after both high- and low-pass filters are down-sampled with a factor of two.

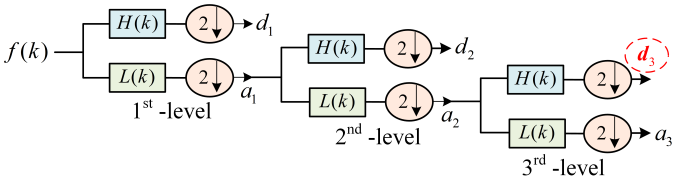

Figure 5.1: Schematic Diagram of Mallet Tree of DWT.

The mother wavelet is the basic waveform used in DWT in (5.1). Its shape and properties determine how the discrete signal $f(k)$ is decomposed into varied frequency components. By translating and scaling this wavelet, the DWT captures both global trends and details in signals, making the mother wavelet's selection crucial for accurate analysis.

Compared to other mother wavelets, such as 'Daubechies', 'Symlets', and 'Coiflets', the Haar wavelet is selected as the mother wavelet due to the following benefits [105] :

1. The Haar wavelet is a simple piecewise constant wavelet, making it a preferred choice for real-time applications where computational efficiency and easy implementation is required;

2. It performs well for edge detection, as it can detect changes in the signal that occur over time.

5.1.2. DECOMPOSITION LEVEL AND SAMPLING FREQUENCY OF DWT

The proposed algorithm utilizes the 3^{rd} scale detailed coefficients for fault detection. Taking the $v_{(1)12}$ as an example, the high-frequency components at different decomposed levels extracted by DWT can be seen in Figure 5.2.

The choice of the data decomposition level is a trade-off between the frequency resolution of decomposed detailed coefficients and the robustness of the protection algorithm against noise interference. Considering that the high-pass filters will add a time advance for the processed data, the higher level (e.g. 4^{th},5^{th}) decomposed detailed coefficients fail to represent the accurate TWs arriving time. In addition, the waveforms of these high-level decomposed coefficients are close to the stepped signals presenting low-resolution problems, which are not suitable for protection design. The lower-level (e.g. 1^{st}, 2^{nd}) decomposed detailed coefficients require high-sampling frequency for measurements and are sensitive to noise intervention.

In this analysis, the sampling frequency of the DWT is set to 100 kHz. This is because a low sampling frequency reduces the resolution of the high-frequency components and increases the time delay introduced by DWT, which ultimately impacts the performance of the protection scheme in terms of speed, sensitivity, and selectivity.

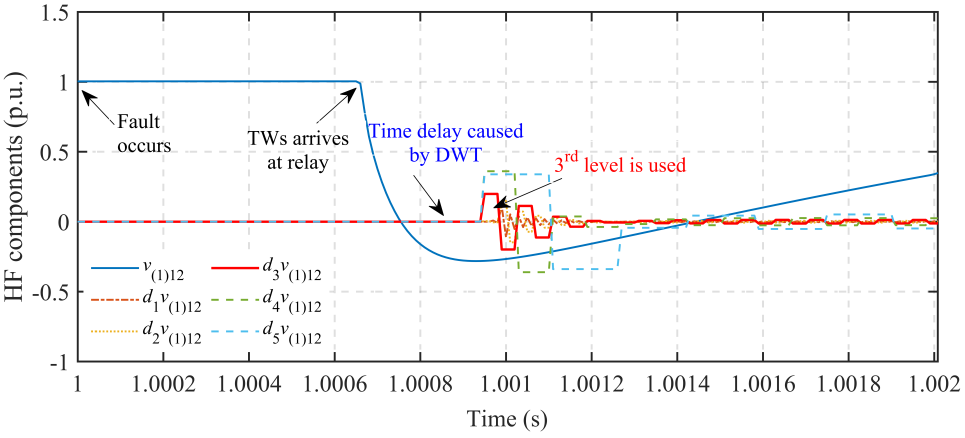

Figure 5.2: The 3-rd level of high-frequency component extracted by DWT.

5.2. DWT-BASED PROTECTION ALGORITHM

This section introduces the proposed protection scheme and the principle of selecting the thresholds.

Step 1: Protection Start-up Criterion

The protection is activated by a start-up criterion, which works according to the following logic. When a DC fault occurs in the system, the DC voltage $V_{dc,ij}$ will drop immediately. Thus, the protection start-up criterion can be established by applying the DC under-voltage detection criterion, which can be expressed as:

$$|V_{dc,ij}| = |v_{p,ij} - v_{n,ij}| < V_{dc,Thre} \tag{5.2}$$

where $V_{dc,Thre}$ denotes the threshold for start-up criterion.

Step 2: Fault Area Detection Criterion

The fault area detection criterion is based on the maximum absolute value of the high-frequency components contained in the line-mode voltage.

The high-frequency components of each decomposed line-mode voltage are denoted as $d_3v_{(1)ij}$ $(i, j = 1, 2, 3, 4)$. The detailed criterion to identify the faulty area can be expressed as follows:

$$\left|d_3v_{(1)ij}\right| > d_3v_{(1)ij,Thre} \tag{5.3}$$

where $d_3v_{(1)ij,Thre}$ denotes the threshold for fault area detection criterion.

Step 3:Fault Type Identification Criterion

The DWT is also utilized to extract the high-frequency components $d_3v_{p,ij}$ and $d_3v_{n,ij}$ contained in the pole voltages. To discriminate the specific fault type, the wavelet energy difference ΔE_{ij} between positive and negative poles is calculated by:

$$\begin{aligned} Ed_3v_{pn,ij} &= \sum_{k=1}^{K=10} \left(d_3v_{pn,ij}(k)\right)^2 \\ \Delta E_{ij} &= \left|Ed_3v_{p,ij}\right| - \left|Ed_3v_{n,ij}\right| \end{aligned} \tag{5.4}$$

where $Ed_3v_{p,ij}$ and $Ed_3v_{n,ij}$ denote the wavelet energy of positive and negative pole voltage components in cable *ij*.

The selection of K in (5.4) is a trade-off between the detection speed and accuracy. When K is too large, it will reduce the detection speed and bring a huge computation burden. When K is too small, the processing of high-frequency signals is not accurate enough, and it easily affects the protection selectivity and reliability, as well as the robustness of the protection of withstanding noise intervention is also reduced. Considering a certain tolerance level, K is set to 10.

Finally, the fault type identification criterion can be expressed as:

$$\begin{cases} \Delta E_{ij} \geq \Delta E_{set1}(\text{PTG}), \Delta E_{ij} \leq \Delta E_{set2}(\text{NTG}) \\ \Delta E_{set2} \leq \Delta E_{ij} \leq \Delta E_{set1}(\text{PTP}) \end{cases} \tag{5.5}$$

where ΔE_{set1} and ΔE_{set2} in (5.5) are the thresholds for fault type identification. Due to the symmetrical system configuration, the ΔE_{ij} presents the same magnitude and opposite polarity for PTG and NTG faults. Thus, the ΔE_{set2} is set as $-\Delta E_{set1}$ in this work.

5.3. DETERMINATION OF THRESHOLD VALUES

Threshold of Step 1

The selection of $V_{dc,Thre}$ is a trade-off between the robustness to noise interference and the sensitivity against HIF. If $V_{dc,Thre}$ is set above 0.95 p.u., the relay units could be activated by noise interference of 25 dB, which would impact the performance of subsequent steps. On the other hand, when the $V_{dc,Thre}$ is set below 0.95 p.u., the relay units may not detect an internal HIF. After numerous simulation studies, the choice of 0.95 p.u. of $V_{dc,Thre}$ guarantees that the protection can be activated correctly for internal HIFs (Considering R_f up to 500 Ω) and 25 dB noise interference.

Thresholds of Steps 2 and 3

The selection of the thresholds of step 2 must ensure successful selectivity and sensitivity of the protection. Specifically, the $d_3v_{(1)ij,Thre}$ should be greater than the maximum absolute value of $d_3v_{(1)ij}$ for the most serious external fault, and be smaller than the minimum absolute value of $d_3v_{(1)ij}$ for an internal HIF, assuming $R_f \leq 500\Omega$. The $d_3v_{(1)ij,Thre}$ must satisfy the following condition:

$$k_{sen} \min\left|d_3v_{(1)ijin}\right| > d_3v_{(1)ij,Thre} > k_{rel} \max\left|d_3v_{(1)ijex}\right| \tag{5.6}$$

where $d_3v_{(1)ijex}$ is the d_3 component when the most severe external fault occurs, which is a bolted PTP fault occurs at the outlet of a neighboring cable [106]. Since, in this case,

the $d_3v_{(1)ijin}$ measured at the faulty cable is the maximum value of external faults, the value may be even larger than some internal faults, which is very challenging for ensuring the selectivity of protection. $d_3v_{(1)ijin}$ is the d_3 component when an internal fault ($R_f = 500\,\Omega$) occurs on cable *ij*. Therefore, when (5.3) is met, it is considered that an internal fault has occurred. Otherwise, the algorithm denotes it as an external fault.

For the studied relays R_{12} and R_{21}, the most serious external fault is the metallic PTP fault occurring at the outlet of cable13 and cable24, respectively. Based on the simulations results, the largest value of $d_3v_{(1)12ex}$ under external fault f_{13} is 0.6368, $d_3v_{(1)21ex}$ under external fault f_{24} is 1.2733;

Furthermore, the smallest value of $d_3v_{(1)12in}$ and $d_3v_{(1)21in}$ under internal HIF ($R_f = 500\,\Omega$) is 1.65 and 2.17, respectively.

In this thesis, it is considered that a reliability coefficient of $k_{rel} = 1.2$ [106], and a sensitivity coefficient of $k_{sen} = 0.85$. According to (5.6), the thresholds should satisfy: $d_3v_{(1)12,Thre} \in (0.764, 1.403)$ and $d_3v_{(1)21,Thre} \in (1.527, 1.84)$. To accelerate the detection speed, finally $d_3v_{(1)12,Thre} = 0.764$ and $d_3v_{(1)21,Thre} = 1.527$. In this way, both the selectivity and sensitivity of step 2 are guaranteed. The thresholds of other relays should be selected in the same way.

The determination of the thresholds ΔE_{set1} and ΔE_{set2} mainly considers the internal HIF, as selectivity is already guaranteed by step 2. Following the threshold determination procedures for step 2, we set ΔE_{set1} and ΔE_{set2} to 23.10 and -23.10 for R_{12}, and to 93.5 and -93.5 for R_{21}, respectively.

The flow chart of the proposed protection scheme is depicted in Figure 5.3. The scheme consists of three steps. To begin with, the DC voltage $V_{dc,ij}$ is sampled to determine whether the start-up criteria are met or not. If they are satisfied, the algorithm moves to the next step that identifies the faulty area using the $d_3v_{(1)ij}$ as illustrated in (5.3). Once an internal fault is determined, the wavelet energy difference ΔE_{ij} is adopted to identify the specific fault type as explained in (5.4), and the interruption commands will provide trips to the corresponding VARC DCCB, the model of which is applied to demonstrate fault current interruption. Otherwise, the protection will be reset.

5.4. SIMULATION AND RESULTS ANALYSIS

5.4.1. PERFORMANCE UNDER INTERNAL FAULT CASES

PROTECTION START-UP

For the observed relay units R_{12} and R_{21}, fault scenarios on cable12 are internal DC faults. All test faults are applied at 1.2s on cable12 for various fault locations *l*, and the fault-impedance R_f is varied from 0.1 Ω to 500 Ω. The sampling rate of 100 kHz in PSCAD/EMTDC was chosen for the protection algorithm to capture the features of high-frequency components using wavelet transform, which is technically possible to achieve in practice. Typical commercially available high-resolution relays are SEL-T401L, SEL-T400L, and SEL-TWFL.

Figure 5.4 presents the results of the protection start-up criteria for fault f_{12}|PTP(l = 50km). The fault distance from relay R_{12} is 50 km. When the voltage TW arrives at R_{12}, voltage $V_{dc,12}$ drops less than the threshold of 0.95 p.u. within 0.3ms. Similarly, voltage $V_{dc,21}$ starts to decrease later since the fault location l for R_{21} is 150 km. It is visible that

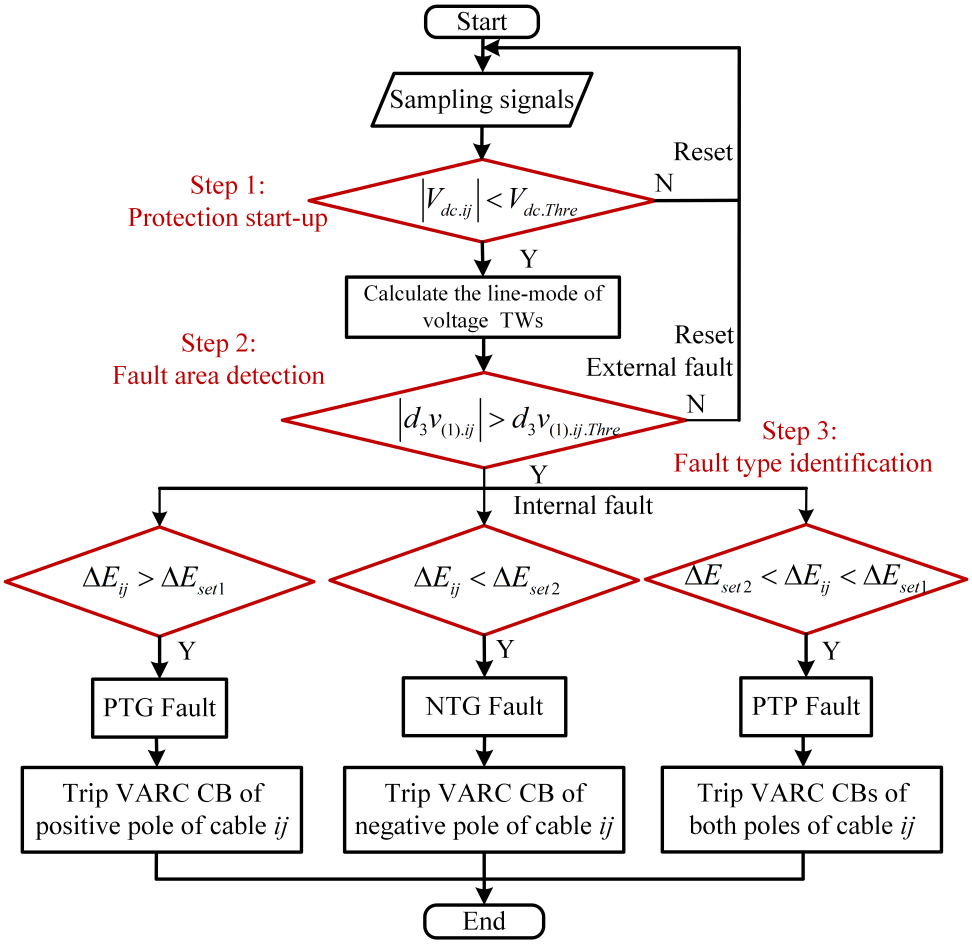

Figure 5.3: Flowchart of the overall protection scheme.

the start-up process is affected by the fault resistance, which impacts the TW propagation by changing the wave impedance alongside the faulty cable. The protection operation threshold is 0.95p.u (997.5 kV), and it can be satisfied with R_f up to 500 Ω, which confirms the desired sensitivity performance of the protection scheme to HIF.

FAULT AREA IDENTIFICATION

Figure 5.5 presents the line-mode voltage $v_{(1)12}$ and $v_{(1)21}$ and their corresponding d_3 components. According to Figure 5.5(a) and (b), the line-mode voltage TWs measured at R_{12} and R_{21} are constant values in steady-state. When the fault occurs at 1.2s, the attenuation and oscillation at the initial post-fault stage of $v_{(1)12}$ and $v_{(1)21}$ occur and are accompanied by the refraction and reflection of the line-mode voltage TW. Figure 5.5(c) and (d) demonstrate the appearance of the d_3 components. The magnitude depends on

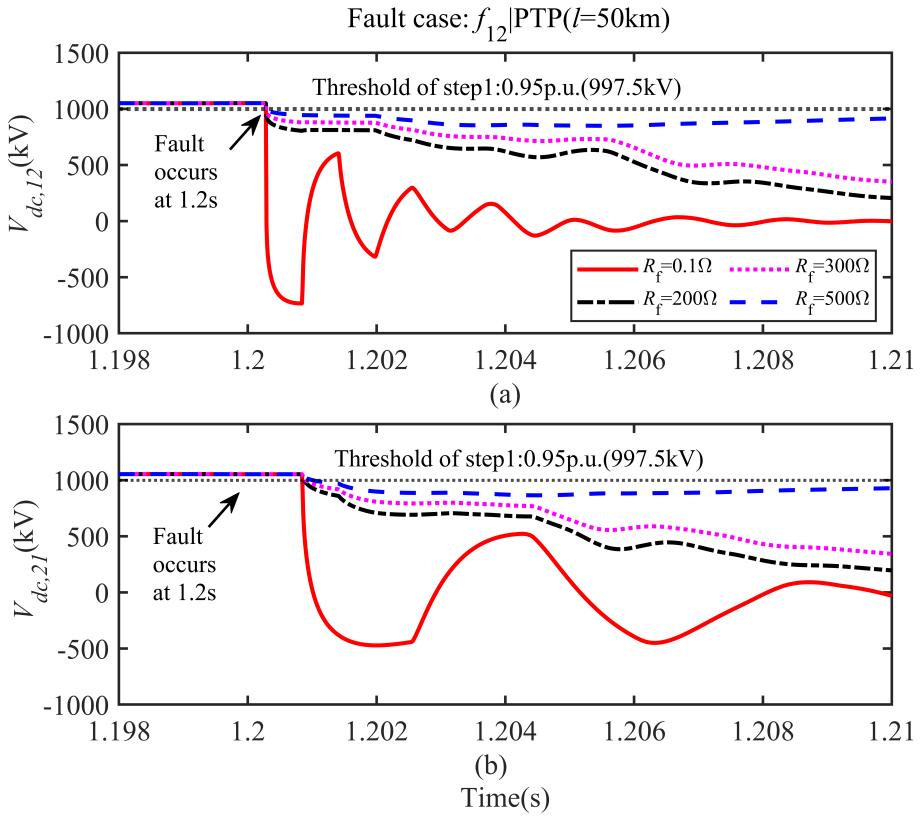

Figure 5.4: Simulation of DC voltage with f_{12}|PTP(l= 50km). (a) DC voltage $V_{dc,12}$. (b) DC voltage $V_{dc,21}$.

the specific fault location l, and the fault-resistance R_f. At steady- and post-fault states, the amplitudes of $d_3 v_{(1)12}$ and $d_3 v_{(1)21}$ are close to zero. The maximum transient values can be extracted at the instant when the line-mode TW arrives at the relay units. The protection thresholds are then satisfied and start to identify the specific fault type.

FAULT TYPE IDENTIFICATION

Figure 5.6 presents the energy difference measured at the relay units R_{12} and R_{21} for faults scenarios f_{12}|PTP(l = 50km), f_{12}|PTG(l = 50km) and f_{12}|NTG(l = 50km), respectively. The fault resistance is set at 10 Ω.

From Figure 5.6 (a) and (b), it can be seen that when the TW arrives at the cable terminals, the wavelet energy of $d_3 v_{p12}$ and $d_3 v_{n12}$ at both poles will increase instantly to a distinguishable value. Since the fault type is a PTP fault, the transient behavior of the positive and negative poles presents a symmetrical trend. The wavelet energy is nearly the same. Thus, the energy difference in accordance to (5.3) is close to zero. However, the wavelet energy can solely be located at the positive pole as proven in Figure 5.6(c)

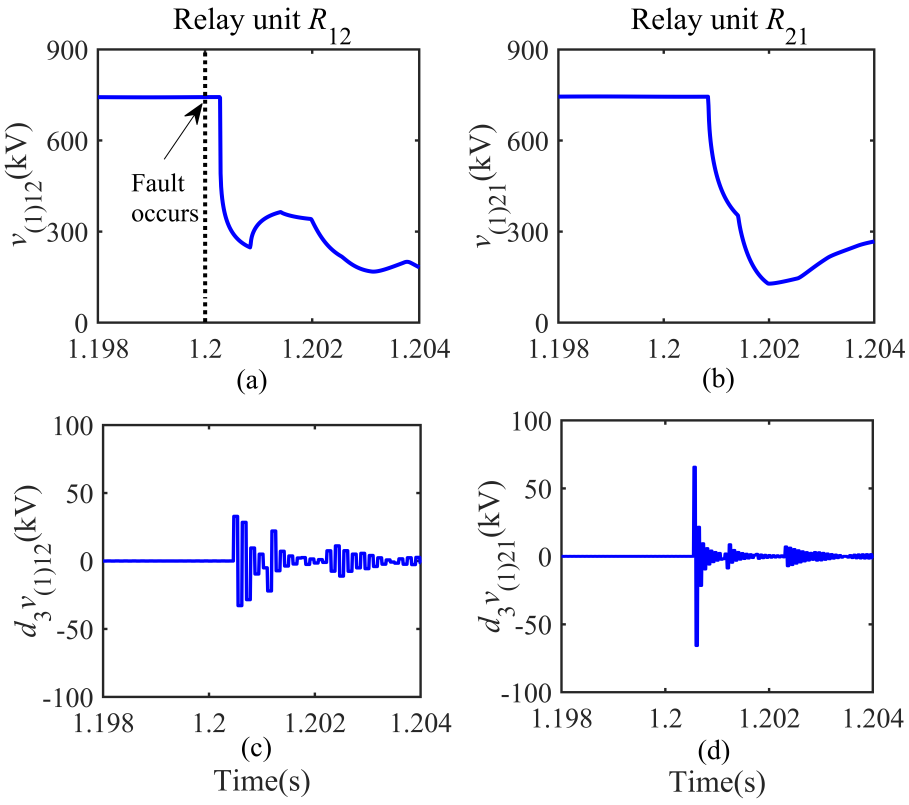

Figure 5.5: Simulation of fault scenario: f_{12}|PTP($l = 50$km, $R_f = 50\Omega$).

and (d) in the case of PTG fault, whilst the wavelet energy of the negative pole is close to zero. Similar results are also found for NTG fault as illustrated in Figure 5.6(e) and (f). By using this feature, the fault type is then determined by (5.5). The test results for more internal fault scenarios are shown in Table.5.1 through Table.5.3. All signals $d_3 v_{(1)12}$ and $d_3 v_{(1)21}$ monitored at R_{12} and R_{21} exceed the threshold value for any fault condition. By taking the energy difference ΔE_{12} and ΔE_{21} in the case of PTP fault as an example, it can be seen that the computed maximum energy difference (which in this case is 19.14) is relatively small. However, the magnitude of the energy difference in the case of a PTG or a NTG fault is much greater than that of a PTP fault. It is noted that the polarity of the energy difference for a PTG and a NTG fault is opposite due to the energy definition in (5.4); Therefore, the PTG and the NTG fault is discriminated. It can be concluded that all faulty areas can be detected, and all fault types can be identified. The relay units R_{12} and R_{21} operate correctly by sending tripping signals to the corresponding VARC DCCBs within 2ms.

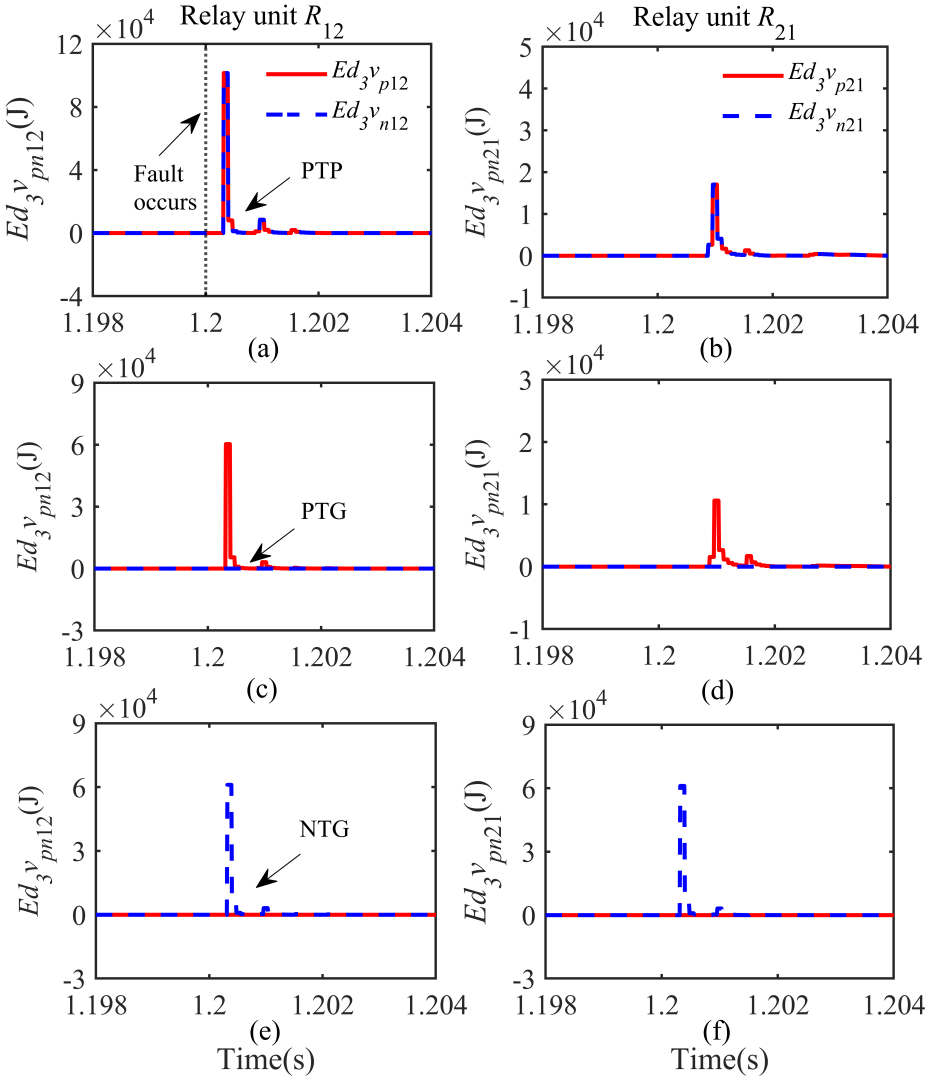

Figure 5.6: Simulation of wavelet energy of positive and negative poles.

5.4.2. PERFORMANCE UNDER EXTERNAL FAULT

Several external fault scenarios are carried out on external zones of cable12. Detailed results are summarized in Table. 5.4. Regarding these external faults, the magnitudes of $d_3v_{(1)12}$ and $d_3v_{(1)21}$ for any external fault are lower than the thresholds. The maximum magnitudes of $d_3v_{(1)12}$ and $d_3v_{(1)21}$ are 0.6368 and 1.2733, respectively. However, compared to the results of the internal DC faults listed in Table.5.1 to Table. 5.3, the magnitudes of $d_3v_{(1)12}$ and $d_3v_{(1)21}$ are relatively small. The protection will be then reset.

Table 5.1: Test Results Under Fault: f_{12}|PTP($l = 50$km)

Fault Case	Relay Unit R_{12}			Relay Unit R_{21}		
R_f (Ω)	$d_3 v_{(1)12}$ (kV)	ΔE_{12} (kV)	Trip (ms)	$d_3 v_{(1)21}$ (kV)	ΔE_{21} (kV)	Trip (ms)
0	376.44	19.14	PN/0.30	200.57	9.11	PN/0.86
10	267.44	9.87	PN/0.60	142.44	0.13	PN/0.88
50	32.79	0.40	PN/0.48	65.61	0.07	PN/0.87
100	19.59	0.23	PN/0.48	39.18	0.04	PN/0.88
200	10.83	0.13	PN/0.48	21.70	0.02	PN/0.89
300	7.49	0.087	PN/0.48	15.0	0.023	PN/0.92
500	4.63	9.052	PN/0.48	9.27	0.007	PN/1.03

Table 5.2: Test Results Under Fault: f_{12}|PTG($l = 100$km)

Fault Case	Relay Unit R_{12}			Relay Unit R_{21}		
R_f (Ω)	$d_3 v_{(1)12}$ (kV)	ΔE_{12} (kV)	Trip (ms)	$d_3 v_{(1)21}$ (kV)	ΔE_{21} (kV)	Trip (ms)
0	101.33	2.77e5	P/0.58	117.33	2.77e5	P/0.58
10	56.53	8.78e4	P/0.58	66.23	8.78e4	P/0.58
50	20.28	1.15e4	P/0.58	23.93	1.15e4	P/0.58
100	11.26	3.54e3	P/0.58	13.31	3.54e3	P/0.58
200	5.96	990.52	P/0.59	7.05	990.4	P/0.59
300	4.05	460.03	P/0.59	4.79	450.94	P/0.59
500	2.47	170.12	P/0.64	2.93	170.07	P/0.65

Table 5.3: Test Results Under Fault: f_{12}|NTG($l = 150$km)

Fault Case	Relay Unit R_{12}			Relay Unit R_{21}		
R_f (Ω)	$d_3 v_{(1)12}$ (kV)	ΔE_{12} (kV)	Trip (ms)	$d_3 v_{(1)21}$ (kV)	ΔE_{21} (kV)	Trip (ms)
0	110.64	-31.e8	N/0.86	39.46	-200.6e3	N/0.30
10	62.4	-10.76e3	N/0.87	23.17	-61.1e3	N/0.30
50	22.59	-1.5e3	N/0.87	8.66	-7.73e3	N/0.32
100	12.57	-0.47e3	N/0.98	4.86	-2.37e3	N/0.30
200	6.67	-0.13e3	N/1.45	2.59	-660.25	N/0.44
300	4.54	-60.14	N/1.45	1.76	-300.59	N/0.46
500	2.77	-30.32	N/1.45	1.57	-110.36	N/0.62

Table 5.4: Results of The Protection Against External Faults

External Faults (l(km),$R_f(\Omega)$)	$\lvert d_3 v_{(1)12}\rvert$ (kV)	$\lvert d_3 v_{(1)21}\rvert$ (kV)	Step2 Met?
f_1|(DC bus1 fault)	0.3918	0.3149	×
f_2|(DC bus2 fault)	0.5049	0.5520	×
f_3|(DC bus4 fault)	0.0251	0.0866	×
f_4|(AC gird1 fault)	0.0453	0.0391	×
f_5|(AC grid2 fault)	0.0634	0.0526	×
f_{13}|PTG($l=0, R_f=0$)	0.3291	0.3292	×
f_{13}|PTP($l=0, R_f=0$)	0.6368	0.4175	×
f_{24}|PTP($l=0, R_f=0$)	0.3636	1.2733	×
f_{13}|PTP($l=0, R_f=10$)	0.5679	1.1365	×
f_{13}|PTP($l=0, R_f=50$)	0.3774	0.7580	×
f_{13}|PTG($l=100, R_f=0$)	0.0884	0.1190	×
f_{24}|PTG($l=100, R_f=0$)	0.1728	0.1233	×
f_{34}|PTP($l=100, R_f=0$)	0.0180	0.0342	×
f_{34}|PTG($l=100, R_f=0$)	0.0060	0.0165	×

5.4.3. TRIPPING TIME DELAY EVALUATION

The tripping time t_{trip} of the proposed protection in Figure 5.3 is comprehensively determined, and computed as follows:

$$t_{trip} = \frac{l}{v_{(1)}} + t_{step1} + 50\mu s + t_{step2} + 50\mu s + t_{step3}. \tag{5.7}$$

In (5.7), 50 μs is the sensor's time delay between each step. $l/v_{(1)}$ represents the TWs propagation delay. Based on the given values, the calculation of $l/v_{(1)}$ yields a result that: $l/v_{(1)} \leq 1.107$ ms. This calculation is based on a maximum possible fault distance of $l = 200$ km for cable 12, and the velocity for $v_{(1)} = 1.806 \times 10^5$ km/s.

The value of t_{step1} in (5.2) is influenced by the R_f and the fault type. When an NTG or PTG fault occurs with a fault resistance of $R_f = 500\,\Omega$, it is observed that $t_{step1} \leq 0.52$ ms. In general, a higher value of R_f results in a larger value of t_{step1}. t_{step2} is mainly determined by the time delay caused by the use of DWT, which is dependent on three factors: the required decomposition level (3rd-level), the sampling frequency (100kHz), and the mother wavelet ('Haar'). In the present work, the resulting time delay is 0.05 ms, which is visible and demonstrated in Figure 5.2.

Once the criterion (5.2) is satisfied, the measured $d_3 v_{(1)ij}$ will exceed the corresponding thresholds after a few sampling intervals (10μs for one sample). t_{step3} is determined by the time delay of DWT, and the computational delay of the energy calculator in (5.4). Recall $K = 10$ in (5.4), the time interval for calculating one data ΔE_{ij} in (5.4) is $10 \times 10\mu s =$ 0.1 ms. The measured ΔE_{ij} meets (5.5) within a few time intervals.

Taking the relay unit R_{12} as an example, the longest tripping time t_{trip} for the fault f_{12}|PTG($l = 200$ km, $R_f = 500\,\Omega$) is 1.747 ms. Consequently, the proposed protection

meets the requirements of fault detection speed for practical HVDC applications.

5.4.4. INTERACTION BETWEEN PROTECTION AND VARC DCCBS FOR FAULT CURRENT INTERRUPTION

Figure 5.7 presents a successful fault current interruption by the VARC DCCB based on protection operation for a fault scenario: f_{12}|PTP(l = 100km, R_f = 0Ω).

The I_{osc}, I_{line}, and I_{mov} refer to the oscillating current, cable current, and current in the branch [78], respectively.

In this fault scenario, the VARC DCCB is activated at 1.2088s. For the VARC DCCB in R_{12}, it is observed that it starts generating oscillating current I_{osc} at 3.92ms after the fault occurrence. The peak fault currents are 4.73 kA and -4.73 kA at 1.2041s. Then, the fault currents are interrupted by the main vacuum interrupter at 1.2081s. The peak fault currents in the VARC DCCB are 5.94 kA and -5.94 kA, respectively. The fault currents are interrupted at 1.2088s. The VARC DCCBs installed in other cables are not activated.

Figure 5.7 reveals that the proposed protection scheme and the DCCBs have good interaction performance. The observed faulty area and fault type are discriminated correctly, and the corresponding faulty poles of cable12 can be interrupted promptly.

5.4.5. INFLUENCE OF NOISE ON PROTECTION PERFORMANCE

Protective relays, in practice, encounter noise disturbances from various sources, such as electromagnetic interference, communication noise, and harmonics. These noises can obscure the measured signals, which may result in protection malfunctions.

The common type of noise, Gaussian White Noise (GWN), is added to the measured signals. The GWN is a random signal with a constant power spectral density. The GWN can simulate a wide array of potential system interferences, making it essential to validate the robustness of the protection scheme against it.

The GWN is added to the sampled TW signals with different signal-noise-ratio (SNR) levels: 25 dB and 40 dB. Two independent fault cases are performed in the studied system, and the test results at the relay unit R_{12} are presented in Table. 5.5.

Step 1 of the protection is minimally affected by the noise, and the relay units can be activated correctly with noise interference. Since the white noises can be regarded as high-frequency harmonics to line-mode voltage, the magnitude of $d_3 v_{(1)12}$ and ΔE_{12} are affected proportionally to the level of the noise intervention as shown in Table. 5.5. However, the maximum absolute values of $d_3 v_{(1)12}$, and energy difference ΔE_{12} exceed the selected thresholds for the faulty area and the fault type identification. Therefore, the results confirm that the proposed protection scheme is sufficiently robust to withstand the 25 dB noise intervention.

5.5. COMPARISON WITH OTHER PROTECTION METHODS

5.5.1. COMPARISON WITH DC INDUCTOR VOLTAGE CHANGED RATE BASED METHOD

The change rate of the DC inductor voltage can provide fast and accurate detection of a DC fault in an HVDC system. In a steady state, the DC inductor voltage is theoretically zero. After the DC fault occurrence, the voltage will surge as the DC current increases

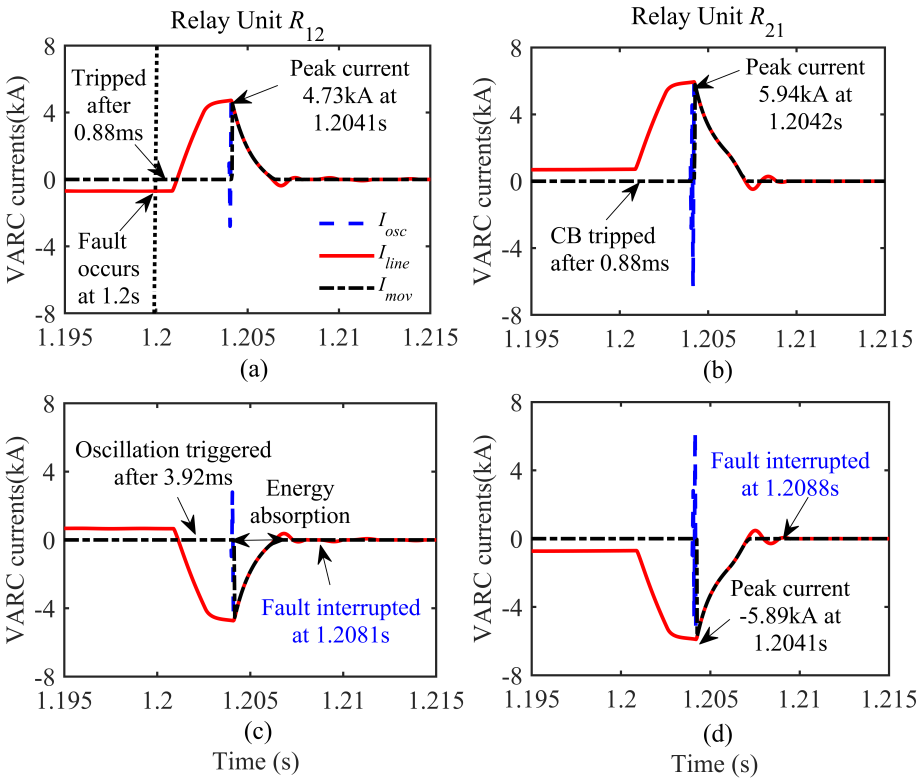

Figure 5.7: Simulation of VARC DCCB Currents. (a).Positive pole at R_{12}. (b).Positive pole at R_{21}. (c).Negative pole at R_{12}. (d). Negative pole at R_{21}.

Table 5.5: Noise Test Results with a Different Noise Level and a Fault Resistance $R_f(\Omega)$

f_{12}|PTG (l = 100km)	SNR=25 dB			SNR=40 dB		
	0 Ω	100 Ω	200 Ω	0 Ω	100 Ω	200 Ω
max$\|d_3 v_{(1)12}\|$	72.46	29.17	35.20	92.55	6.84	8.45
ΔE_{12}	1.4e5	2.2e3	2.9e3	1.3e5	1.7e3	1.67e3
Tripping	√P	√P	√P	√P	√P	√P
f_{12}|NTG (l = 150km)	SNR=25 dB			SNR=40 dB		
	0 Ω	100 Ω	200 Ω	0 Ω	100 Ω	200 Ω
max$\|d_3 v_{(1)12}\|$	30.13	23.44	26.16	40.12	5.42	6.16
ΔE_{12}	-2.8e4	-2.3e3	-3.2e3	-3.3e4	-428.1	-120.2
Tripping	√N	√N	√N	√N	√N	√N

rapidly. A DC inductor voltage change rate-based protection scheme is proposed in [23]. A short time interval Δt for the voltage across the terminal reactor to rise from an initial threshold V_{LTt1} to the protection threshold V_{LTt2} is used to depict the derivative of the DC reactor voltage, which can be expressed as follows [23]:

$$\frac{V_{LTt2} - V_{LTt1}}{\Delta t} = \frac{\Delta V_{Lt}}{\Delta t} = \frac{d v_{Lt}}{dt} = L_{dc} \frac{d^2 i_{DC}}{dt^2}, \tag{5.8}$$

With predefined thresholds V_{LTt1} and V_{LTt2}, the derivative of the DC reactor voltage is determined by the time interval Δt. By monitoring the Δt, the change rate of the DC inductor voltage is used for fault detection. The voltage across the L_{dc} is measured continuously, and only a fault detection that lasts longer than a minimum fault detection time is valid.

For comparison purposes, the fault location indication time is set to 180 μs, and the predefined thresholds of V_{LTt1} and V_{LTt2} are set as 5 kV and 10 kV, which are in line with the values in [23]. If the threshold V_{LTt1} and V_{LTt2} are met and the time interval Δt is less than the threshold value of 180 μs, it is an indication that the fault has occurred. If Δt is longer than 180 μs, then the cable is a healthy cable, and no protection action is activated.

Three independent faults are simulated to verify algorithm effectiveness. The simulation of the inductor voltages V_{Lp12} and V_{Ln12} at cable12 terminal are shown in Figure 5.8.

The voltages across the inductors increase rapidly after the fault occurrence. Following the fault f_{12}|PTG(l = 10km), the protection method in [23] operates correctly. However, it is seen that the inductor voltages also surge during the external fault f_{13}|PTP(l = 10km, $R_f = 0\Omega$) and the bus fault f_1; Furthermore, they experience similar trends at the fault initial stage with the fault f_{12}|PTG(l = 10km, $R_f = 0\Omega$). The thresholds of 5 kV and 10 kV are promptly exceeded. The protection will malfunction and trip both DCCBs at R_{12}, resulting in taking out of service of the healthy cable. In contrast, the proposed algorithm will correctly identify internal and external faults for cable12 as validated in previous subsections. Thus, the protection method in [23] presents low selectivity. In addition, the procedures of threshold selection in [23] are complicated to be applied in other systems or industrial projects. The time window Δt between two thresholds (inductor voltage increase from 5 kV to 10 kV) requires precise signal measuring, which makes the protection vulnerable to noise effects.

5.5.2. COMPARISON WITH MEDIAN ABSOLUTE DEVIATION BASED TRANSIENT SIGNAL DETECTION

A Median Absolute Deviation (MAD)-based TWP is proposed in [36], which realizes the fault detection by locating the outliers in the sampling dataset of voltage and current TWs.

A faulty pole is detected when the criteria $W_{MAD}(t) \geq \Delta_1$ and $W_{MAD\_M}(t) \leq \Delta_2$ are satisfied. Here $W_{MAD}(t)$ and $W_{MAD\_M}(t)$ refer to the results processed by MAD, and the modified MAD algorithm MAD_M from the sampling current and voltage TWs, respectively.

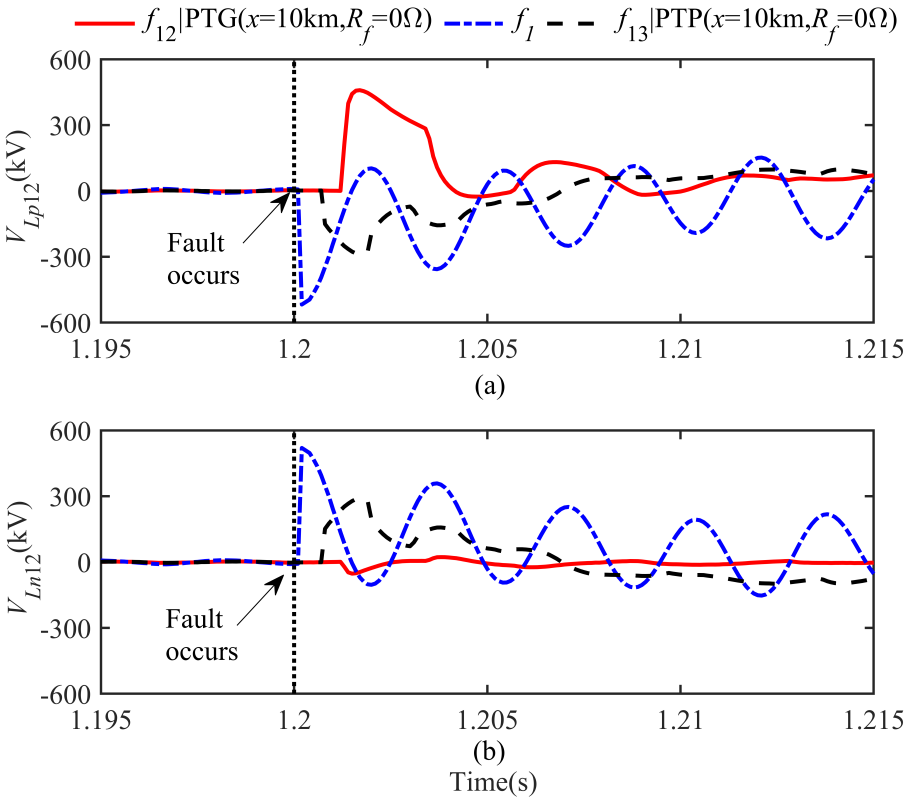

Figure 5.8: DC inductor voltages. (a). V_{Lp12} at positive pole. (b). V_{Ln12} at negative pole

The thresholds Δ_1 and Δ_2 in the studied testing system are set to 6.0 p.u. and -0.2 p.u., respectively. The latest 50 samples are considered, which aligns with the procedure applied in [36]. Two fault cases in [36] are also investigated for the studied system:

- F1: PTP fault on cable12 50 km from bus1.
- F2: PTP fault on cable12 100 km from bus1.

The data calculated at relay units R_{12} and R_{21} of cable12 are summarized in Table. 5.6. The magnitudes of MAD.I and MAD.V are inversely proportional to the fault impedance. The results for the positive and negative poles are very close due to the symmetrical fault and system configuration. When the fault-impedance exceeds 50 Ω, the damping of the voltage and current TWs is not obvious, and the criterion in [36] is not satisfied. Thus, the MAD algorithm fails to extract the outliers from the sampling dataset (marked as red). This confirms the limit of the sensitivity of MAD-based TW protection, whilst the proposed protection scheme is capable of detecting high-impedance (up to 500Ω) correctly. Furthermore, the MAD-based protection is not robust enough to with-

Table 5.6: MAD Based TWP Performance With Different R_f(Ω)

F1	Item (p.u.)	10Ω	50Ω	100Ω	200Ω
MAD	I_{dc12^+}	8.276	4.351	2.574	1.619
	I_{dc12^-}	9.320	5.793	2.644	1.509
	I_{dc21^+}	9.081	5.785	4.277	3.157
	I_{dc21^-}	9.023	5.704	4.177	3.050
MAD_M	V_{dc12^+}	-0.501	-0.272	-0.171	-0.098
	V_{dc12^-}	-0.50	-0.272	-0.171	-0.098
	V_{dc21^+}	-0.422	-0.198	-0.122	-0.069
	V_{dc21^-}	-0.422	-0.197	-0.123	-0.068
F1 Trip	R_{12}&R_{21}	√PN	×	×	×
F2	Item (p.u.)	10Ω	50Ω	100Ω	200Ω
MAD	I_{dc12^+}	8.828	4.118	2.077	1.612
	I_{dc12^-}	8.875	4.180	2.151	1.498
	I_{dc21^+}	11.278	6.812	4.895	3.493
	I_{dc21^-}	11.249	6.736	4.803	3.389
MAD_M	V_{dc12^+}	-0.478	-0.249	-0.155	-0.086
	V_{dc12^-}	-0.479	-0.249	-0.156	-0.087
	V_{dc21^+}	-0.478	-0.249	-0.154	-0.085
	V_{dc21^-}	-0.478	-0.249	-0.154	-0.085
F2 Trip	R_{12}&R_{21}	√PN	×	×	×

stand the noise intervention as it will regard the noises as outliers, whilst the proposed method is demonstrated to operate correctly with a 25 dB noise intervention.

5.5.3. COMPARISON WITH COMMERCIALLY AVAILABLE METHODS

The traveling wave protection (TWP) in [106] uses voltage/current and their derivatives to detect the faults, which can be expressed as,

$$\begin{cases} \dfrac{dv}{dt} > \Delta set_1 \\ \Delta v > \Delta set_2 \end{cases}, \quad \begin{cases} \dfrac{di}{dt} > \Delta set_3 \text{ (Rectifier side)} \\ \Delta i > \Delta set_4 \text{ (Inverter side)} \end{cases} \tag{5.9}$$

where Δset_i (i=1, 2, 3, 4) are thresholds for fault detection.

The TWP in [22] adopts pole-mode wave P_{wave} and ground-mode G_{wave} and their derivatives for fault detection, which can be represented by:

$$\begin{cases} \dfrac{dP_{wave}}{dt} > \Delta set_1 \\ \Delta P_{wave} > \Delta set_2 \end{cases}, \quad \begin{cases} \dfrac{dG_{wave}}{dt} > \Delta set_3 \\ \Delta G_{wave} > \Delta set_4 \end{cases} \tag{5.10}$$

Following the threshold setting procedures in [22], [106], the thresholds Δset_i (i=1, 2, 3, 4) of TWP in [106] in the studied testing system are set as 690.94 kV/ms, 757.34 kV,

1.33 kA/ms, and 3.37 kA, respectively. For the TWP criteria in [22], the thresholds are set as 776.02 kV/ms, 898.65 kV, 836.84 kV, and 707.32 kV, respectively. In addition to F1 and F2, the TWP methods in [22], [106] are tested by more fault cases:

- F3: PTG fault 0 km from bus1 (R_f=200 Ω)
- F4: PTG fault 50 km from bus1 (R_f=200 Ω)
- F5: NTG fault 50 km from bus1 (R_f=200 Ω)
- F6: Metallic PTP fault. 0 km at cable13.

It is noted that F1 and F2 are metallic faults. Test results for R_{12} are listed in Table. 5.7, both TWP methods in [22], [106] could operate correctly under metallic faults F1 and F2. However, the TWP methods in [22], [106] fail to trip the DCCBs due to a limited voltage drop and limited current increase during HIF. Thus, low sensitivity problems are visible in [22], [106] in the case of HIF. The limitations of the TWP methods in [22], [106] are not visible in the proposed protection, as demonstrated previously.

Table 5.7: The Performance of TWP Methods In [22], [106]

Relay R_{12}	F1	F2	F3	F4	F5	F6
$\frac{dv_{p12}}{dt}$(kV/ms)	54012.1	22015.5	5512.3	3066.8	2.21	573.09
Δv_{p12}(kV)	893.69	818.52	114.12	1.373	1.312	630.30
$\frac{dv_{n12}}{dt}$(kV/ms)	54011.9	22015.5	1.963	113.72	3084.5	575.79
Δv_{n12}(kV)	890.38	815.36	3.865	3.399	111.94	631.12
$\frac{di_{p12}}{dt}$(kA/ms)	3.67	3.154	0.351	0.368	0.042	1.102
Δi_{p12}(kA)	4.79	4.42	0.805	0.726	0.058	2.793
$\frac{di_{n12}}{dt}$(kA/ms)	3.669	3.149	1.963	0.039	0.365	1.109
Δi_{n12}(kA)	4.776	4.409	0.051	0.042	0.714	2.805
Trips	√ PN	√ PN	×	×	×	×
Relay R_{12}	F1	F2	F3	F4	F5	F6
$\frac{dP_{p12}}{dt}$(kV/ms)	54145.1	22056.4	5520.7	3074.9	2.715	517.76
ΔP_{p12}(kV)	1008.4	1010.04	160.99	155.8	1.693	437.71
$\frac{dP_{n12}}{dt}$(kV/ms)	53878.9	21974.9	6.213	3.335	5823.89	646.69
ΔP_{n12}(kV)	817.74	712.16	4.510	3.541	121.93	748.88
$\frac{dG_{12}}{dt}$(kV/ms)	590.61	507.16	2766.1	1545.2	1530.6	697.37
ΔG_{12}(kV)	768.22	708.84	125.10	117.60	24.146	589.44
Trips	√ PN	√ PN	×	×	×	×

5.5.4. COMPARISON WITH ROCOV BASED METHOD

The protection in [19] uses the measured ROCOV at the line side of the DC inductor to detect and locate the faults. The fault is detected when the following criterion is met:

$$\text{ROCOV}_{pn.ij} = \frac{dv_{pn.ij}}{dt} > \Delta_{pn.ij} \tag{5.11}$$

where $\Delta_{pn.ij}$ is the thresholds of the ROCOV-based protection at relay R_{ij}. $v_{pn.ij}$ is the pole voltages.

Taking relay units R_{12} and R_{21} as examples, the observed ROCOV at the line side of the DC inductor for different predefined faults are summarized in the following Table. 5.8.

Table 5.8: Performance Of ROCOV Based-Method [19]

Faults	ROCOV (kV/ms) (Normal)		ROCOV (kV/ms) (SNR=25 dB)		ROCOV (kV/ms) (SNR=40 dB)	
	R_{12}	R_{21}	R_{12}	R_{21}	R_{12}	R_{21}
F1	1.08e3	0.21e3	1.10e3	0.24e3	1.07e3	0.22e3
F2	0.44e3	0.44e3	0.47e3	0.42e3	0.44e3	0.44e3
F3	0.055e3	0.0063e3	0.23e3	0.26e3	0.046e3	0.045e3
F4	0.031e3	0.0061e3	0.27e3	0.25e3	0.044e3	0.044e3
F5	0.031e3	0.0062e3	0.27e3	0.27e3	0.039e3	0.043e3
F6	0.0015e3	0.0014e3	0.18e3	0.18e3	0.029e3	0.036e3

It is obvious that the magnitude of the measured ROCOV for an external fault F6 is even higher than that of internal faults on cable12 when noise interference is present. These results imply that the reliability and selectivity performance of the ROCOV based-protection in [19] are vulnerable to noise disturbance. As such, the threshold determination is very challenging using the simple protection criterion in (5.11). The selectivity is also a problem when the fault is close to the line terminal with a small value of L_{dc}. Furthermore, [35] has demonstrated that the ROCOV method in [19] is inadequate for identifying HIF faults based solely on the ROCOV criterion as a primary protection criterion. In addition, the ROCOV method in [19] cannot distinguish specific DC fault types. The limitations of the TWP methods in [19] are not visible in the proposed protection, as demonstrated previously.

5.6. CONCLUSION

This chapter introduces the proposed DWT-based protection scheme and corresponding results. The performance of the protection is investigated by various faults and compared to existing protection methods.

The high-frequency components contained in the line mode and pole voltages TWs are used for designing the protection scheme. The DWT is the applied signal processing tool. The 'haar' wavelet is selected as the mother wavelet since it is a simple piecewise constant wavelet with good edge detection properties. The sampling frequency is set to 100 kHz. The 3^{rd} scale detailed coefficients are used for fault detection. The developed protection scheme comprises three steps: 1) The protection is activated when the measured DC voltage drops below 0.95p.u., 2) The faulty area detection is identified using the d_3 components of the line-mode voltage TWs, and 3) The specific fault type is identified by the comparison of the wavelet energy of d_3 components of the pole voltages. The setting principle of the protection threshold values for the studied and other systems is also elaborated. Finally, the robustness of the proposed protection algorithm is validated for a four-terminal MTDC system in the PSCAD/EMTDC environment.

The interaction between the proposed protection and the VARC DCCBs for fault current interruption is also demonstrated. Due to the prompt fault clearance, the MMCs and the AC grids are minimally affected by the faults. The protection is also thoroughly compared to the existing methods, including the DC reactor voltage change rate-based protection, ROCOV-based protection, and MAD-based protection, and two commercial solutions proposed in [22], [106]. The presented results confirm selectivity and sensitivity superiority of the proposed protection.

Based on the simulation results, the robustness of the proposed protection algorithm for testing MTDC grids is determined according to four aspects:

1. Speed: The fast detection and tripping (within 2 ms) of the proposed protection method meets the practical expectations;

2. Selectivity: The protection correctly operates on all internal faults and does not operate on external faults such as AC-, DC bus-, and neighboring line faults;

3. Sensitivity: The protection successfully discriminates different fault types and detects faults with a resistance of up to 500 Ω;

4. Reliability: The protection operates correctly for external faults and noise interference (25 dB).

Compared with the existing protections, the novelty and the main contributions are threefold. Firstly, the proposed protection scheme utilizes the characteristic of the transient high-frequency components contained in the fault-induced line mode and the pole voltage TWs, identifying the DC fault area and discriminating the specific fault type in an MTDC system. Secondly, the proposed protection scheme improves sensitivity in detecting HIF and promptly trips the DCCB. Thirdly, the thresholds can be easily determined and, in this way, can be easily implemented for other test models and actual grids.

6

DESIGNING THE PARAMETER FITTING-BASED FAULT LOCATION METHOD USING THE AMLM-ALGORITHM

This chapter introduces the proposed parameter fitting-based fault location method for MTDC systems and validates its performance on PSCAD and RTDS. Firstly, in this chapter, the expressions are derived for the backward line-mode current TWs containing fault location information. Then, the adaptive multi-step Levenberg-Marquardt (AMLM) algorithm is detailed for solving the nonlinear least-squares problem of parameter fitting. By doing so, the fault location can be estimated based on the fitted coefficient from the sampled discrete data. Furthermore, this chapter verifies the proposed fault location method using different MTDC systems modeled in PSCAD and RTDS through numerous simulations. The results indicate that the proposed fault location method has accurate estimation performance. The chapter ends up with the main concluding remarks.

Chapter V deals with the line protection algorithm, which identifies the faulty cables and the faulty type/poles within the MTDC system. This Chapter aims to develop a novel DC fault location method that could accurately estimate the fault location along the faulty cable. The proposed method eliminates the need to search for the fault location over hundreds of kilometers of submarine cables, minimizing repair time and accelerating the system recovery in the post-fault stage.

This chapter is organized as follows. Section 6.1 outlines the testing system setup in PSCAD/EMTDC. Section 6.2 presents the theoretical analysis of the backward line-mode current traveling waves after a DC fault. Section 6.3 describes the proposed fault location method using AMLM-based parameter fitting. Section 6.4 validates the performance of the fault location in the PSCAD environment. Section 6.5 provides the RTDS simulation conditions and the test results. Finally, conclusions are elaborated in Section 6.6.

6.1. TESTING SYSTEM FOR FAULT LOCATION

The four-terminal MMC-HVDC system, shown in Figure 6.1, is modeled in the PSCAD environment using the Cigre benchmarked testing model DCS2 (B4.57 working group). The DC voltage level has been modified to ±320 kV according to Cigre brochure. The AC grids, $G_1 - G_4$, operate at a nominal frequency of 50 Hz. M, N, P, and Q denote the DC buses. The DC inductor L_{dc} is installed at the end of each cable to limit the rising rate and peak value of the fault current.

In Figure 6.1, four MMC converters are connected by frequency-dependent (phase) cables ($l_{12} - l_{34}$) with a distance of 200 km. For the studied MMC model, the rated capacity is 1500 MVA. The number of SMs, N in each arm is 200. The arm resistance R_{arm} is 0 Ω, the arm inductance L_{arm} is 5 mH, the SM capacitance C_{sm} is 15000 μF, and the on-state resistance R_{on} is 1.361 mΩ.

At each end of the DC cable, two relay units R_{ij} and R_{ji} are installed on the positive and negative poles. The VARC DCCBs are implemented at each cable terminal, following the approach presented in [78].

6.2. FAULT ANALYSIS OF LINE-MODE CURRENT TWS

Similar to the fault analysis performed in Chapter IV, cable l_{34} is selected in Figure 6.1 as the faulty cable in this Chapter. By doing so, the relay units R_{34} and R_{43} as the observed relays. Figure 6.2.(a) describes the diagram of an internal DC fault f_{34} in the line-mode network. Figure 6.2.(b) presents the line-mode fault component *Peterson* equivalent circuit[66].

For the adopted MMC model in Figure 6.1, we have R_{eq} = 0.907 mΩ, C_{eq} = 0.45 × 10^3 μF, and L_{eq} = 3.33 mH. To simplify the subsequent analysis, the Z_{MMC} can be simplified as $1/(sC_{eq})$ and sL_{eq}, as the impact of R_{eq} is negligible.

According to Figure 6.2.(b), we can obtain the S-domain expression for line-mode

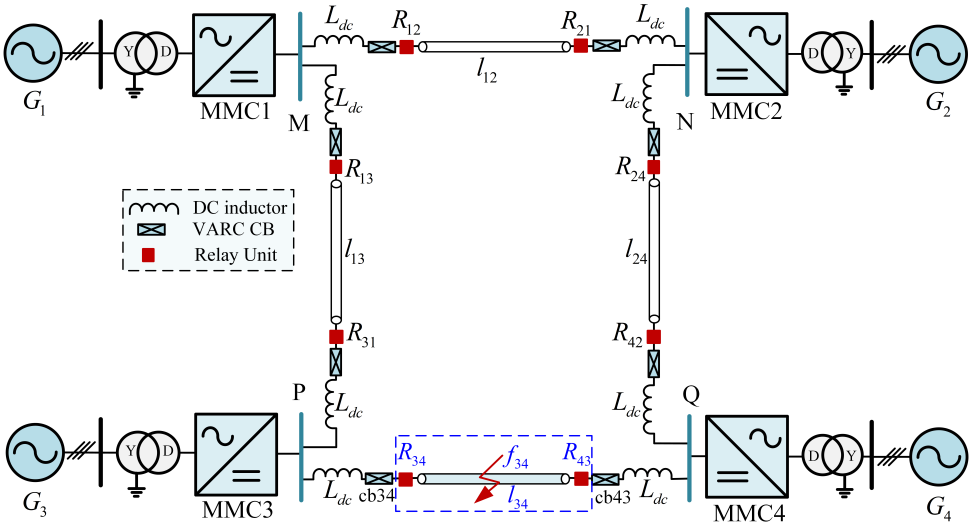

Figure 6.1: Structure of the studied four-terminal MMC-HVDC system.

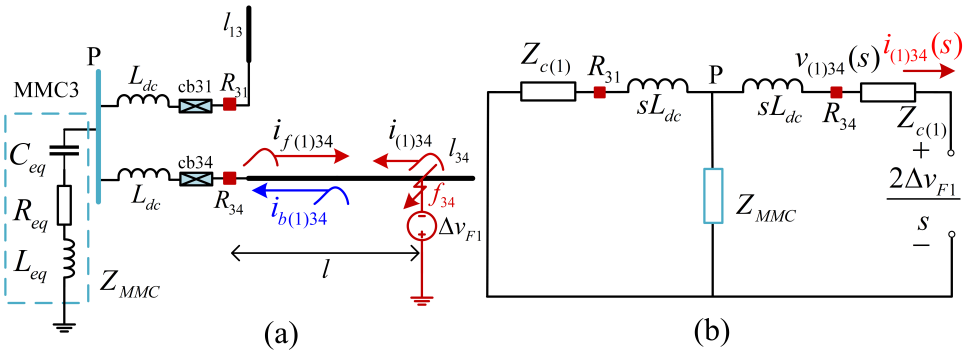

Figure 6.2: (a) fault f_{34} in the line-mode network. (b) line-mode fault component *Peterson* equivalent circuit.

fault current $i_{(1)34}(s)$ and voltage $v_{(1)34}(s)$ as follows:

$$\begin{cases} i_{(1)34}(s) = \dfrac{2\Delta v_{F1}}{s}\dfrac{1}{Z_{c(1)}+sL_{dc}+Z_P} = \dfrac{2\Delta v_{F1}}{s}\dfrac{(s-z_1)(s-z_2)}{(Z_{c(1)}+sL_{dc})(s-p_1)(s-p_2)}, \\ v_{(1)34}(s) = \dfrac{2\Delta v_{F1}}{s}\left(1-\dfrac{Z_{c(1)}}{Z_{c(1)}+sL_{dc}+Z_P}\right) = \dfrac{2\Delta v_{F1}}{s}\left(1-\dfrac{Z_{c(1)}(s-z_1)(s-z_2)}{(Z_{c(1)}+sL_{dc})(s-p_1)(s-p_2)}\right). \end{cases} \tag{6.1}$$

where the Δv_{F1} is the same as that used in Chapter 4 and shown in Table. 4.3. z_1, z_2, p_1,

p_2, and Z_P in (6.1) are calculated as follows:

$$\begin{cases} z_{1,2} = \dfrac{-Z_{c(1)}C_{eq} \pm \sqrt{(Z_{c(1)}C_{eq})^2 - 4C_{eq}(L_{dc}+L_{eq})}}{2C_{eq}(L_{dc}+L_{eq})}, \\ p_{1,2} = \dfrac{-Z_{c(1)}C_{eq} \pm \sqrt{(Z_{c(1)}C_{eq})^2 - 8C_{eq}(L_{dc}+2L_{eq})}}{2C_{eq}(L_{dc}+2L_{eq})}, \\ Z_P = \dfrac{(Z_{c(1)}+sL_{dc})(\frac{1}{sC_{eq}}+sL_{eq})}{Z_{c(1)}+sL_{dc}+\frac{1}{sC_{eq}}+sL_{eq}}. \end{cases} \tag{6.2}$$

The L_{dc} in the system in Figure 6.1 is set to 40 mH, and the line-mode characteristic impedance in the adopted cable model is $Z_{c(1)} = 19.0\ \Omega$. As such, we have the following relationship: $Z_{c(1)}^2 C_{eq}^2 = 73.10\times10^6 \gg 8C_{eq}(2L_{eq}+L_{dc}) = 167.97\times10^3 > 4C_{eq}(L_{dc}+L_{eq}) = 77.99\times10^3$.

Accordingly, the roots in (6.2) can be simplified as: $z_1 = p_1 \approx 0$, $z_2 \approx -Z_{c(1)}/(L_{dc}+L_{eq})$, $p_2 \approx -Z_{c(1)}/(L_{dc}+2L_{eq})$.

Thereby, we can rewrite (6.1) as:

$$\begin{cases} i_{(1)34}(s) = \dfrac{2\Delta v_{F1}}{s}\dfrac{(s+\frac{Z_{c(1)}}{L_{dc}+L_{eq}})}{(Z_{c(1)}+sL_{dc})(s+\frac{Z_{c(1)}}{L_{dc}+2L_{eq}})}), \\ v_{(1)34}(s) = \dfrac{2\Delta v_{F1}}{s}(1-\dfrac{Z_{c(1)}(s+\frac{Z_{c(1)}}{L_{dc}+L_{eq}})}{(Z_{c(1)}+sL_{dc})(s+\frac{Z_{c(1)}}{L_{dc}+2L_{eq}})}). \end{cases} \tag{6.3}$$

Given that $L_{dc}+L_{eq}$=43.33 mH $\approx L_{dc}+2L_{eq} = 46.66$ mH. We can further simplify (6.3) as:

$$\begin{cases} i_{(1)34}(s) = \dfrac{2\Delta v_{F1}}{s}\cdot\dfrac{1}{Z_{c(1)}+sL_{dc}}, \\ v_{(1)34}(s) = \dfrac{2\Delta v_{F1}}{s}\cdot\dfrac{sL_{dc}}{Z_{c(1)}+sL_{dc}}. \end{cases} \tag{6.4}$$

Following the fault analysis performed in Chapter VI, $i_{(1)34}(s)$ and $v_{(1)34}(s)$ in (6.4) can be further extended as explained in [66], [97] by considering the attenuation effect of line-mode TWs along the fault location l:

$$\begin{cases} i_{(1)34}(s) = \dfrac{2\Delta v_{F1}}{s}\cdot\dfrac{1}{Z_{c(1)}+sL_{dc}}\cdot\dfrac{1-kl}{1+s\cdot\tau l}\cdot e^{-s\cdot\frac{l}{v_{(1)}}}, \\ v_{(1)34}(s) = \dfrac{2\Delta v_{F1}}{s}\cdot\dfrac{sL_{dc}}{Z_{c(1)}+sL_{dc}}\cdot\dfrac{1-kl}{1+s\cdot\tau l}\cdot e^{-s\cdot\frac{l}{v_{(1)}}}. \end{cases} \tag{6.5}$$

As described in Figure 6.2 (a), we assume the direction of the forward traveling waves (FTWs) is from the DC bus to the cable. In contrast, the direction of the backward traveling waves (BTWs) is from the cable to the DC bus. Since the wavefront of BTWs monitored at relay units is not refracted or reflected by the line boundaries, it is more possible

that we can obtain the analytical expressions of their waveforms, which are closer to those in practical engineering. As a result, the BTWs are preferred to study the initial fault characteristics than FTWs.

According to the TW theory [97], the line-mode voltage $v_{(1)}(l,t)$ and the current $i_{(1)}(l,t)$ propagate with the time and space. The expressions for $v_{(1)}(l,t)$ and $i_{(1)}(l,t)$ in the line-mode network can be seen as [107]:

$$\begin{cases} v_{(1)}(l,t) = v_{f(1)}\left(t - \dfrac{l}{v_{(1)}}\right) + v_{b(1)}\left(t + \dfrac{l}{v_{(1)}}\right), \\ i_{(1)}(l,t) = \left[v_{f(1)}\left(t - \dfrac{l}{v_{(1)}}\right) - v_{b(1)}\left(t + \dfrac{l}{v_{(1)}}\right)\right] / Z_{c(1)}, \end{cases} \tag{6.6}$$

where $v_{f(1)}$ is the voltage FTWs and $v_{b(1)}$ is voltage BTWs in the line-mode network.

According to (6.6), the BTWs of voltage/current $v_{b(1)34}(s)$ and $i_{b(1)34}(s)$ at relay R_{34} can be calculated as:

$$v_{b(1)34}(s) = \frac{v_{(1)34}(s) - Z_{c(1)}\, i_{(1)34}(s)}{2}, \quad i_{b(1)34}(s) = \frac{-v_{b(1)34}(s)}{Z_{c(1)}}. \tag{6.7}$$

Combing (6.5) and (6.7), the expression of $i_{b(1)34}(s)$ with fault location l becomes:

$$\begin{aligned} i_{b(1)34}(s) &= \frac{Z_{c(1)}\, i_{(1)34}(s) - v_{(1)34}(s)}{2Z_{c(1)}} \\ &= \frac{\Delta v_{F1}}{sZ_{c(1)}} \cdot \frac{1 - k_0 l}{1 + s \cdot \tau l} e^{-s \cdot \frac{l}{v_{(1)}}} = A_0 \left(\frac{1}{s} - \frac{1}{s + 1/\tau_0}\right) e^{-s \cdot T_{d0}} \end{aligned} \tag{6.8}$$

Using the *Inverse Laplace Transform*, we obtain the following time domain expression for $i_{b(1)34}(t)$:

$$i_{b(1)34}(t) = A_0 \left(1 - e^{-\frac{t - T_{d0}}{\tau_0}}\right) u(t - T_{d0}), \tag{6.9}$$

where in (6.9), the function $u(t - T_{d0})$ represents a step function with a time delay of $T_{d0} = l / v_{(1)}$. The values of A_0 and τ_0 can be calculated as:

$$A_0 = \frac{\Delta v_{F1}(1 - k_0 l)}{Z_{c(1)}}, \tau_0 = \tau l. \tag{6.10}$$

where the values for k_0 and τ are set as $k_0 = 5.0 \times 10^{-5}$/km, and $\tau = 5.985 \times 10^{-7}$s/km for the tested cable model.

Similarly, the expression for the $i_{b(1)43}(t)$ measured at relay unit R_{43} can be expressed as:

$$i_{b(1)43}(t) = A_0' \left(1 - e^{-\frac{t - T_{d0}'}{\tau_0'}}\right) u\left(t - T_{d0}'\right), \tag{6.11}$$

where the values for A_0', T_{d0}' and τ_0' can be obtained by replacing l with $(L - l)$ in (6.10). L is the length of cable l_{34}.

6.3. PROPOSED FAULT LOCATION METHOD

This section introduces the AMLM algorithm for the parameter fitting of the BTWs of currents derived in the last section. Based on the fitted parameters, the proposed single-ended fault location method for the MTDC system is detailed.

Whether in the actual HVDC engineering or a simulation platform, the expressions derived for $i_{b(1)34}(t)$ and $i_{b(1)43}(t)$ are not continuous signals. The signals $i_{b(1)34}(t)$ and $i_{b(1)43}(t)$ are sampled discrete data, and the density of the data set depends on the sampling frequency.

According to (6.9) and (6.11), the fault location l can be determined when the values of A_0, τ_0 or A_0', and τ_0' can be obtained from the sampled data of $i_{b(1)34}(t)$ and $i_{b(1)43}(t)$. In this case, non-linear parameter fitting, a method used to analyze complex relationships in discrete data, is a useful approach to verify the analytical expressions of $i_{b(1)34}(t)$ and $i_{b(1)43}(t)$ and fit the discrete data from the protection measurements.

The objective of parameter fitting is to adjust parameters in a non-linear function to minimize the differences between the sampled and fitted data. This process can be regarded as a nonlinear least squares optimization problem. In our case, these functions are the exponential functions for $i_{b(1)34}(t)$ and $i_{b(1)43}(t)$, and the parameters to be fitted are A_0, τ_0 or A_0', and τ_0', as derived in (6.9) and (6.11).

We first define the merit function as:

$$\min_{x \in R^2} \|H(x)\|^2, \tag{6.12}$$

Taking $i_{b(1)34}(t)$ as an example, the error function for parameter fitting is:

$$H(x) = i_{b(1)34} - A_0(1 - e^{-\frac{t-T_{d0}}{\tau_0}}), \tag{6.13}$$

Here x is a two dimensional vector: $x = [A_0, \tau_0]_{1\times 2}$.

6.3.1. AMLM-BASED PARAMETER FITTING

The aim of the following analysis is to find the optimal parameters that minimize the squared residuals of the merit function (6.12) of the nonlinear least-squares problem. This thesis adopts the AMLM algorithm [108] for parameter fitting, which has been proved in [97] that significantly reduces the number of iteration steps to converge to the optimal solution compared to the classic Levenberg-Marquardt (LM) algorithm in [109].

The iterate x_k at each step using AMLM algorithm is computed by:

$$x_{k+1} = \begin{cases} x_k + \delta_k, & \text{if } r_k = \frac{\|H_k\|^2 - \|H(x_k+\delta_k)\|^2}{\|H_k\|^2 - \|H_k + G_k\delta_k\|^2} \geq p_0, \\ x_k, & \text{otherwise,} \end{cases} \tag{6.14}$$

In (6.14), the condition $r_k \geq p_0$ controls the adaptive step size δ_k at the k th iteration during successive iterations.

The determination of δ_k is the key of the AMLM algorithm, which decides the direction for searching the optimal solution of the next iteration of the x_{k+1}. Different algorithms have different computational principles of δ_k, which leads to differences in

the iteration speed and accuracy. For example, in Newton's method, the $H(x_k)$ must be differentiate, and the δ_k is determined as:

$$\delta_k = -\frac{H^{'}(x_k)}{H^{"2}(x_k)} \tag{6.15}$$

where $H^{'}(x_k)$ and $H^{"2}(x_k)$ are the first derivative and second order derivative of $H(x_k)$, respectively.

When applying AMLM algorithm, the δ_k is calculated as:

$$\delta_k = \frac{-G_k^T H_k}{\left(G_k^T G_k + \lambda_k I\right)} \tag{6.16}$$

where I is an 2×2 identity matrix. λ_k is the LM parameter which is computed as follows:

$$\lambda_{k+1} = \begin{cases} \lambda_k, & \text{if } r_k \geq p_1 \text{ and } s < t, \\ \beta_{k+1} \left\| H_{k+1} \right\|^{\delta}, & \text{otherwise,} \end{cases} \tag{6.17}$$

where

$$\beta_{k+1} = \begin{cases} c_1 \beta_k, & \text{if } r_k < p_2, \\ \beta_k, & \text{if } p_2 \leq r_k \leq p_3, \\ \max\left\{c_2 \beta_k, \beta_{\min}\right\}, & \text{if } r_k > p_3. \end{cases} \tag{6.18}$$

The G_k is the Jacobian J_k, which is $[-1 + e^{-\frac{t}{\tau_0}}, \frac{A_0 t}{{\tau_0}^2} e^{-\frac{t}{\tau_0}}]$, or the Jacobian used at the last iteration step x_k:

$$G_{k+1} = \begin{cases} G_k, & \text{if } r_k \geq p_1 \text{ and } s < t, \\ J_{k+1}, & \text{otherwise,} \end{cases} \tag{6.19}$$

where s and t are to count the iterations, and t is set as 10 to accelerate the iteration process.

The condition $\left\| G_k^T H_k \right\| \leq 10^{-5}$ is used to decide whether or not to terminate the iterations. Specifically, when the condition $\left\| G_k^T H_k \right\| \leq 10^{-5}$ is met, it shows that the algorithm converges superlinearly under a small tolerance, and the iteration process should be terminated. The current solution $x_k = [A_{0,k}, \tau_{0,k}]$ is optimal for (6.12). Otherwise, the AMLM algorithm continues to the next iteration until the condition of $\left\| G_k^T H_k \right\| \leq 10^{-5}$ is met. The x_k is updated using (6.14).

The parameter fitting for $i_{b(1)43}(t)$ can be achieved following the above procedures by replacing the l with $(L - l)$ in the error and merit function in (6.12)-(6.13).

Following the above procedures, the optimal parameters A_0, τ_0 or A_0', and τ_0' for (6.12) can be obtained using the AMLM algorithm.

6.3.2. SINGLE-ENDED FAULT LOCATION METHOD

In (6.9) and (6.11), it is evident that the parameters A_0, τ_0 or A_0', and τ_0' contain information about the fault location l. However, deriving l directly in terms of A_0 or A_0' is complicated, as it is also influenced by the fault type and the fault resistance R_f according to

Table. 4.3. In contrast, the parameters τ_0 and τ_0' are solely associated with l, making it a preferred indicator for fault location.

As the DC fault in l_{34} is the internal fault for both relay units R_{34} or R_{43}, the fault location can be determined either using the sampled data $i_{b(1)34}$ or $i_{b(1)43}$ (without data exchange between R_{34} and R_{43}).

To ensure the accuracy of fault location, the proposed method first fits the sampled data $i_{b(1)34}$ and $i_{b(1)43}$, and selects the data with higher R^2 values for subsequent fault locations. Here, the R^2 is an efficient index to evaluate the performance of the AMLM-based parameter fitting. The formula for R^2 is:

$$R^2 = 1 - \frac{R_{SS}}{T_{SS}} \tag{6.20}$$

where R_{SS} and T_{SS} are the residual and total sum of squares, respectively. The R^2 value ranges from 0 to 1, where a higher value indicates a better fit between fitted and simulated data.

As such, the estimated fault location l^* is:

$$l^* = \begin{cases} \frac{\tau_0}{\tau}, & \text{if } R_{34}^2 \geq R_{43}^2, \\ L - \frac{\tau_0'}{\tau}, & \text{otherwise,} \end{cases} \tag{6.21}$$

Using (6.16)-(6.21), the fault location method using the AMLM algorithm can be formulated as the following **Algorithm 1**:

6.3.3. DATA WINDOW AND RESULTS EVALUATION

To ensure that the selected data is as close as possible to (6.9) and (6.11), the data window is chosen from either $(t_0, t_1 + t_d)$ or $(t_0', t_1' + t_d)$ for parameter fitting. Here, t_0 and t_0' are the time instants when the fault-induced TWs arrive at the relay units R_{34} and R_{43} with time delays of T_{d0} and T_{d0}', respectively. t_1 and t_1' are the times when $i_{b(1)34}(t)$ and $i_{b(1)43}(t)$ reach their peak values. t_d is a short time window of 50 μs added to improve anti-noise interference ability.

Taking the $i_{b(1)34}(t)$ measured at relay unit R_{34} as an example, the selected time window $(t_0, t_1 + t_d)$ used for parameter fitting is illustrated in Figure 6.3 (assuming the fault occurs at 1.0 s).

To evaluate the accuracy of the proposed fault location method in the following contents, the error is defined by:

$$e = \left| \frac{l - l^*}{L_{cable34}} \right| \% \tag{6.22}$$

where $L_{cable34}$ is 200 km.

6.4. PSCAD SIMULATION TEST

The simulations are carried out in the PSCAD/EMTDC environment for the MMC-MTDC system shown in Figure 6.1. All the faults are set at cable l_{34}. The data are measured from the relay units R_{34} and R_{43}. In practice, cable faults are commonly caused by metallic

Algorithm 1 The proposed fault location method using the adaptive multi-step Levenberg Marquardt algorithm

Require: Sampled $i_{b(1)34}$, $i_{b(1)43}$
Require: $x_1 \in R^2, c_1 > 1 > c_2 > 0, 0 < p_0 < p_2 < p_1 < p_3 < 1, 1 \le \delta \le 2, t \ge 1, \beta_1 > \beta_{min} > 0$
Ensure: Set $G_1 = J_1$, $\lambda_1 = \beta_1 \|H_1\|^{\delta}$, $k = 1, s = 1, i = 1, k_i = 1$
  $p_0 \leftarrow 0.0001$, $p_1 \leftarrow 0.50$, $p_2 \leftarrow 0.25$, $p_3 \leftarrow 0.75$
  $c_1 \leftarrow 4.0$, $c_2 \leftarrow 0.25$,
  $\beta_1 \leftarrow 10^{-5}$, $\beta_{min} \leftarrow 10^{-8}$
  while $\left\| G_{k_i}^T H_{k_i} \right\| \neq 0$ **do**
    $\delta_k \leftarrow -G_k^T H_k / \left(G_k^T G_k + \lambda_k I\right)$ ▷ (6.16)
    $\beta_{k+1} \leftarrow c_1$ or β_k or $\max\{c_2\beta_k, \beta_{\min}\}$ ▷ (6.18)
    $\lambda_{k+1} \leftarrow \lambda_k$ or $\beta_{k+1}\|H_{k+1}\|^{\delta}$ ▷ (6.17)
    $x_{k+1} \leftarrow x_k + \delta_k$ ▷ (6.14)
    if $r_k \ge p_1$ and $s < t$ at x_k **then** ▷ (6.19)
      $G_{k+1} \leftarrow G_k$, $s = 1, i = i + 1, k_i = k$.
    else if Otherwise **then**
      $G_{k+1} \leftarrow J_k$, $s = s + 1$.
    end if
    if $\left\| G_k^T H_k \right\| \le 10^{-5}$ **then**
      Terminate iteration ▷ x_k is optimal for (6.12)
    else if $\left\| G_k^T H_k \right\| > 10^{-5}$ **then**
      $k = k + 1$
    end if
  end while
    Return A_0, τ_0, A_0', τ_0'
  if $R_{34}^2 \ge R_{43}^2$ **then** ▷ (6.21)
    $l^* \leftarrow \frac{\tau_0}{\tau}$ ▷ Data in R_{34} is used
  else if $R_{34}^2 \le R_{43}^2$ **then** ▷ Data in R_{43} is used
    $l^* \leftarrow L - \frac{\tau_0'}{\tau}$
  end if
    Return l^*

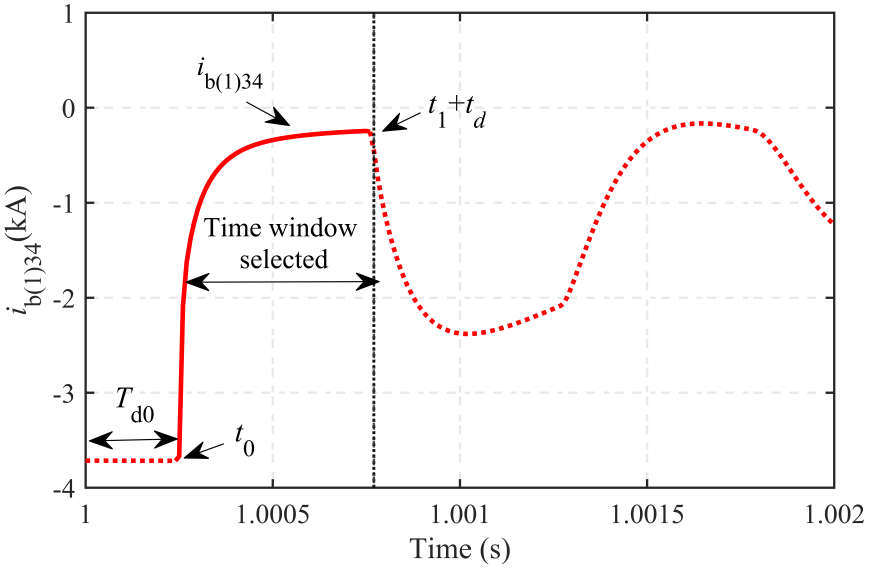

Figure 6.3: Time window illustration for parameter fitting.

damage [36]. Due to this, the faults with large R_f values are not considered. The sampling frequency f_s of 200 kHz in PSCAD/EMTDC was chosen for testing the method, which is technically possible to achieve in practice.

6.4.1. FAULT LOCATION PERFORMANCE

Taking PTP faults as examples, the parameter fitting that results with different fault locations can be seen in Figure 6.4. It is noted that the data of $i_{b(1)34}(t)$ presented in Figure 6.4 has been selected using the time window $(t_0, t_1 + t_d)$ explained in Figure 6.3.

It is concluded that the fitted waveform (dotted lines) of $i_{b(1)34}$ by the AMLM algorithm closely matches the simulated one (solid lines), which proves the previous analytical expressions derived in (6.9) and the accuracy of the adopted AMLM algorithm. The data window selected varies depending on the fault location. Generally, the farther the fault location, the longer the data window is selected (meaning more sampled data can be used). This often results in higher R^2 values and more precise fitting results. This phenomenon is mainly due to the different TWs time delays of T_{d0} and peak value, which have been concluded from previous analysis.

The inability to fully match the fitted waveform and simulated one is because the expression of $i_{b(1)34}$ in (6.9) is the result after a series of simplifications of fault circuits and TW theory. Considering the complex structure of the MTDC system, especially the effects of MMC and DCCB on the reflection and injections of TWs, it is impossible to obtain a completely accurate expression for the $i_{b(1)34}$. However, based on the results in Figure 6.4, the derived expression for $i_{b(1)34}$ in (6.9) is very close to the simulated waveforms, showing that the parameter fitting results are accurate enough and can be used

for fault location estimation.

Additional testing results evaluated using the R^2 are presented in Figure 6.5. The simulated fault locations range from 10 km to 190 km in cable l_{34}. Almost all the R^2 values are close to 1.0. The results indicate that the AMLM algorithm has successfully optimized the objective function in (6.13). The AMLM-based parameter fitting yields highly accurate indexes regardless of the fault location or fault type. Consequently, the fitted data τ_0 and τ_0' can be used for estimating the fault location.

Typical PTG and PTP faults are simulated to validate the proposed fault location method, and the results are given in Table. 6.1. According to Table. 6.1, the proposed method has well-estimated the fault locations. The fault location errors are less than 0.4% for all presented scenarios. These results confirm that the proposed method has a desirable TWs parameter fitting ability and is employable for fault location purposes.

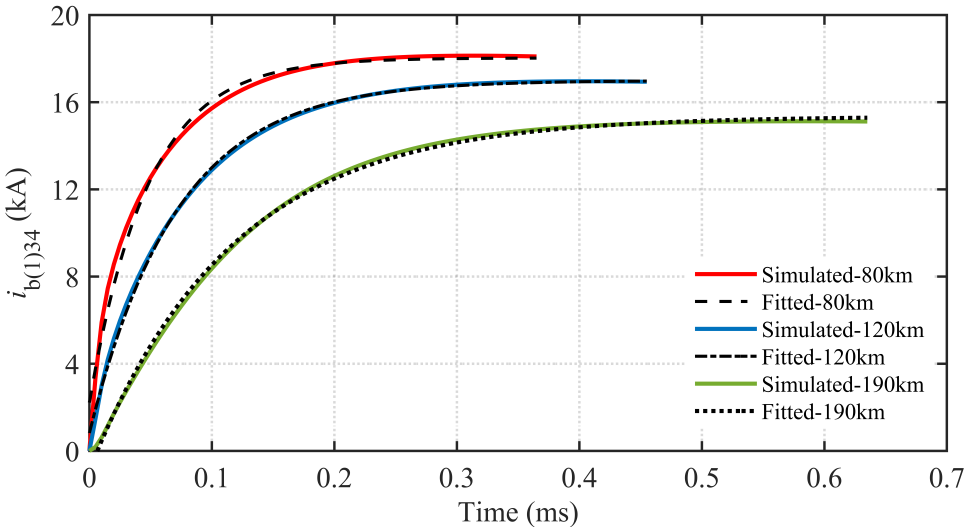

Figure 6.4: Parameter fitting results for $i_{b(1)34}$ under PTP faults.

6.4.2. INFLUENCE OF DC INDUCTOR

In (6.5), it is proven that L_{dc} impacts the propagation process of TWs as it reflects voltage/current TWs when they arrive at the relay units. To verify the influence of L_{dc} on the performance of parameter fitting and fault location, six independent DC faults with various sizes of L_{dc} are simulated in the tested system. Taking the fault f_{34}|PTG(l = 110km) as an example, the parameter fitting results are shown in Figure 6.6. Due to the different sizes of L_{dc}, the TWs of $i_{b(1)34}$ after faults and the data window used for parameter fitting vary accordingly. The smaller the value of L_{dc}, the shorter the data window length. This is because the L_{dc} limits the current increasing rate. However, the AMLM fitting algorithm still performs well in all cases, as shown in Figure 6.6. The fitted waveform (dotted

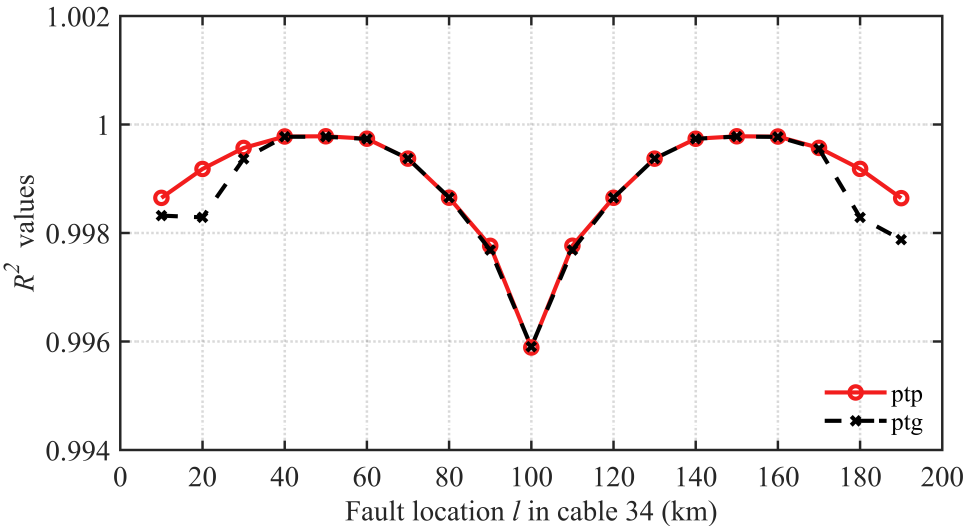

Figure 6.5: Results evaluation of parameter fitting using R^2 values.

line) almost fully matches the simulated (solid line) waveform.

Table. 6.2 lists the corresponding fault location results. Since L_{dc} is a system parameter, the value of τ must be adjusted for parameter fitting when different values of L_{dc} are used. Specifically, for $L_{dc} \in \{20\text{ mH}, 60\text{ mH}, 80\text{ mH}, 100\text{ mH}\}$, $\tau \in \{5.559 \times 10^{-7}, 6.2383 \times 10^{-7}, 6.405 \times 10^{-7}, 6.6325 \times 10^{-7}\}$, respectively. The results demonstrate that, with a reasonable selection of τ values, the proposed method exhibits a high degree of independence from the size of L_{dc}. Moreover, the estimated error e exhibits only marginal changes in response to variations in the size of L_{dc}, remaining within an acceptable range. This also indicates that the proposed method can be flexibly applied to other MTDC systems and can be used in conjunction with DC protection algorithms that do not rely on boundary devices.

6.4.3. NOISE TESTS

The AMLM-based parameter fitting and fault locations results considering the SNR of 35 dB and 40 dB levels are given in Figure 6.7 and Table. 6.3. These noises are added to the original simulated waveforms of $i_{b(1)34}(t)$ to study the robustness of the AMLM parameter fitting algorithm and corresponding fault location accuracy.

According to Figure 6.7, the parameter fitting is minimally affected by noise interference, and the waveform of $i_{b(1)34}(t)$ can be well fitted with the R_2 values of 0.99754 and 0.99879, respectively. The fitted waveforms still exhibit smooth exponential functions, closely matching the simulated ones, without any outliers.

As the noise is stochastic, this paper repeated each set of noise tests 50 times. The results, e.g., R^2, l^* and e in Table. 6.3, are all averaged values. As expected, the noise impacts the performance compared with the results in Table. 6.3. This is because the

Table 6.1: Results of the Fault Location Method (Metallic Fault)

Scenario	l^* (km)	e(%)	Scenario	l^* (km)	e(%)
f_{34}|PTG(l = 30km)	29.9685	0.0157	f_{34}|PTP(l = 30km)	29.8193	0.0903
f_{34}|PTG(l = 40km)	40.2723	0.1361	f_{34}|PTP(l = 40km)	40.4864	0.2431
f_{34}|PTG(l = 50km)	49.9017	0.0491	f_{34}|PTP(l = 50km)	49.6853	0.1573
f_{34}|PTG(l = 80km)	80.7592	0.3798	f_{34}|PTP(l = 60km)	60.5644	0.2822
f_{34}|PTG(l = 90km)	89.9084	0.0457	f_{34}|PTP(l = 80km)	80.555	0.2775
f_{34}|PTG(l = 110km)	110.1069	0.0534	f_{34}|PTP(l = 120km)	119.4688	0.2656
f_{34}|PTG(l = 120km)	119.3202	0.3398	f_{34}|PTP(l = 140km)	139.4427	0.2786
f_{34}|PTG(l = 150km)	150.1790	0.0894	f_{34}|PTP(l = 150km)	150.2883	0.1441
f_{34}|PTG(l = 160km)	159.8010	0.0994	f_{34}|PTP(l = 160km)	159.4507	0.2746
f_{34}|PTG(l = 170km)	169.9483	0.0258	f_{34}|PTP(l = 170km)	170.1694	0.0846

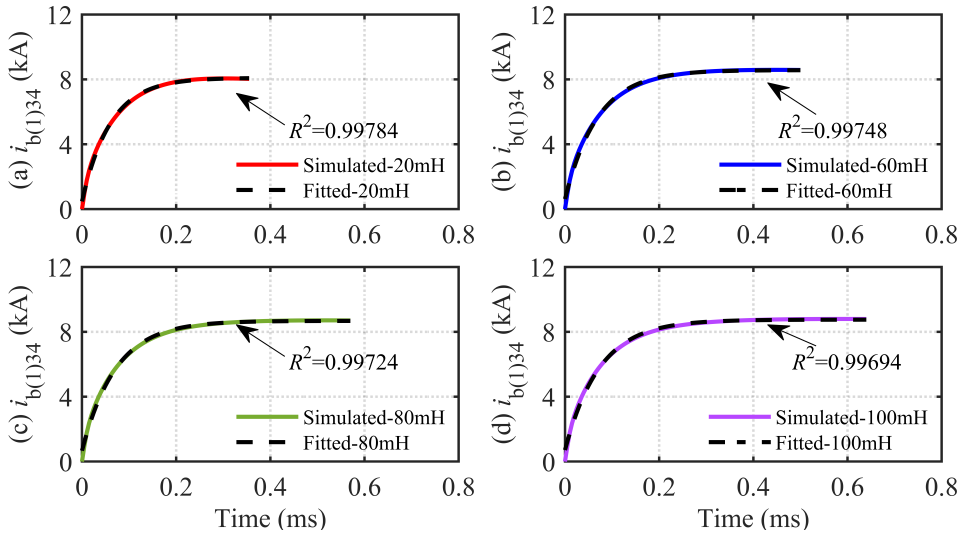

Figure 6.6: Parameter fitting results for $i_{b(1)34}$ with various sizes of L_{dc}. (a)L_{dc} = 20 mH;(b)L_{dc} = 60 mH;(c)L_{dc} = 80 mH;(d)L_{dc} = 100 mH.

noise may affect the selected data window, reducing the R^2 of parameter fittings, and the value of τ is fixed in (6.21).

The largest error is 0.4119% when the f_{34}|PTP(l = 60km) fault occurs. Overall, the fault location results under noise are accurate as all the estimated errors are smaller than 0.5%, indicating that the proposed method has a high tolerance to noise up to 35 dB. Compared to the methods developed in [32], [49], this method exhibits significantly improved anti-noise ability. However, it is worth noting that when there are higher noise levels in the measurements (i.e., a decrease in SNR), the DC fault location becomes more challenging, particularly for faults near the cable terminals. This would be one of the

Table 6.2: Influence With Different DC Inductors

Scenario	L_{dc} = 20 mH			L_{dc} = 60 mH		
	R^2	l^* (km)	e(%)	R^2	l^* (km)	e(%)
f_{34}|PTG(l = 50km)	0.99943	49.1671	0.4164	0.99988	50.2065	0.1032
f_{34}|PTG(l = 110km)	0.99784	109.6796	0.1602	0.99748	110.7108	0.3554
f_{34}|PTG(l = 150km)	0.99943	150.8419	0.4209	0.99988	149.8727	0.0636
f_{34}|PTP(l = 80km)	0.99875	80.7125	0.3563	0.99848	79.9116	0.0442
f_{34}|PTP(l = 140km)	0.99958	139.5485	0.2258	0.99973	139.5749	0.2125
f_{34}|PTP(l = 170km)	0.99903	170.4169	0.2084	0.99985	169.8425	0.0788
Scenario	L_{dc} = 80 mH			L_{dc} = 100 mH		
	R^2	l^* (km)	e(%)	R^2	l^* (km)	e(%)
f_{34}|PTG(l = 50km)	0.99986	49.9345	0.0328	0.99977	49.8645	0.0678
f_{34}|PTG(l = 110km)	0.99724	110.7103	0.3552	0.99694	110.7833	0.3916
f_{34}|PTG(l = 150km)	0.99986	150.1212	0.0606	0.99785	149.8734	0.0633
f_{34}|PTP(l = 80km)	0.99825	80.0269	0.0135	0.99793	79.7753	0.1124
f_{34}|PTP(l = 140km)	0.99958	139.548	0.2260	0.99928	139.9985	0.0007
f_{34}|PTP(l = 170km)	0.99991	170.0706	0.0353	0.99969	170.2024	0.2024

future work directions to improve the proposed parameter fitting-based fault location method performance further. However, the anti-noise ability of 35 dB level is sufficiently robust in most of the cases in practice.

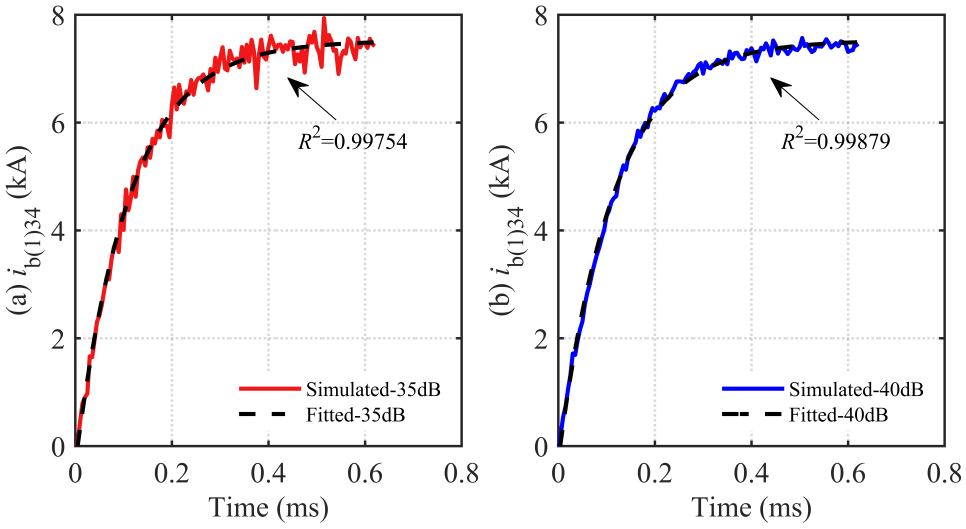

Figure 6.7: Parameter fitting under fault f_{34}|PTP(l = 170km): (a) SNR = 35 dB; (b) SNR = 40 dB.

Table 6.3: Noise Test Results With Different Noise Levels

Scenario	SNR=35 dB			SNR=40 dB		
	R^2	l^* (km)	e(%)	R^2	l^* (km)	e(%)
f_{34}|PTG(l = 30km)	0.99783	29.9468	0.0266	0.9998	30.4243	0.2122
f_{34}|PTG(l = 50km)	0.99812	49.9353	0.0323	0.9998	50.3067	0.1533
f_{34}|PTG(l = 90km)	0.99687	89.8664	0.0668	0.9998	89.9943	0.0029
f_{34}|PTG(l = 110km)	0.99543	109.5268	0.2366	0.9998	110.2812	0.1406
f_{34}|PTG(l = 150km)	0.99748	150.7124	0.3562	0.9998	150.1285	0.0643
f_{34}|PTP(l = 60km)	0.99932	60.5852	0.2926	0.9998	60.8238	0.4119
f_{34}|PTP(l = 80km)	0.99821	80.4659	0.2329	0.9997	80.8013	0.4007
f_{34}|PTP(l = 120km)	0.99856	119.5590	0.2205	0.9998	119.3413	0.3293
f_{34}|PTP(l = 140km)	0.99927	139.6921	0.1540	0.9996	139.7577	0.1211
f_{34}|PTP(l = 170km)	0.99616	169.9110	0.0445	0.9995	170.0398	0.0199

6.4.4. PERFORMANCE WITH LOWER SAMPLING FREQUENCIES

The sampling frequency in PSCAD/EMTDC is a key factor that affects the performance of parameter fitting. It determines the data window length used for the sampled data of $i_{b(1)34}(t)$ and $i_{b(1)43}(t)$ in **Algorithm** 1. This section investigates the performance of the proposed fault location method under various sampling frequencies.

Here, six metallic faults are performed to investigate the performance with lower sampling frequencies. According to the R^2 values in Table. 6.4, the adopted AMLM **Algorithm** 1 can still optimize (6.12) to obtain the corresponding indexes for fitted TWs curve well for lower f_s. However, the accuracy of parameter fitting and fault location are influenced compared to the results in Table. 6.1. This is due to a significantly reduced data window with a lower sampling frequency. Taking the fault f_{34}|PTG(l = 140km) as an example, the number of discrete sampling data used for AMLM parameter fitting is 9 and 23 under f_s being 20 kHz and 50 kHz, respectively. However, when f_s is 200 kHz, the number of data that can be utilized jumps to 90. More work is needed in the future to improve these shortcomings.

Table 6.4: Influence With Lower Sampling Frequency f_s

Scenario	f_s = 50 kHz			f_s = 20 kHz		
	R^2	l^* (km)	e(%)	R^2	l^* (km)	e(%)
f_{34}|PTG(l = 130km)	0.99929	128.1488	0.9256	0.99992	132.0088	1.0044
f_{34}|PTG(l = 140km)	0.99978	140.1209	0.0604	0.99993	139.9478	0.0261
f_{34}|PTG(l = 150km)	0.99982	151.1544	0.5772	0.99994	147.0590	1.4705
f_{34}|PTP(l = 110km)	0.99691	107.2704	1.3648	0.99991	112.2724	1.1362
f_{34}|PTP(l = 120km)	0.99958	125.4541	2.7271	0.99995	119.5548	0.2226
f_{34}|PTP(l = 130km)	0.99930	130.0928	0.0928	0.99997	125.5855	2.2073

6.5. RTDS SIMULATION TEST

To investigate the fault location method, a ±525 kV three-terminal meshed MMC-HVDC system is modeled in RTDS as depicted in Figure 6.8.

6.5.1. TESTING SYSTEM IN RTDS

In RTDS/RSCAD, the most detailed MMC valve model: *'rtds_vsc_FPGA_GM'* is applied for MMC2 and MMC3[110], while the average one is adopted for MMC1. The Xilinx Virtex-7 FPGA board (GTFPGA) is used for RTDS [111] due to its high computation and parallel processing ability. Three GTFPGA units are required to represent one MMC unit. Since the capacitor voltage across all SMs must be balanced and equal, two additional GTFPGA units are required to realize the capacitor voltage balancing and firing pulse control. In this work, the odd-even sorting algorithm is utilized [112]. The number of SMs inserted per time step is calculated using the Nearest Level Control (NLC) selection technique. Thus, five GTFPGA units are required to represent one of the detailed model $'rtds\_vsc\_FPGA\_GM'$ for MMC2 and MMC3.

Cross-rack communication is achieved via a global bus hub and an IRC switch. The racks are connected to the GTFPGA units via the GTIO port, with signal exchanges facilitated by two full-duplex fiber optic cables using the high-speed Aurora protocol.

Table.6.5 lists the system parameters.

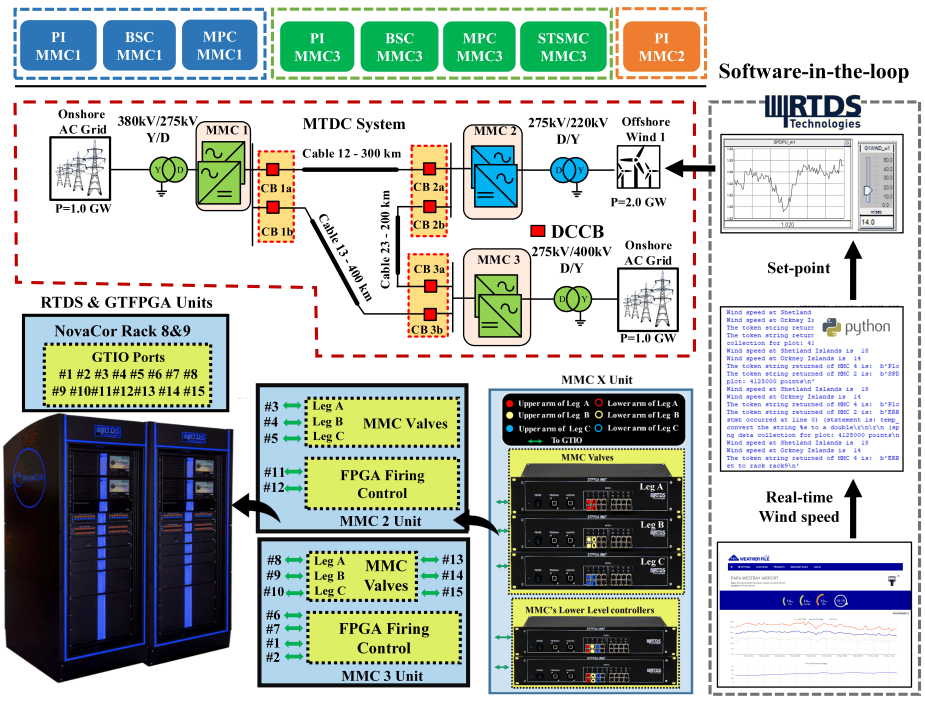

Figure 6.8: Configuration of the ± 525kV three-terminal meshed MMC-HVDC system.

Suitable cable ratings are required to link the offshore wind farms to the onshore grid

Table 6.5: System Parameters

Item	Converters		
	MMC1	MMC2	MMC3
Rated Active Power	1000 MW	2000 MW	1000 MW
Control Mode	V_{dc}/V_{ac}	P_{ac}/Q_{ac}	v_{ac}/f
AC Grid Voltage	380 kV	220 kV	400 kV
DC Link Voltage	±525 kV		
SMs Number Per Arm	200		
Arm Capacitance	15000 μF		
Arm Inductance	39.7 mH		
DC Inductance	20 mH		
AC Converter Voltage	275 kV		
Transformer Inductance	0.18 p.u.		

system. The submarine XLPE cable is used and modeled within the RTDS environment using a dependent model (phase domain). The parameters of the cables are taken from [76]. The length of cable12, cable23, and cable13 are 300 km, 200 km, and 400 km, respectively.

MMC1 and MMC3 connect the strong onshore AC grid with 1 GW rated power. The offshore wind farms connect the DC grid through MMC2, built in small time steps with eight parallel connected type-4 wind turbines. An interface transformer connects the small time step model to the large time step model. It should be noted that the MTDC system, with BSC, MPC, and STSMC controllers (introduced in Chapter III), is programmed on one RTDS rack along with the onshore and DC grid, while the wind farm is modeled on another rack. A global bus hub and an IRC switch perform the cross-rack communication.

The software-in-the-loop (SIL) is used to extract the real-time wind speeds from the web by the *Selenium* tool, as illustrated in Figure 6.8. The online wind data are communicated through TCP/IP connection to RSCAD, the communication delay is 100 ms, and the data is updated every 2 s. The wind gust data is measured near the Orkney Islands (58.9809° N, 2.9605° W) and Shetland Islands (60.5297° N, 1.2659° W), which is adopted from [113].

This RTDS testing model is also used for the nonlinear controllers modeling using the methods presented in Chapter III. The interoperability of these controllers will be detailed in Chapter VII.

6.5.2. EXPERIMENTAL FAULT LOCATION RESULTS

Cable 12 in Figure 6.8 is selected as the testing cable. Typical DC faults of different fault locations and fault types are used to test the performance of the proposed fault location method. The sampling frequency is 20 kHz. The value of τ is set to 1.0255×10^{-6}. All the DC faults are metallic. Additional noise tests (each set is repeated 50 times) at 35 dB are performed to validate the anti-noise capability in the RTDS environment.

The obtained results of parameter fitting and detailed fault location are presented

in Figure 6.9 and Table. 6.6, respectively. It can be observed from Figure 6.9 that the proposed AMLM algorithm accurately fits the sampled TWs at relays R_{12} and R_{21}, with R^2 values approaching 1.0. Thus, the obtained parameters provide sufficiently accurate estimates for the fault location.

The results in Table. 6.6 demonstrate that the proposed method accurately estimates the fault location for both normal and noisy environments, with errors within 1.0%. Although the accuracy slightly decreases compared to Table. 6.1 in certain scenarios, it should be noted that this is due to the limitations of parameter fitting caused by a sampling frequency of 20 kHz. Overall, the results are presented in Table. 6.6 still yields satisfactory outcomes for the proposed method.

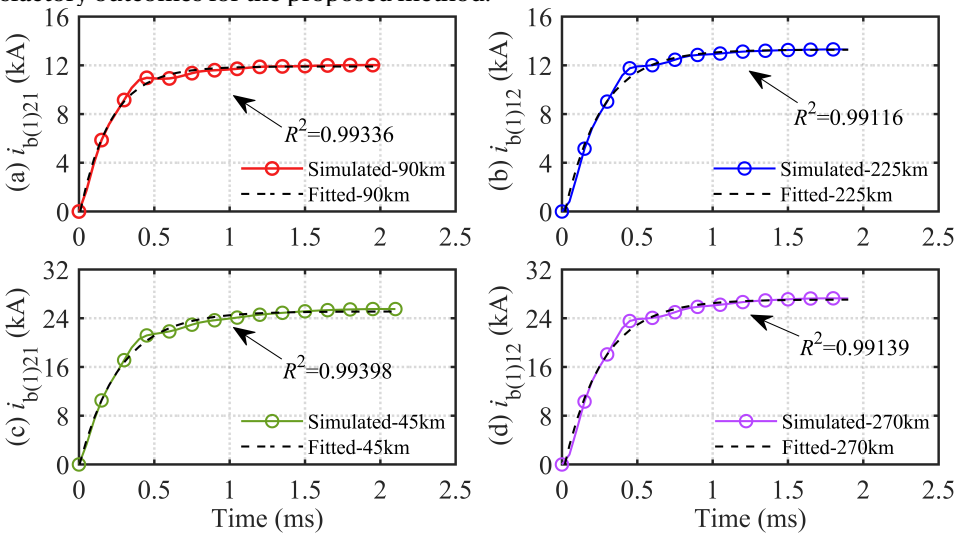

Figure 6.9: Parameter fitting results for $i_{b(1)34}$ under faults: (a) f_{12}|PTG(l = 90km); (b) f_{12}|PTG(l = 225km); (c) f_{12}|PTP(l = 45km); (d) f_{12}|PTP(l = 70km)

Table 6.6: Fault Location Results in RTDS Environment (Metallic Fault)

Scenario	Normal			SNR=35dB		
	R^2	l^* (km)	e(%)	R^2	l^* (km)	e(%)
f_{12}|PTG(l = 200km)	0.99354	199.5236	0.2382	0.99091	201.2945	0.6472
f_{12}|PTG(l = 210km)	0.99375	208.3584	0.8208	0.99087	209.8657	0.0672
f_{12}|PTG(l = 220km)	0.99349	219.4096	0.2952	0.99386	219.8608	0.0696
f_{12}|PTP(l = 200km)	0.99228	198.2448	0.8776	0.99269	198.8083	0.5958
f_{12}|PTP(l = 210km)	0.99232	208.1911	0.9044	0.9912	208.9830	0.5085
f_{12}|PTP(l = 220km)	0.99216	219.0346	0.4827	0.9918	219.7597	0.1202
f_{12}|PTP(l = 230km)	0.9920	230.0341	0.0170	0.99235	230.1496	0.0748
f_{12}|PTP(l = 240km)	0.9916	241.6480	0.8240	0.99073	240.9215	0.4607

6.6. CONCLUSION

This chapter proposes a new single-ended DC fault location method based on backward line-mode current TWs for the MTDC power system.

Based on the fault analysis, this chapter clarifies that the backward line-mode current TWs can be approximated to an exponential function with a parameter containing the fault location l. When the value of this parameter is obtained from the sampled backward line-mode current TWs data at relay units, the actual fault location can be estimated. As such, this chapter introduces the AMLM algorithm to solve the nonlinear least-squares problem for parameter fitting. The computation procedure of the AMLM algorithm is elaborated. Finally, the performance validation of the proposed fault location method is done via PSCAD/EMTDC and RTDS platforms through various faults.

According to the results, the proposed parameter fitting algorithm and fault location method are accurate, with all the R^2 values close to 1.0 (perfect fitting) and most errors being smaller than 0.5%. It also performs excellently with different sizes of DC inductors. The method does not require a high sampling frequency and communication channel, significantly reducing the hardware requirements and investment in practical applications. The noise tests are also carried out. The presented results confirm the superiority of the proposed fault location method in withstanding the 35 dB noises.

Compared with the existing fault location methods, the novelty and the main contributions of the fault location method in this chapter are threefold. Firstly, the proposed method provides a refined perspective on fault location in MTDC systems. It uses the fitted coefficients of the backward line-mode current TWs to estimate the fault location. Secondly, the proposed fault location method does not require an extremely high sampling frequency (100 kHz used) to detect the refraction/reflection time of TWs. This significantly reduces hardware requirements and investment in practical applications and guarantees fault location accuracy. Thirdly, the fault location accuracy under different fault types and the size of the DC inductor and noise disturbance are improved compared to existing methods.

To implement the proposed fault location method in other MTDC systems, it is necessary to determine suitable initial values required in **Algorithm** 1 and τ in (6.10) according to the previous analysis and system parameters. The length of t_d also needs to adapt to the maximum considered noise level and the sampling frequency of the system.

7

INTEROPERABILITY STUDY OF CONTROLLERS IN RTDS

This chapter investigates the MMC control Interoperability (IOP) for different transient processes. The most frequent contingencies of the practical projects, e.g., power flow variation, wind speed variation, and DC/AC grid faults, are simulated in RTDS with eight different control allocation scenarios. Each scenario presents different control capabilities for maintaining system stability. More precisely, the scenarios with non-linear controllers show faster settling time and fewer DC voltage and power variations. Controller switchings are also achieved without bringing large system oscillations. Finally, the optimal controller allocation to cope with system contingencies is provided in this chapter.

Parts of this chapter have been published in [53].

MMC control IOP is a crucial issue with different suppliers in the future multi-vendor MTDC systems. This chapter provides the control IOP study using the RTDS testing model described in Chapter VI. All the non-linear controllers are modeled using the methods presented in Chapter III.

This Chapter is structured as follows. Section 7.1 introduces the MMC controller allocations in the RTDs environment. Section 7.2 presents the validation results of the implemented controller's IOP issue through various system transients. Section 7.3 concludes this chapter.

7.1. MMC CONTROLLER ALLOCATIONS

The control hierarchy for the high power converter can be classified into three regions as depicted in Figure 7.1. Region 1 in Figure 7.1 represents the converter level control compresses of capacitor voltage balancing, circulating current suppression, and IGBT switching pluses. Typically, this region operates within tens or hundreds of microseconds. Region 2, in Figure 7.1, provides the reference signals for the control loops from region 1 based on the dispatch control signal provided by region 3. Region 2, also known as station-level control, has a few hundred milliseconds response time. This chapter focuses on Region 2, for which different controllers are implemented.

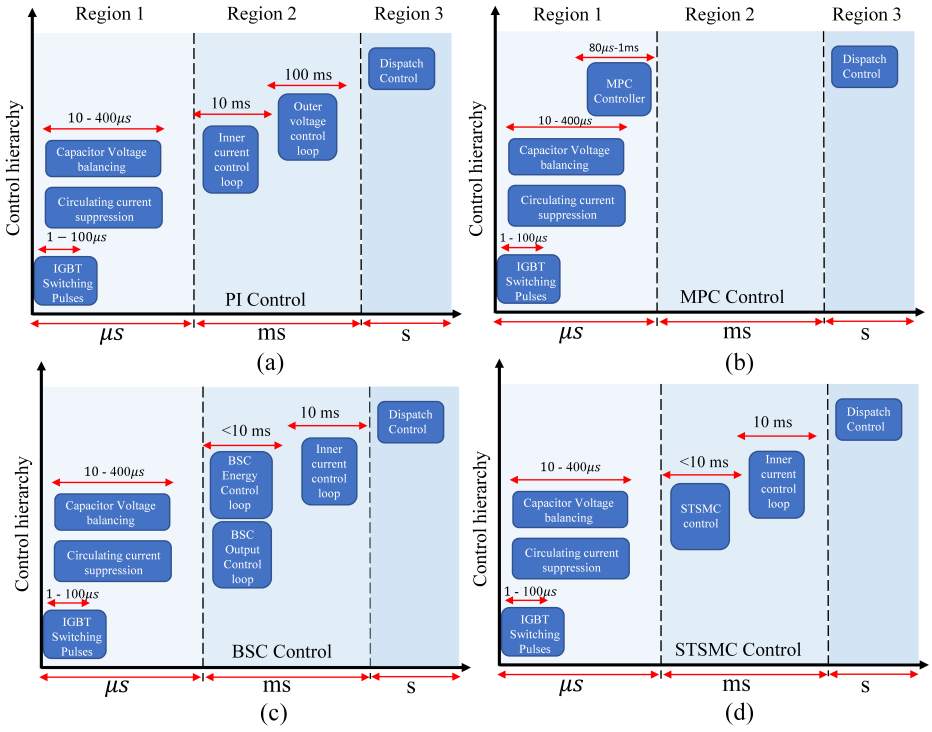

Figure 7.1: MMC control hierarchy: (a) PI hierarchy. (b) MPC hierarchy. (c) BSC hierarchy. (d) STSMC hierarchy.

In the studied system from Figure 6.8, all MMCs can be controlled via classical PI

controllers following the methods in Chapter II. Furthermore, the MPC method is implemented in MMC1 and MMC3. The BSC method is implemented in MMC1 and MMC3, and the STSMC is implemented in MMC3. To investigate the IOP and interactions of different controllers for MMC1 and MCM3, the following eight scenarios (twelve possible in total) are defined for simulation studies as Table. 7.1. The scenarios 'PI-MPC', 'MPC-PI', 'BSC-MPC', and 'BSC-PI' may result in unstable oscillatory behaviors. They are omitted due to the concern of their insufficient interoperability, which will be improved in the future.

Table 7.1: Different Control Allocation Scenarios for MMC1 and MMC3

Uniformed		Mixed	
Scenario	MMC1-MMC3	Scenario	MMC1-MMC3
S1	PI(V_{dc}/V_{ac})-PI(P_{ac}/Q_{ac})	S5	PI(V_{dc}/V_{ac})-BSC
S2	MPC-MPC	S6	MPC-STSMC
S3	BSC-BSC	S7	MPC-BSC
S4	PI(V_{dc}/V_{ac})-STSMC	S8	BSC-STSMC

7.2. INTEROPERABILITY RTDS SIMULATION STUDIES

In this section, an in-depth analysis is carried out to investigate the interoperability of various controllers. It is demonstrated that non-linear controllers achieve faster transitions with minimal DC voltage active power variations and current peak values during the system transients. Simulations are performed based on the three-terminal HVDC system described in Chapter VI in Figure 6.8 in RTDS.

We define the following indicators to assess the controller performance:

- t_r: Rise time for the response signal to increase/decrease from the initial value to 90 % of the expected value.
- t_s: Settling time for the response signal to reach and stay within a range of 3 % of expected value (error band).
- P_{var}: Maximum variation of active power during transient response.
- V_{var}: Maximum variation of DC voltage during transient response.
- i_P: Maximum peak current during transient response.

The investigated transient cases are:

- Case I: Step change of MMC3's active power from 0 p.u. to 0.5 p.u. at $t_0 = 0.1$ s (Event1) and increase to 1.0 p.u. at $t_1 = 1.1$ s (Event2).
- Case II: Temporary PTG fault occurs at cable12 outlet at $t_0 = 0.1$ s (Event1) and VARC DCCB re-closes at $t_1 = 1.1$ s (Event2).
- Case III: Step change of wind farms output power from 630 MW to 750 MW at $t_0 = 0.5$ s (Event1) and increase to 1000 MW $t_1 = 5.5$ s (Event2).

- Case IV: Temporary phase A grounding fault occurs at MMC1 AC gird at $t_0 = 0.1$ s (Event1), fault resistance is 1.0 Ω.
- Case V: MMC1's controller switching from PI to BSC at $t_0 = 0.1$ s (Event1), BSC to MPC at $t_1 = 1.1$ s (Event2), and MMC3 controller switching from PI to BSC at $t_0 = 0.1$ s (Event1), BSC to STSMC at $t_1 = 1.1$ s (Event2), STSMC to MPC at $t_2 = 2.1$ s (Event3).

7.2.1. CASE I: STEP CHANGE OF ACTIVE POWER

The rating active power of MMC3 is set to 1000 MW (1 p.u.). MMC1 maintains the DC grid voltage and acts like a slack bus in the DC grid, MMC2 supplies active power from wind farms, while MMC3 regulates the active power flow. Before the disturbance, the reference active power $P_{ac,ref}$ of MMC3 is set as 0 p.u. The power produced by the wind farms through MMC2 is all absorbed by MMC1. At time instance $t_0 = 0.1$ s, there is a step change in the $P_{ac,ref}$ of MMC3 rising from 0 p.u. to 0.5 p.u. (Event1). Different controller combinations (7.1) present different behaviors to this system transient. Figure 7.2 provides the simulation results of the active power exchanges between MMC1 and MMC3.

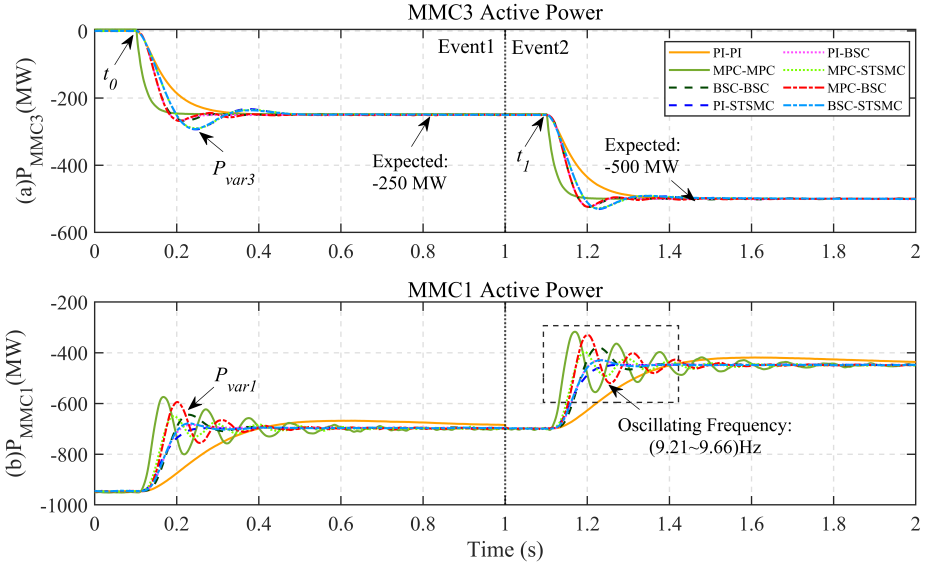

Figure 7.2: Simulation of case I: (a) MMC3 active power. (b) MMC1 active power.

According to Figure 7.2(a), the waveform of P_{MMC3} is smooth and does not oscillate in the case of scenario PI-PI (S1). However, the speed of response and settling is significantly slower than the other scenarios due to the higher time constant of PI control in the outer loop. In contrast to S1, the scenario MPC-MPC (S2) has the optimal performance of the rising and settling time and minimal power variation (almost none). In the case of scenario BSC-BSC (S3), the converge time is shorter than in scenario S1, and a small degree of variation can be found. This is because the reference signal of i_d^{Δ} of BSC comes from the upper-level energy controller, which is designed to reflect the variations of DC

voltage. Thus, the tracking ability of active power step-changing is relatively weak. When the MMC3 is controlled via STSMC (S4), a large degree of variation is observed, since the STSMC is turned to provide faster response as a consequence creates overshoot. A similar result is also found in S8. For other controller allocations, the settling and rise time are reduced compared with scenario PI-PI (S1), and the power variations are also smaller than in scenarios S4, S6, and S8.

Figure 7.2(b) presents the waveform of MMC1 active power, the scenario PI-PI (S1) presents an even longer rise and settling time than that of MMC3. The MMC 3 absorbs the power from the DC grid. However, the response of MMC 1's outer control is slower (in the case of S1). The energy is taken from the DC voltage, which creates a drop in DC voltage. Thus, the tracking ability of MMC1 is not robust enough against active power step change. In the case of scenarios S2, S6, and S7, the active power P_{MMC1} is converging with an oscillating frequency (from 9.21 Hz to 9.66 Hz) as a result of interaction between inner and outer control loops. Other scenarios are similar to that of MMC3. The transient process of Event2 is similar to that found in Event1.

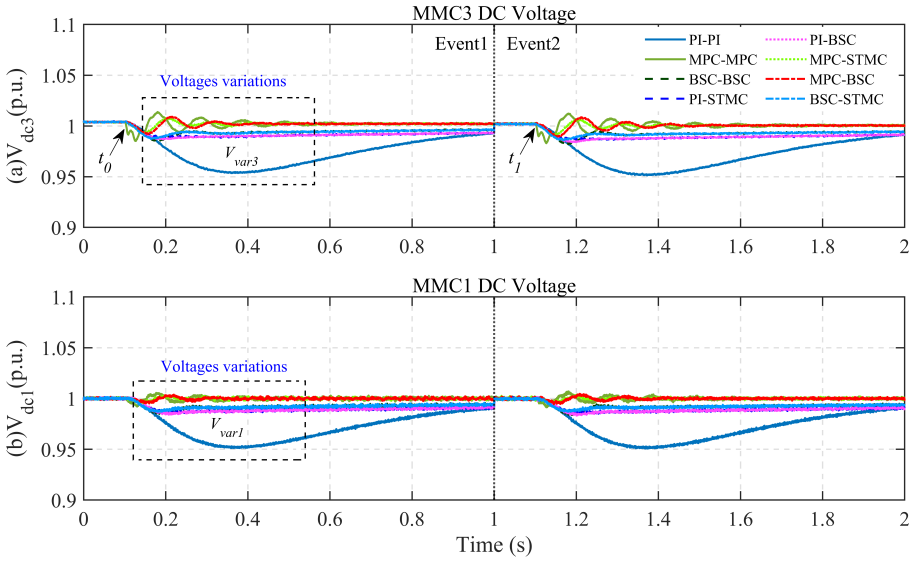

Figure 7.3: Simulation of case I: (a) MMC3 DC voltage. (b) MMC1 DC voltage.

The dynamics of active power also lead to variations in DC voltage. Figure 7.3 provides the simulation for DC voltages V_{dc3} and V_{dc1}. The maximum percentage variation in the DC voltage varies with different controller allocations. It is obvious that in the case of scenario PI-PI (S1), the voltage V_{dc3} and V_{dc1} have the largest voltage variations which exceed the error band, and the settling time both at MMC3 and MMC1 is longer than that of other scenarios by reason of the high time constant settling in MMC3 PI outer loop. In contrast, small fluctuations are observed in some control scenarios, e.g., S2, S6, and S7, but can be restricted within a 3 % standard margin. For other controller allocations, e,g., S3, S5, and S8, the waveforms of V_{dc3} and V_{dc1} are smooth and without any oscillations. Overall, these scenarios with advanced controllers present a more desirable

performance than that of classical controller allocation S1.

Table. 7.2 provides the detailed summary statistics obtained from the preliminary analysis of case I. It is apparent that the rise time t_r of S1 in case of P_{MMC3} and P_{MMC1} are much longer than in other scenarios by cause of MMC1's DC voltage control settling. But except for S2, the variation of P_{MMC3} in S1 is much smaller than in all other scenarios due to its smooth process. While for some scenarios, e.g., S4, S6, and S8, they are designed with a fast-tracking capability, which improves the rise time but in the meantime, it causes significant fluctuations due to the excessive damping during transients. This further prolongs the settling time which is even longer than S1. This phenomenon also applies and is even more obvious for the in P_{MMC1} of MMC1. For the DC voltage variations, the S1 has the largest variations, which reach 4.88 % and 4.92 %, respectively. Other scenarios have optimal performance in maintaining the DC voltage, the fluctuations are restricted within the margin of 2 %, among them the S6 obtains the optimal behavior with 0.85 % and 0.49 % variations at each side. Scenario S4 (PI-STSMC) is suggested as the optimal choice to regulate the active power, since it has minimal power and voltage variations, and the fastest rise and settling time, S5 (PI-BSC) and S8 (BSC-STSMC) can be set as the back-up scenarios.

Table 7.2: Simulation data for case I.

Item	Event1							
	P_{MMC3}			P_{MMC1}			V_{dc3}	V_{dc1}
	t_r(s)	t_s(s)	P_{var3}(%)	t_r(s)	t_s(s)	P_{var1}(%)	V_{var3}(%)	V_{var1}(%)
S1	0.154	0.220	0.053	0.192	0.766	6.525	4.88	4.92
S2	0.050	0.079	0.012	0.039	0.381	29.191	1.70	0.86
S3	0.073	0.153	4.823	0.081	0.168	15.50	1.79	1.64
S4	0.089	0.339	6.070	0.083	0.112	0.49	1.36	1.49
S5	0.072	0.138	4.710	0.081	0.097	4.578	1.62	1.68
S6	0.088	0.347	5.529	0.061	0.201	11.472	0.85	0.49
S7	0.072	0.1323	4.768	0.065	0.229	26.353	1.06	0.67
S8	0.089	0.338	6.009	0.080	0.136	4.077	1.40	1.32

7.2.2. CASE II: DC FAULT AND DCCB RE-CLOSING

Figure 7.4 provides diagrams that represent successful fault interruption in cable12. The term iline12 used in Figure 7.4(a) refers to the line current, and the term iosc12 is defined as a high-frequency oscillating current of the VSC-branch of VARC DCCB to create the zero-crossing. Since the PTG fault is applied at t_0 = 0.1 s at the cable12 outlet, the protection immediately detects the fault and trips the VARC DCCB installed at the positive pole of cable12 (near MMC1), while the DCCB near MMC2 is tripped with a time-delay due to the fault traveling wave propagation across the cable12.

As can be seen in Figure 7.4(a), the current iline12 continues to increase until iosc12 reaches the same amplitude (reversal direction) and is communicated to the main breaker. The peak value of fault current, in this case, is 19.96 kA. The fault is successfully interrupted at 0.1173 s. Meanwhile, the fault pole voltage is also cleared at 0.115 s, as found in Figure 7.4(b). We assume that the fault is a temporary fault, the VARC DCCB is initialed at

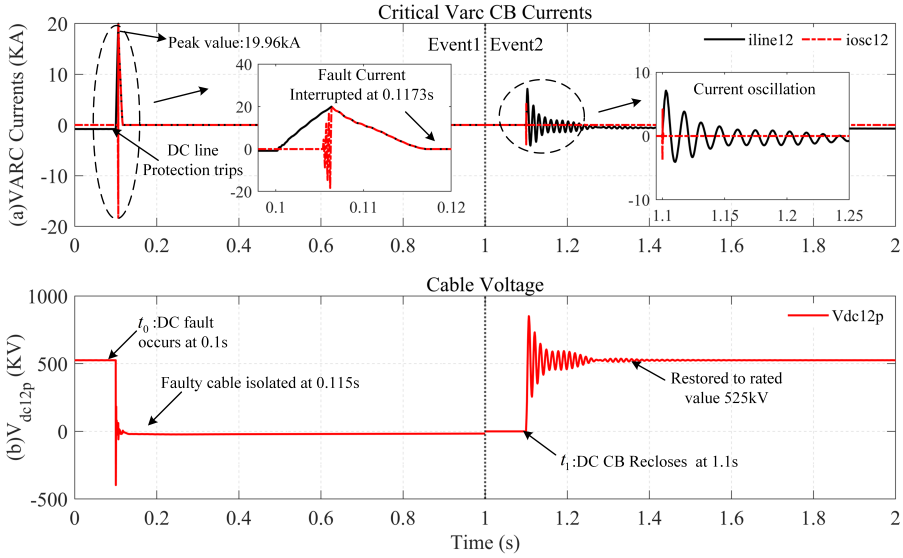

Figure 7.4: Simulation of case II: (a) VARC currents. (b) Cable12 voltage.

t_1 = 1.1 s to reconnect the cable12. It is revealed that both cable current and pole voltage can be restored to a steady value after oscillations, which will propagate into other parts of the MTDC system. Thus, the optimal coordination between MMC controllers will be crucial in maintaining the system's stability.

Figure 7.5 provides the performance of MMC1 and MMC3 (MMC2 is minimally affected) with different scenarios during the two events described in case II. Initially, the system operates at rated values. Since the DC fault is one of the most serious faults in the MTDC system, it is seen in Figure 7.5(a) that the voltage V_{dc1} of MMC1 in all scenarios suffers severe oscillations. However, it is worth mentioning that all the scenarios can restore the DC voltage quickly except for S1 due to the low response ability of DC voltage control. Similar results are also observable when the VARC DCCB is re-closed at t_1 = 1.1 s. The MMC1's output current i_{MMC1} is depicted in Figure 7.5(b). At the initial fault stage, the i_{MMC1} also increases rapidly. The majority of fault currents are the discharging currents of MMC arm capacitors. Different scenarios demonstrate different fault current suppression capabilities, the fault peak current ranges from 14.36 kA to 16.53 kA, and the current will be restored to nominal value when DCCB clears the fault. When the DCCB is re-closed at t_1 = 1.1 s (Event2), the topology of the system is modified, and the power flow is reallocated, which can be learned from Figure 7.5(b) and (c). Thus, the current i_{MMC1} will be restored to the new steady-state value with an oscillating frequency of 80.80 Hz. This newly added cable introduces a time delay due to the inductive nature of the cable. As a result, the time response of all scenarios varies within a range of a few milliseconds, the settling time t_s, in this case, is around 120 ms. The peak value is restricted to the range from 5.10 kA to 6.29 kA. As can be seen in Figure 7.5(c), the MMC3's active power P_{MMC3} is also highly affected at fault initial and post-fault stage.

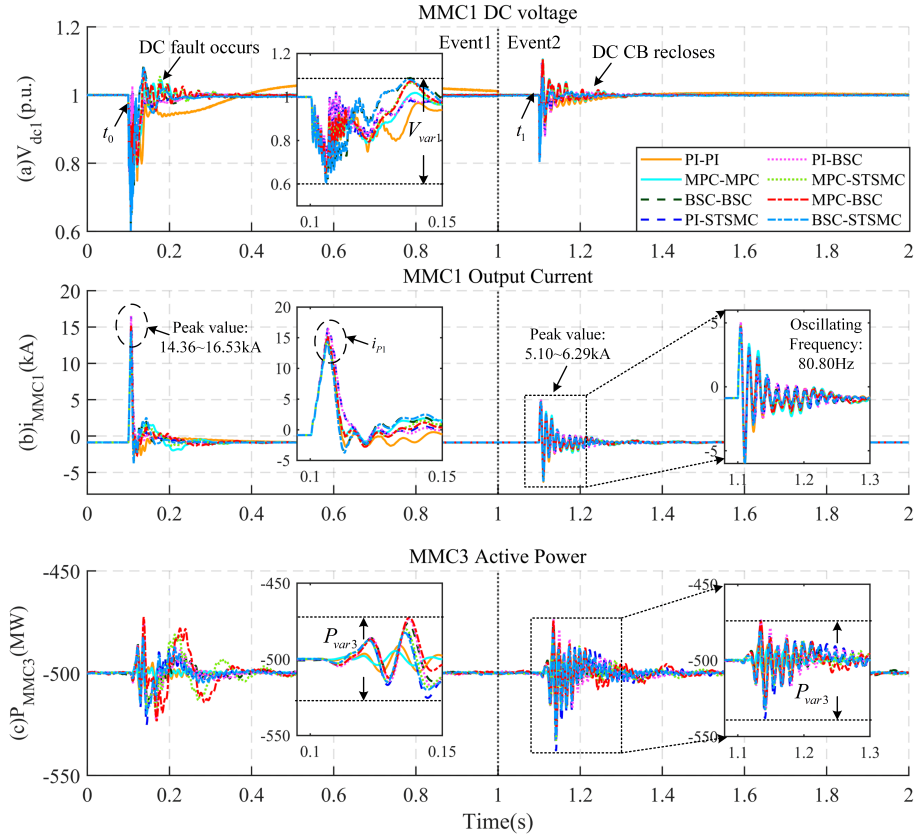

Figure 7.5: Simulation of case II:(a) MMC1 DC voltage. (b) MMC1 output current. (c) MMC3 active power.

The maximum variations and settling times vary in different scenarios. A detailed summary obtained from case II can be found in Table.7.3. In Event1, the voltage variation V_{var1} for all scenarios exceeded 30 %. Among them, S3 and S8 have the largest value of 39.72 % and 39.80 %, respectively, and V_{var1} with S4 and S5 are relatively small at 30.16 % and 30.14 %, respectively. However, the S4 and S5 present large power variations P_{var3} in Event2. In contrast, the current peak value i_{P1} of S3 and S8 are suppressed to the minimum values of 14.3679 kA and 14.4106 kA, respectively. While the S4 and S5 present the lowest current suppression capability. This is due to a higher drop in the DC voltage at MMC 1 as seen in Table. 7.3. What can be seen in this table of Event2 is that the combination of the advanced and classical controller does not provide any improved performance compared to S1. All the scenarios fail to maintain the DC voltage V_{var1} of MMC1 when the DCCB is re-closed, as they all drop sharply by 19 %. The peak current i_{P1} of MMC1 is also much larger than the steady-state value, although there is a degree of variation between different scenarios. For the active power of P_{MMC3}, the S1 and S2 present relatively minimal variations, which are 2.2135 % and 1.3563 %, respectively. The

optimal scenario selection against DC fault depends on the control priority. In the fault interruption stage (Event1). If the aim is to suppress the fault current, S3 (BSC-BSC) can be selected as it has the minimal peak value of i_{P1} as 14.3679 kA, and S8 (BSC-STSMC) can be set as the back-up scenario. If the aim is to maintain the DC voltage V_{dc1}, then S5 (PI-BSC) is the optimal settling as it has the minimal variation $V_{var1} = 30.14\%$. S4 (PI-STSMC) can be set as the backup scenario. S2 (MPC-MPC) is the first choice if the aim is to maintain the active power flow of the MMC3 side, and S1 (PI-PI) can be the backup choice. In the DCCB re-closing stage, S2 is the optimal settling as it has the desired performance both in suppressing the oscillating current and maintaining the active power flow at MMC3.

Table 7.3: Simulation data for case II

Item	Event1			Event2		
	V_{dc1}	i_{MMC1}	P_{MMC3}	V_{dc1}	i_{MMC1}	P_{MMC3}
	V_{var3}(%)	i_{P1}(kA)	P_{var3}(%)	V_{var3}(%)	i_{P1}(kA)	P_{var3}(%)
S1	36.51	15.0043	1.642	19.25	-6.2930	2.214
S2	35.25	15.1715	0.799	19.21	-5.1433	1.356
S3	39.72	14.3679	3.088	19.51	-6.1568	5.287
S4	30.16	16.5320	5.059	19.03	-5.2855	7.615
S5	30.14	16.5279	4.572	19.08	-5.2514	6.574
S6	35.2	15.1746	4.076	19.29	-5.1863	6.614
S7	35.14	15.1803	4.676	19.39	-5.1015	5.427
S8	39.80	14.4106	4.009	19.60	-6.2426	6.453

7.2.3. CASE III: WIND-SPEED CHANGE

The active power P_{MMC2} depends on the wind speed of wind turbines. Figure. 7.6 provides the waveforms of active power in different scenarios for case III.

Initially, all output active powers remain steady. Assuming that the wind speed is changed at the time instance $t_0 = 0.5$ s, the active power generated by wind farm P_{MMC2} starts to increase. Since the MMC2 is independently controlled via the grid-forming PI controller, the transient of P_{MMC2} is not affected by the controller allocations of MMC1 and MMC2. According to Figure 7.6(a), the P_{MMC2} increase smoothly to the preset new condition 750 MW, the rise time t_r and settling time t_s are 0.51 s and 0.74 s, respectively. The overshoots or undershoots of P_{MMC2} are not observed during this transient. Similar results are also found in Event2. As for the P_{MMC1} presented in Figure 7.6 (b), all the scenarios with advanced controllers have optimal performance except for the scenario PI-PI (S1). S1 has the longest settling time t_s and the power variation is also observable. This longer power variation is created as the outer control loop of MMC1 and it is associated with DC voltage variations. It is not sensitive to the power flow changing of the DC grid. While for the P_{MMC3} depicted in Figure 7.6 (c), it is seen that P_{MMC3} remain the steady steady value, only minor fluctuations can be seen. The constant power flow in MMC3 is due to the nature of the control mode i.e. P/Q control. However, the small perturbation arises caused by the variation of DC grid voltage around the operating point.

Detailed data of rise and settling time of active power P_{MMC1} are listed in Table.7.4. What stands out in this table is that the settling time t_s of scenario S1 for events 1 and 2

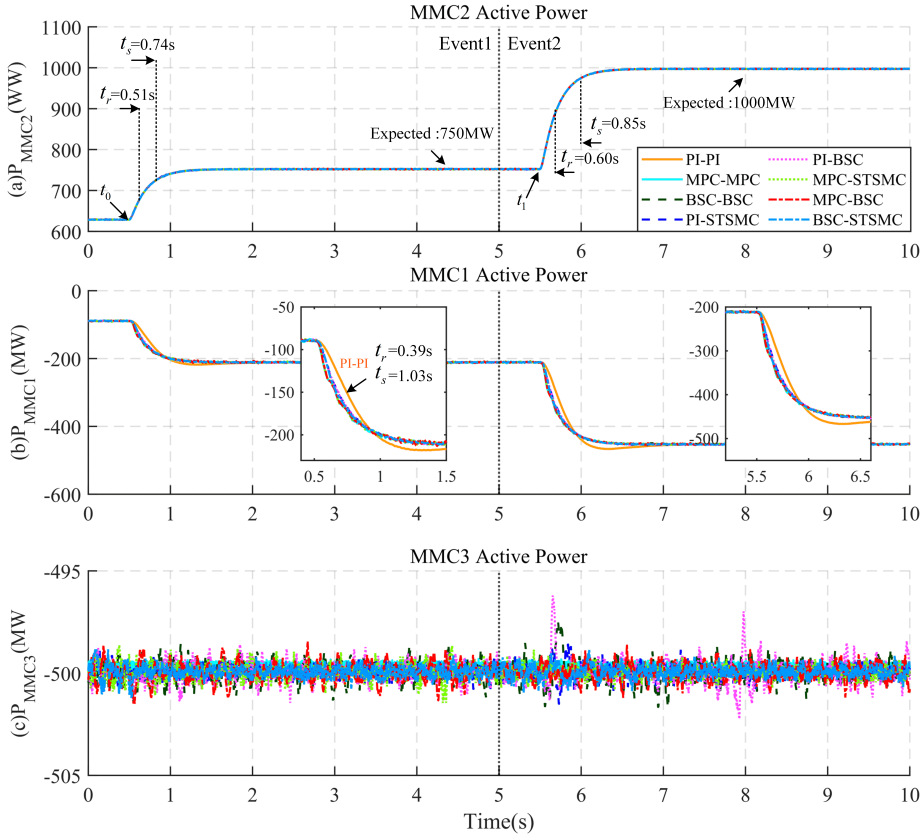

Figure 7.6: Simulation of case III: (a) MMC2 active power. (b) MMC1 active power. (c) MMC3 active power.

are 1.0376 s and 0.9147 s, respectively, which are the longest. The results are aligned with preliminary analysis and also demonstrate the superior performance of these advanced controllers in terms of tracking signals. It is concluded that S2 (MPC-MPC) is the optimal choice for regulating the active power flow, since it requires a minimal settling time to achieve the pre-set value, S3 (BSC-BSC) and S4 (PI-STSMC) can be the backup scenarios. Other scenarios also have desirable performance except for S1.

7.2.4. CASE IV: AC FAULT STUDY

The single phase to ground fault is the most common fault in the AC grid. Figure 7.7 reveals the effect of case IV on MMC1's outputs. The initial conditions are the same as in the previous subsections. After the fault occurs at $t_0 = 0.1$ s, the oscillations of MMC outputs are perceptible in all scenarios. Recall that MMC1 adopts the V_{dc}/V_{ac} control mode. An AC gird fault can be considered as a sudden disturbance signal imposed to v_{ac}. Therefore, the $i^{\Sigma}_{q,ref}$ of the outer control loop will change abruptly, which leads to the sudden change of v^{Σ}_{Mq} of the inner loop. Besides, the v^{G}_{d} and v^{G}_{q} and the frequency

Table 7.4: Simulation data for case III

Item	Event1		Event2	
	P_{MMC1}		P_{MMC1}	
	$t_r(s)$	$t_s(s)$	$t_r(s)$	$t_s(s)$
S1	0.3929	1.0376	0.4975	0.9147
S2	0.3600	0.5665	0.5731	0.5726
S3	0.3643	0.5856	0.5734	0.5730
S4	0.3724	0.5793	0.5878	0.5873
S5	0.3691	0.5820	0.5949	0.5944
S6	0.3587	0.6493	0.5713	0.5996
S7	0.3466	0.6400	0.5938	0.6122
S8	0.3620	0.5928	0.5896	0.5891

as the output of PLL are also affected by the fault. As a result, the inputs of the capacitor voltage balancing controller and firing control of MMC1 will be disturbed. Eventually, the DC side outputs of MMC1 fluctuate.

More precisely, the MMC1's DC voltage is depicted in Figure 7.7(a), the impact of AC fault on V_{dc1} is much smaller than that of a DC fault in any scenario, as illustrated in Figure 7.5(a). This is because the variation of V_{dc1} is mainly affected by the voltage variation on the DC side. Figure 7.7(b) depicts waveform of the MMC1's output current i_{MMC1}. Since i_{MMC1} represents the sum of the upper and lower arm currents of MMC1, the AC fault will cause the sudden change of the grid current $i^{\Delta}_{a,b,c}$ and disrupt the balance of MMC1's arm currents. As a result, the circulating currents $i^{\Sigma}_{a,b,c}$ will increase rapidly (almost zero in the steady state) until the disappearance of the AC fault. Then, the i_{MMC1} gradually restores to the steady-state value. The oscillations of i_{MMC1} caused by AC fault are much smaller than that of DC fault as depicted in Figure 7.5(b), since V_{dc1}, in this case, remains stable, the SMs capacitors are not discharged after the fault. Similar results of P_{MMC1} can be found in Figure 7.7(c) as it is the product of V_{dc1} and i_{MMC1}. In addition, it is worth mentioning that the second-order harmonics will appear in the DC components since the PLL can not isolate the asymmetrical positive and negative sequence components contained in the AC grid voltages and currents by the single phase to ground fault.

The variations and settling times of case IV are summarized in Table. 7.5. It is visible that all the scenarios present desirable performance in maintaining the DC voltage V_{dc1}, the largest variation of V_{var1} is only 0.0072 % (S1). For the output current i_{MMC1}, the amplitude in steady-state is 0.887 kA. After the fault, the transient peak value i_{P1} is restricted to 0.9469 kA (S3). The oscillations of fault current in i_{MMC1} are suppressed to the steady-state value within 0.55 s for any scenario, which confirms the indispensability of the CCSC loop of each controller. For the active power P_{MMC1}, it is seen that it exceeds the ±3% error band only in the scenarios S1, S6, and S8. The largest variation of P_{var1} is 3.4047 % and it is settled after 0.2968 s, other two scenarios stabilize the P_{MMC1} after 0.0746 s and 0.0785 s, respectively. The statistics fully demonstrate the robustness of each scenario against the AC grid fault. The system stability is guaranteed. It is con-

cluded that the S2 (MPC-MPC) and S5 (PI-BSC) are the optimal scenarios against AC grid fault since they have minimal settling time to restore the system to the original steady state. Other scenarios present slower settling times or larger active power variations at MMC1.

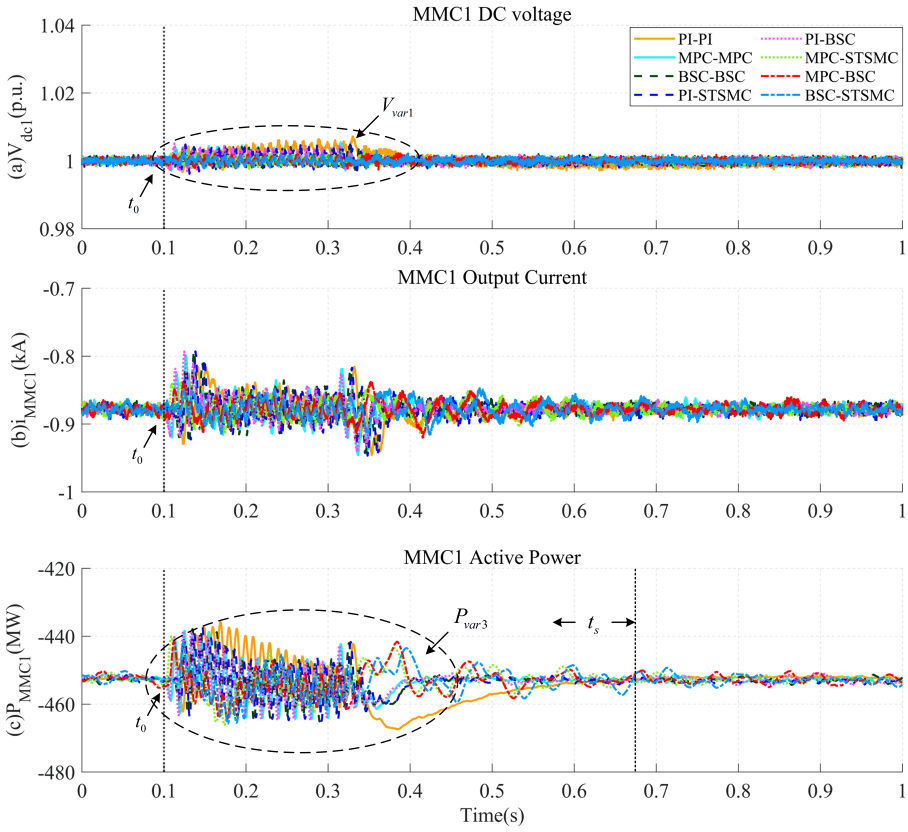

Figure 7.7: Simulation of case IV: (a) MMC1 DC Voltage. (b) MMC1 output current. (c) MMC1 active power.

7.2.5. CASE V: SWITCHING BETWEEN DIFFERENT CONTROLLERS

Figure 7.8 illustrates the transition effect between different controllers of MMC1. PI control is the initial control method as it is the most commonly utilized method in practical projects. The change in MMC1 control from PI to BSC is applied at the time instance t_0 = 0.1 s. It is seen in Figure 7.8, that the DC outputs of MMC1 and MMC3 remain steady, and only a small variation of P_{var1} (2.16 %) is observed in P_{MMC1}, which reveals that switching between PI and BSC can be realized smoothly and without bringing extra oscillations to the system. In the case of the controller switching from BSC to MPC (Event2) at t_1 = 1.1 s, there is an oscillation of 56.49 Hz with an overshoot of 4.63 % in DC link voltage V_{dc1}. This oscillation occurs due to the mismatch between the output of the inner current controllers. During the operation of BSC, the MPC output is saturated.

Table 7.5: Simulation data for case IV

Item	Event1				
	V_{dc1}	i_{MMC1}		P_{MMC1}	
	V_{var1}(%)	i_{P1}(kA)	t_s(s)	P_{var1}(%)	t_s(s)
S1	0.0072	0.9456	0.2914	3.4047	0.2968
S2	0.0055	0.9458	0.1606	2.7570	-
S3	0.0048	0.9469	0.1719	2.9288	-
S4	0.0053	0.9466	0.4679	2.8643	-
S5	0.0051	0.9410	0.1610	2.8217	-
S6	0.0026	0.9130	0.3363	3.1214	0.0746
S7	0.0026	0.9210	0.3353	2.7503	-
S8	0.0030	0.9164	0.5500	3.0438	0.0785

Upon the transition, the saturated value of MPC control is applied to the MMC1. As a result, MMC1 injects less power into the DC grid, which further increases the DC link voltage V_{dc1}. Later, the outer DC voltage controller regulates this voltage mismatch and restores the system.

Furthermore, Figure 7.9 illustrates the effect of transitions between different controllers implemented in MMC3. The switching from PI to BSC is applied at $t_0 = 0.1$ s, and all the DC voltages of MMC1 and MMC3 remain steady. When the control switches form BSC to STSMC at $t_1 = 1.1$ s, small fluctuations are visible at V_{dc1} and V_{dc3}, which reach to 1.21 % and 0.54 %, respectively. This is caused by the saturation of the control signal in opposite polarity, which leads to power overshoots and further creates DC link voltage overshoots. Similarly, the output currents i_{MMC1} and i_{MMC3} are also affected, with peak values of -1.0319 kA and -1.027 kA, respectively. Since extra power is taken from the DC grid at MMC2, a power mismatch of the STSMC controller affects the P_{MMC3}, and the variation P_{var3} reaches 60.0 %. When the controller switches from STSMC to MPC at $t_2 = 2.1$ s (Event2), it is found in Figure 7.9(a) that DC voltage V_{dc3} is oscillating with the 136.61 Hz due to the faster action of MPC and slower response of STSMC, the oscillations are restored to steady-state at 2.273 s, the maximum variation of V_{var3} is restricted to 2.05 %. Since the control action takes place at MMC3 with limited power variation, the V_{dc1} remains constant. The oscillating behaviors of currents i_{MMC1} and i_{MMC3} are similar to that of DC voltages, the peak values during this transient reach -1.30 kA and -1.175 kA, respectively. While for the active power presented at Figure 7.9(c), small variations are found in P_{MMC1} and P_{MMC3}, the P_{var3} reaches to 10.1 %, which is larger than P_{var1} (6.24 %) due to higher voltage oscillations.

The results of this investigation show that all classical and advanced controllers implemented in MMC1 and MMC3 can switch between each other. Although there are some undesired fluctuations on the DC side in some scenarios, most are within the acceptable 3 % error band. More prominent disturbances are quickly adjusted to steady-state values by the controller and will not cause excessive disturbances to the entire MTDC system.

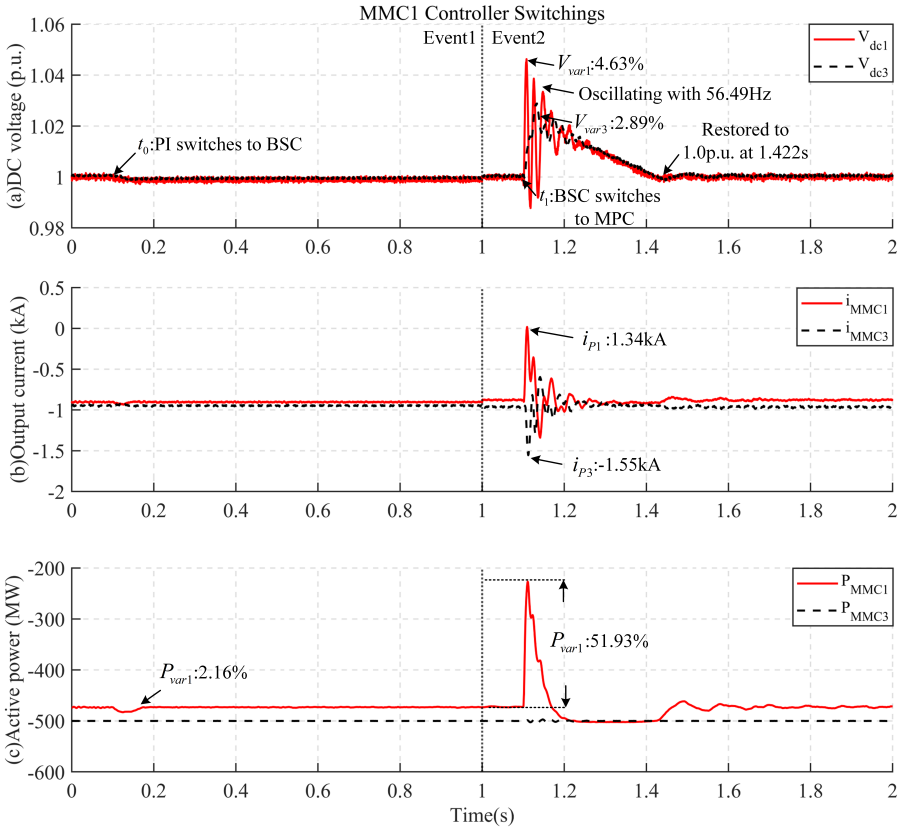

Figure 7.8: Simulation of case V: (a) DC voltage. (b) Output current. (c) Active power.

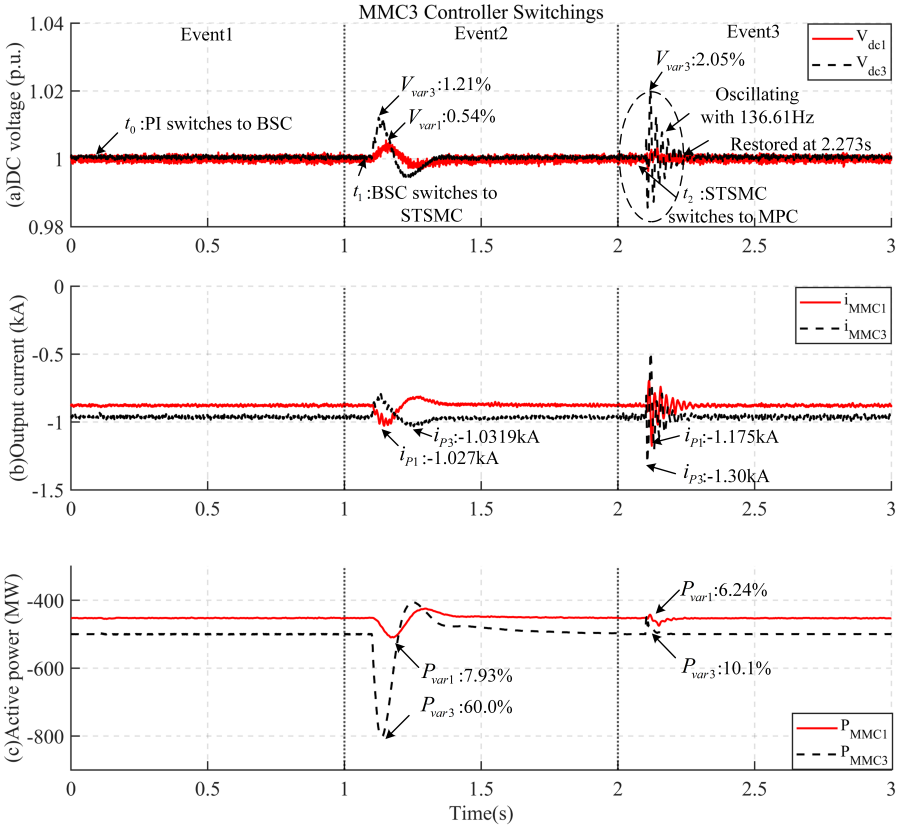

Figure 7.9: Simulation of case V: (a) DC voltage. (b) Output current. (c) Active power.

7.3. CONCLUSION

This Chapter investigates the interoperability between the classical PI controller and non-linear MPC, BSC, and STSMC controllers during large transients of future MTDC systems. The interoperability investigation was conducted for eight MMC controller allocation scenarios. The five common system transient cases, such as step change of active power, DC/AC grid faults, wind speed changing, and controller switching, are defined to study the performance of the predefined controller allocation scenarios in the RTDS environment. Each case is thoroughly investigated through the settling time, rise time, and maximum active power and voltage variations. According to the findings, the scenarios with non-linear MMC controllers generally show better transient performance by achieving faster settling time and fewer DC voltage and active power variations than classical PI MMC controllers.

The insights from the results may assist in establishing the optimal controller allocation under each system oscillation scenario. On the whole, the findings of this study have many important implications for constructing multi-vendor MTDC systems in practice.

8

CONCLUSIONS AND SUGGESTIONS FOR FUTURE WORK

This chapter summarizes the conclusions of the thesis and provides the answers to the research questions. Besides, a few suggestions for future research are also discussed.

The final chapter contains two parts. Section 8.1 provides the meaningful answers to the **key research questions** asked in Chapter I, along with the findings and conclusions. Section 8.2 discusses potential research directions for the future to expand the work further, offering more promising and attractive solutions for future practical MTDC applications.

The main topics within the thesis are **MMC control & interoperability, Protection, and Fault location** for the MMC-based MTDC system. The research conducted in previous chapters aims to address the shortcomings and limitations of existing works, providing promising technical solutions for future MTDC systems. The scientific contributions can be summarized into threefold. Specifically,

1. A DWT-based robust DC protection scheme for the MTDC system.
2. A parameter fitting-based fault location method for the MTDC system.
3. Modeling of nonlinear control methods for MMCs and the control interoperability test for the MTDC system.

The presented methods and studies accomplished the research objectives and answered the proposed key research questions. The answers are detailed as follows.

8.1. ANSWERS TO THE RESEARCH QUESTIONS

Q1: What are the strategies to achieve control interoperability in the MTDC grid, considering vendor-specific control systems? Additionally, how can these strategies be evaluated and optimized for overall grid performance and stability?

To investigate control interoperability in the future vendor-specific MTDC grids, this thesis deals with the modeling of the classic PI controller and three non-linear controllers: backstepping control, sliding mode control, and model predictive control for MMCs in a three-terminal MTDC system. Various control allocation scenarios and system transient cases are conducted in the RTDS environment to evaluate the performance of each scenario. Key indicators, like rise time, settling time, active power, and voltage variations, are used to assess the controller performance for maintaining grid stability. The detailed controller modeling process and MMC control interoperability are discussed in Chapters III and VII, respectively.

The RTDS simulations in Chapter VII demonstrated that the MMC non-linear controllers achieve faster transitions with minimal DC voltage and active power variations during the system transients. Taking Case I (step change of active power) as an example, the waveform of the DC active power is smooth and does oscillate when the PI controllers are used. However, the speed of the active power response and settling is much slower than those in non-linear controllers-based scenarios. For the DC voltage variations originating from active power changes, the DC voltages have the largest voltage variations with PI controllers, which exceed the error band. The settling time of the MMCs with PI controllers is longer than that of other scenarios. In contrast, only small fluctuations are observed in the scenarios with non-linear controllers and can be restricted within a 3% standard margin. According to the results, these scenarios with non-linear controllers present a more desirable performance than those of classical PI controllers. The optimal and backup choices regulate the active power to obtain

a faster response, and minimal variations can be determined. Similar conclusions can be drawn for other tested transient cases, such as DC fault and DCCB reclosing, wind-speed change, and AC grid faults. Besides, the classical and nonlinear controllers can switch between each other. While minor fluctuations arise in some scenarios, most remain within the acceptable ranges. Addressing these concerns will be a future work.

Given that these large disturbances can be quickly regulated to a steady state without causing excessive disturbances to the entire MTDC system, these insights could pave the way for optimal controller allocations in terms of various system oscillation scenarios. All these findings in Chapter VII demonstrate that interoperable non-linear MMC controllers have a promising perspective in enhancing resilience and response speed without causing significant fluctuations to the future multi-vendors MTDC system.

Q2: How can we develop robust protection schemes to detect DC faults promptly, and how can we ensure their selectivity, sensitivity, and reliability?

In the MTDC system, there are multiple DC lines. If any DC line has a fault, the stable operation of other healthy DC lines, as well as components like MMCs, will be severely affected. The degree of impact depends on factors like the DC fault type, fault location, duration of fault, fault resistance, and other considerations. To coordinate with the DCCB to immediately interrupt the fault current and isolate the faulty line, the DC line protection must promptly determine the faulty line and fault types.

Chapter IV analyzes the features of TWs in the MTDC system. Applying the *Perterson* equivalent circuit and the simplified MMC models, the expressions for the fault-induced current and voltage TWs are derived both in *S*-and time-domain. By constructing the transfer function, the features of measured TWs in internal and external relays are obtained. It is found that due to the existence of boundary element, the magnitude of the high-frequency components of the line-mode voltage TWs measured at the faulty line is significantly greater than that of the healthy line. Similar phenomena are also captured in the faulty pole- and healthy pole voltages. As a result, the fault area and fault type can be determined using the features of the high-frequency components contained in the measured voltages TWs.

Based on the findings in Chapter IV, Chapter V proposes a DWT-based protection scheme. The results demonstrated the robustness of the proposed protection from the perspectives of "Speed," "Selectivity," "Sensitivity," and "Reliability."

In conclusion, achieving a balance in the robustness of protection performance is always a trade-off, especially considering the four key factors. However, by utilizing the appropriate characteristics of fault-induced signals for protection design and by setting the threshold values accurately, one can design protection that meets desired levels of speed, selectivity, sensitivity, and reliability. The proposed protection improves the performance in terms of "selectivity," "sensitivity," and "reliability", compared to existing protection methods. The thresholds can be easily determined, and as such, the proposed protection can be easily applied to other testing models and actual systems. Some efforts are still needed to improve this protection work further in the future, which will be discussed later.

Q3: Which methodology can be used to develop accurate and refined fault loca-

tors?

In this thesis, a novel parameter fitting-based fault location method is proposed, which provides a fresh perspective on the fault location for the MTDC systems.

According to the TW theory, the TWs initiated at the fault point can be divided into two parts: the backward TWs and the forward TWs. The direction of the forward traveling waves is from the DC bus to the cable. In contrast, the direction of the backward traveling waves is from the cable to the DC bus. Both the expressions of the backward TWs and the forward TWs contain the fault location information. Since the wavefront of backward traveling waves measured at relays are not refracted or reflected by the line boundaries, the analytical expressions of their waveforms are closer to those in practical engineering. To this end, Chapter VI extends the fault analysis theory of the MTDC system, and the expressions for the backward line-mode current TWs are derived using the simplified *Peterson* equivalent fault circuit. It is revealed that the time domain expression for the line-mode backward TWs comprises two parts: a constant value and an exponential function. Specifically, the coefficient contained in the exponential function is associated with the fault location. Thus, if the value of the coefficient can be determined, the fault location can be estimated. This concept formulates the motivation for the proposed fault location method.

To obtain the value of parameters from sampled discrete data, Chapter VI utilizes the non-linear parameter fitting to verify the analytical expressions of backward TWs and to fit the discrete data from the protection measurements. The fitting process can be regarded as a nonlinear least squares optimization problem. The AMLM algorithm is introduced in detail for fitting the optimal parameters. The data from both relay units of faulty cables are used to determine the fault location. Here, it is noticed that the proposed method is a single-ended method. It does not need communication devices and channels to exchange and synchronize the measuring data, which significantly reduces the hardware requirements and investment in practical applications. After numerous simulation tests in PSCAD and RTDS, it is concluded that the proposed parameter fitting algorithm and fault location method are accurate, with most fault location errors being smaller than 0.5%. The proposed method is independent of fault types and the size of the DC inductor and has desirable performance with various sampling frequencies. The method is also accurate for severe noise disturbance. To implement the proposed fault location method in other MTDC systems, it is necessary to determine suitable initial values and the data window length for parameter fitting. In conclusion, the proposed fault location method is novel, accurate, and promising for the MTDC system.

Compared to other parameter fitting algorithms, such as Newton's method and the classical LM algorithm, the adopted AMLM algorithm has better computational accuracy, fewer iteration steps, and fewer memory sizes. Compared to the classical TWs-based fault location method, the proposed method does not need an extremely high sampling frequency to detect the refraction/reflection time of TWs and the exact information of TW velocity. Compared to the active injection-based fault location method, the proposed one does not require additional measurements or a signal injection device. The fault location can be realized with offline sampled data.

The key benefit of this method is that the parameter used is a system parameter that is solely determined by the frequency-dependent (phase) cable model. As a result, if

the exact expression of measured TWs can be derived and an accurate parameter fitting algorithm is employed, the precise fault location can be estimated. Moreover, the fault location results are minimally affected by the fault type and the DC inductor size, which can not be achieved using other fault location methods.

In the future, continuous efforts are still needed to improve this fault location method performance further, and the application in other systems and a few work directions will be discussed later.

8.2. RECOMMENDATIONS FOR FUTURE RESEARCH

Based on the studies of this thesis, several recommendations can be proposed for future research to develop and improve our understanding of HVDC protection, fault location, and interoperable MMC control for MTDC power systems:

1. Formulating the adaptive protection thresholds

   The threshold values of protection methods directly determine the "Speed," "Selectivity," "Sensitivity," and "Reliability." of the protection. The thresholds introduced in Chapter V are set to fixed values by considering the pre-defined conditions to ensure the "Selectivity," "Sensitivity," and "Reliability." For example, the most serious noise disturbance is considered as 25 dB, and the maximum fault resistance is considered as 500 Ω. However, in actual MTDC systems, DC faults can occur in any manner, and their specific fault conditions are entirely unpredictable, including the fault type, fault location, grounding resistance, and fault duration. Besides, system disturbances, such as DCCB reclosing, converter station operational mode changes, and system topology changes, can also impact threshold selection. The protection might malfunction in these cases. Therefore, protection schemes with fixed threshold values have significant limitations. Some future work is needed to find the optimal threshold value settings to continue improving the sensitivity and selectivity performance. Establish the communications between the relays and other components and formulate the threshold values adaptive to all possible fault conditions and system oscillations. Using a predefined looking-up table might be a promising solution.

2. Developing new time-frequency signal analysis algorithms to overcome sampling frequency limitations.

   The proposed protection method in Chapter V utilizes the features of high-frequency components contained in the measured TWs. The DWT is selected as the signal-analyzing tool due to its merits of being computationally efficient in time-frequency analysis and its high computational speed. A sampling frequency of 100 kHz is used in the DWT. As such, the detection speed of the protection is very fast, and its selectivity is guaranteed. Though some commercial protection devices use extremely high sampling frequencies (1 MHz), e.g., SEL-T401L and SEL-TWFL, most practical protections adopt a sampling frequency of 10 kHz. This poses significant challenges when using advanced time-frequency analyzing tools like DWT to formulate protections. Consequently, the time-frequency resolution of these

tools would be significantly reduced, and the time delays would increase. For instance, the time delay in the thesis caused by DWT is 0.05 ms when the sampling frequency is 100 kHz, but it becomes 0.5 ms if the sampling frequency is 10 kHz. This can significantly affect the robustness performance of the protection. Similar problems will also arise for other methods, such as HHT and *S*-transform. To enhance the practical implementation ability, a novel time-frequency analyzing tool may be developed to address the low sampling frequency limitation and maintain robust protection performance for abrupt signal detection.

3. Investigating other possibilities of the DC inductor L_{dc}

   For most MTDC protection methods, such as time-domain-based protections and inductor-voltage-based protection methods, L_{dc} is critical and indispensable. In the proposed protection method, L_{dc}, with a value of 120 mH, serves as a boundary device to filter out the high-frequency components found in the TWs. As a result, these high-frequency components are detected only in the faulty cable relays, ensuring protection selectivity. However, L_{dc} requires significant land space in offshore HVDC grids with submarine cable transmissions, especially when it has a large value. How can we refine the DC protection methods (especially the thresholds) using a smaller value of L_{dc} or different installation locations of L_{dc}? Developing non-boundary protection and fault location methods for the MTDC system without the use of L_{dc} would also be an interesting and promising topic for future research study.

4. Refining the optimal data window for parameter fitting

   The proposed fault location method in Chapter VI utilized the parameters fitted from the sampled TWs data to estimate the fault location. When fitting these parameters, two factors are critical in determining the accuracy between fitted results and measured data. The first is the adopted algorithm, which outlines the detailed iterative processes and the convergence level, helping identify optimal parameters. The second is the data selected for parameter fitting, which is discussed in Chapter VI. The data selected from the backward line-mode current TWs stems from the TWs that arrive at the relays and peak with a short time delay of 50 μs. This data window selects the data from the sampled TWs and feeds the input to the AMLM algorithm. It can be regarded as a fixed data window length and suits most of the fault conditions. However, in specific extreme cases, such as noise interference, data window selection should be adaptive. It might also require anti-noise filtering functionalities to provide the AMLM algorithm with the original sampled TWs data. Otherwise, the fitted data might deviate from their theoretical TWs expressions, resulting in inaccurate fault location estimations. Hence, refining the principle of data window selection for parameter fitting is essential to enhance fault location performance.

5. Implementing the protection and fault location method in the overhead line (OHL) transmission system

   In this thesis, the submarine transmission line in the testing MTDC system is modeled using the frequency-dependent (phase) model in PSCAD and RSCAD. This

simulates the MTDC system developed and planned in the North Sea. However, the OHL is another option for other MTDC projects, especially for these onshore long-distance MTDC projects. The physical features between the cable lines and OHL are different. For example, the OHL usually has higher reactance and lower capacitance than cables. The TWs velocity in OHL is also higher than that of cables. Therefore, the TWs propagation process on a faulty OHL varies from cable lines in the post-fault stage. For example, since the voltage drops more quickly and the current rises more rapidly in OHL compared to cable models, the usable data for protection design at the same sampling frequency is much less in OHL than in cable. This presents significant challenges for protection and for ensuring the accuracy of fault location methods. In addition, the features of the high-frequency components contained in the TWs and *S*-and time-domain expressions of the TWs defined in this thesis should be studied further. Given these distant properties concerning TWs, the protection and fault location method must be adjusted accordingly or reformulated.

On the other hand, the permanent HIF, such as a tree falling and making contact with the line, is a more common fault type in OHL. This poses a challenge for the fault location method. In Chapter VI, all faults are considered metallic since the cable model is used in the testing system. However, the fault resistance is associated with the magnitude of voltage TWs. As a result, the fitted values will also be influenced by the fault resistance, even with the same fault location. This could pose a problem if the proposed AMLM-based fault location is directly implemented in OHL-based MTDC systems.

Moreover, the DC faults discussed in this thesis are limited to PTG, NTG, and PTP faults, which occur in submarine cables. However, the phenomenon of lightning strikes has not been considered in the design of protection and fault location methods. The adopted *Peterson* fault circuit may not suit the lightning strikes on the OHL system to analyze the fault-induced TWs. Lightning strikes also present challenges for protection relays, such as the sampling frequency detection speed and accuracy of the wavefront of TWs. Therefore, it is essential to refine the proposed protection and fault location methods for implementing OHL-based MTDC systems.

6. Refining the MMC control interoperability study

   The MMC control interoperability study in this thesis is original and is in the beginning stage. The findings have obtained many important implications for the multi-vendor MTDC systems. However, a lot of work is still needed in the future. Firstly, in Case V, undesired power oscillations and fluctuations were observed when the controller switched between different controllers. Further investigation is needed to understand the reasons behind this phenomenon and to eliminate it. Then, the interactions of different controller allocations are analyzed mainly based on the RTDS experimental results. Research on the mathematical mechanism behind the results when the MTDC system operates with interacted controllers is needed for further study. Besides, the broadband oscillation in the MTDC system is closely related to the controls, parameter tuning, and controller

interactions. The solution using these non-linear control technologies is needed to mitigate these undesired broadband oscillations and improve the stability and power quality in multi-vendor MTDC systems. Finally, the tested controllers are applied in a decentralized manner. In the future, a centralized layer of MMC controllers with both traditional and advanced controllers for the MTDC system could be developed by properly setting all operating points (reference values). This study may provide a new perspective for further developing these nonlinear controllers and testing the interoperability of MMC.

BIBLIOGRAPHY

[1] A. Alassi, S. Bañales, O. Ellabban, G. Adam, and C. MacIver, "Hvdc transmission: Technology review, market trends and future outlook", *Renewable and Sustainable Energy Reviews*, vol. 112, pp. 530–554, 2019, ISSN: 1364-0321.

[2] M. Liserre, T. Sauter, and J. Y. Hung, "Future energy systems: Integrating renewable energy sources into the smart power grid through industrial electronics", *IEEE Industrial Electronics Magazine*, vol. 4, no. 1, pp. 18–37, 2010. DOI: 10.1109/MIE.2010.935861.

[3] Y. Xue and X.-P. Zhang, "Reactive power and ac voltage control of lcc hvdc system with controllable capacitors", *IEEE Transactions on Power Systems*, vol. 32, no. 1, pp. 753–764, 2017. DOI: 10.1109/TPWRS.2016.2557342.

[4] ABB. "Evolution of HVDC light". (2028), [Online]. Available: https://new.abb.com/news/detail/4224/evolution-of-hvdc-lightr (visited on 07/28/2023).

[5] T. Halder, "Hot modeling and simulation of high voltage direct current (hvdc) power transmission", in *2012 IEEE International Conference on Power Electronics, Drives and Energy Systems (PEDES)*, 2012, pp. 1–6. DOI: 10.1109/PEDES.2012.6484496.

[6] ABB, "Special Report 60 years of HVDC-ABB", Tech. Rep. July, 2023.

[7] A. Kalair, N. Abas, and N. Khan, "Comparative study of hvac and hvdc transmission systems", *Renewable and Sustainable Energy Reviews*, vol. 59, pp. 1653–1675, 2016, ISSN: 1364-0321.

[8] C. Srivastava and M. Tripathy, "Dc microgrid protection issues and schemes: A critical review", *Renewable and Sustainable Energy Reviews*, vol. 151, p. 111 546, 2021, ISSN: 1364-0321.

[9] N. M. Haleem, A. D. Rajapakse, A. M. Gole, and I. T. Fernando, "Investigation of fault ride-through capability of hybrid vsc-lcc multi-terminal hvdc transmission systems", *IEEE Transactions on Power Delivery*, vol. 34, no. 1, pp. 241–250, 2019. DOI: 10.1109/TPWRD.2018.2868467.

[10] H. Zheng, X. Yuan, J. Cai, P. Sun, and L. Zhou, "Large-signal stability analysis of dc side of vsc-hvdc system based on estimation of domain of attraction", *IEEE Transactions on Power Systems*, vol. 37, no. 5, pp. 3630–3641, 2022. DOI: 10.1109/TPWRS.2022.3144336.

[11] WIKIPEDIA. "List of HVDC projects". (2023), [Online]. Available: https://en.wikipedia.org/wiki/List_of_HVDC_projects#Europe (visited on 07/31/2023).

[12] Tennet. "Our projects". (2023), [Online]. Available: https://www.tennet.eu/projects (visited on 07/14/2023).

[13] North Sea Wind Power Hub Programme, "Unlocking the North Sea as a Green Powerplant", Tech. Rep. September, 2022. DOI: https://northseawindpowerhub.eu/knowledge/unlocking-the-north-sea-as-a-green-powerplant.

[14] Entsoe. "TYNDP 2022 Projects Sheets". (2023), [Online]. Available: https://tyndp.entsoe.eu/european-projects (visited on 07/14/2023).

[15] W. Wang, X. Yan, S. Li, L. Zhang, J. Ouyang, and X. Ni, "Failure of submarine cables used in high-voltage power transmission: Characteristics, mechanisms, key issues and prospects", *IET Generation, Transmission & Distribution*, vol. 15, no. 9, pp. 1387–1402, 2021.

[16] S. Gao, Q. Liu, and G. Song, "Current differential protection principle of hvdc transmission system", *IET Generation, Transmission & Distribution*, vol. 11, no. 5, pp. 1286–1292, 2017.

[17] T. G. Bolandi, H. Seyedi, S. M. Hashemi, and P. S. Nezhad, "Impedance-differential protection: A new approach to transmission-line pilot protection", *IEEE Transactions on Power Delivery*, vol. 30, no. 6, pp. 2510–2518, Dec. 2015.

[18] L. Chen, X. Lin, Z. Li, *et al.*, "Similarity comparison based high-speed pilot protection for transmission line", *IEEE Transactions on Power Delivery*, vol. 33, no. 2, pp. 938–948, Apr. 2018.

[19] J. Sneath and A. D. Rajapakse, "Fault detection and interruption in an earthed hvdc grid using rocov and hybrid dc breakers", *IEEE Transactions on Power Delivery*, vol. 31, no. 3, pp. 973–981, 2014.

[20] J. Liu, N. Tai, and C. Fan, "Transient-voltage-based protection scheme for dc line faults in the multiterminal vsc-hvdc system", *IEEE Transactions on Power Delivery*, vol. 32, no. 3, pp. 1483–1494, 2016.

[21] W. Leterme, J. Beerten, and D. Van Hertem, "Nonunit protection of hvdc grids with inductive dc cable termination", *IEEE Transactions on Power Delivery*, vol. 31, no. 2, pp. 820–828, 2015.

[22] C. Zhang, J. Huang, G. Song, and X. Dong, "Non-unit ultra-high-speed line protection for multi-terminal hybrid lcc/mmc hvdc system and its application research", *IEEE Transactions on Power Delivery*, vol. 36, no. 5, pp. 2825–2838, Oct. 2021.

[23] R. Li, L. Xu, and L. Yao, "Dc fault detection and location in meshed multiterminal hvdc systems based on dc reactor voltage change rate", *IEEE Transactions on Power Delivery*, vol. 32, no. 3, pp. 1516–1526, Jun. 2017.

[24] C. Li, A. M. Gole, and C. Zhao, "A fast dc fault detection method using dc reactor voltages in hvdc grids", *IEEE Transactions on Power Delivery*, vol. 33, no. 5, pp. 2254–2264, Oct. 2018.

[25] W. Xiang, S. Yang, G. P. Adam, H. Zhang, W. Zuo, and J. Wen, "Dc fault protection algorithms of mmc-hvdc grids: Fault analysis, methodologies, experimental validations, and future trends", *IEEE Transactions on Power Electronics*, vol. 36, no. 10, pp. 11 245–11 264, 2021.

[26] S. Yang, W. Xiang, R. Li, X. Lu, W. Zuo, and J. Wen, "An improved dc fault protection algorithm for mmc hvdc grids based on modal-domain analysis", *IEEE Journal of Emerging and Selected Topics in Power Electronics*, vol. 8, no. 4, pp. 4086–4099, 2019.

[27] K. Satpathi, Y. M. Yeap, A. Ukil, and N. Geddada, "Short-time fourier transform based transient analysis of vsc interfaced point-to-point dc system", *IEEE Transactions on Industrial Electronics*, vol. 65, no. 5, pp. 4080–4091, May 2018.

[28] Z. Zheng, T. Tai, J. S. Thorp, and Y. Yang, "A transient harmonic current protection scheme for hvdc transmission line", *IEEE Transactions on Power Delivery*, vol. 27, no. 4, pp. 2278–2285, Oct. 2012.

[29] D. Li, A. Ukil, K. Satpathi, and Y. M. Yeap, "Improved s transform-based fault detection method in voltage source converter interfaced dc system", *IEEE Transactions on Industrial Electronics*, vol. 68, no. 6, pp. 5024–5035, 2020.

[30] V. A. Lacerda, R. M. Monaro, D. Campos-Gaona, D. V. Coury, and O. Anaya-Lara, "Distance protection algorithm for multiterminal hvdc systems using the hilbert–huang transform", *IET Generation, Transmission & Distribution*, vol. 14, no. 15, pp. 3022–3032, 2020.

[31] D. Wang and M. Hou, "Travelling wave fault location algorithm for lcc-mmc-mtdc hybrid transmission system based on hilbert-huang transform", *International Journal of Electrical Power & Energy Systems*, vol. 121, p. 106 125, 2020.

[32] O. M. K. K. Nanayakkara, A. D. Rajapakse, and R. Wachal, "Traveling-wave-based line fault location in star-connected multiterminal hvdc systems", *IEEE Transactions on Power Delivery*, vol. 27, no. 4, pp. 2286–2294, 2012.

[33] S. Zhang, G. Zou, C. Wang, J. Li, and B. Xu, "A non-unit boundary protection of dc line for mmc-mtdc grids", *International Journal of Electrical Power & Energy Systems*, vol. 116, p. 105 538, 2020.

[34] B. Li, Y. Li, J. He, *et al.*, "An improved transient traveling-wave based direction criterion for multi-terminal hvdc grid", *IEEE Transactions on Power Delivery*, vol. 35, no. 5, pp. 2517–2529, Oct. 2020.

[35] W. Xiang, S. Yang, L. Xu, J. Zhang, W. Lin, and J. Wen, "A transient voltage-based dc fault line protection scheme for mmc-based dc grid embedding dc breakers", *IEEE Transactions on Power Delivery*, vol. 34, no. 1, pp. 334–345, 2018.

[36] L. Liu, Z. Liu, M. Popov, P. Palensky, and M. A. M. M. van der Meijden, "A fast protection of multi-terminal hvdc system based on transient signal detection", *IEEE Transactions on Power Delivery*, vol. 36, no. 1, pp. 43–51, 2021.

[37] S. S. Mirhosseini, S. Jamali, and M. Popov, "Non-unit protection method for long transmission lines in mtdc grids", *IET Generation, Transmission & Distribution*, vol. 15, no. 11, pp. 1674–1687, 2021.

[38] Z.-Y. He, K. Liao, X.-P. Li, S. Lin, J.-W. Yang, and R.-K. Mai, "Natural frequency-based line fault location in hvdc lines", *IEEE transactions on power delivery*, vol. 29, no. 2, pp. 851–859, 2013.

[39] G. Song, X. Chu, X. Cai, S. Gao, and M. Ran, "A fault-location method for vsc-hvdc transmission lines based on natural frequency of current", *International Journal of Electrical Power & Energy Systems*, vol. 63, pp. 347–352, 2014.

[40] J. He, B. Li, Q. Sun, *et al.*, "The improved fault location method based on natural frequency in mmc-hvdc grid by combining fft and music algorithms", *International Journal of Electrical Power & Energy Systems*, vol. 137, p. 107 816, 2022.

[41] G. Song, J. Hou, B. Guo, T. Wang, B. Masood, and S. T. H. Kazmi, "Single-ended active injection for fault location in hybrid mmc-hvdc systems", *International Journal of Electrical Power & Energy Systems*, vol. 124, p. 106 344, 2021.

[42] T. Bi, S. Wang, and K. Jia, "Single pole-to-ground fault location method for mmc-hvdc system using active pulse", *IET Generation, Transmission & Distribution*, vol. 12, no. 2, pp. 272–278, 2018.

[43] T. Wang, G. Song, and K. S. T. Hussain, "Adaptive single-pole auto-reclosing scheme for hybrid mmc-hvdc systems", *IEEE Transactions on power delivery*, vol. 34, no. 6, pp. 2194–2203, 2019.

[44] D. Li and A. Ukil, "Fault location estimation in voltage-source-converter-based dc system: The *L* location", *IEEE Transactions on Industrial Electronics*, vol. 69, no. 11, pp. 11 198–11 209, 2022.

[45] J. Xu, Y. lü, C. Zhao, and J. Liang, "A model-based dc fault location scheme for multi-terminal mmc-hvdc systems using a simplified transmission line representation", *IEEE Transactions on Power Delivery*, vol. 35, no. 1, pp. 386–395, 2020.

[46] L. Yuansheng, W. Gang, and L. Haifeng, "Time-domain fault-location method on hvdc transmission lines under unsynchronized two-end measurement and uncertain line parameters", *IEEE Transactions on Power delivery*, vol. 30, no. 3, pp. 1031–1038, 2015.

[47] S. Lan, M.-J. Chen, and D.-Y. Chen, "A novel hvdc double-terminal non-synchronous fault location method based on convolutional neural network", *IEEE Transactions on Power Delivery*, vol. 34, no. 3, pp. 848–857, 2019.

[48] C. Zhang, G. Song, T. Wang, and L. Yang, "Single-ended traveling wave fault location method in dc transmission line based on wave front information", *IEEE Transactions on Power Delivery*, vol. 34, no. 5, pp. 2028–2038, 2019.

[49] M. Farshad and M. Karimi, "A signal segmentation approach to identify incident/reflected traveling waves for fault location in half-bridge mmc-hvdc grids", *IEEE Transactions on Instrumentation and Measurement*, vol. 71, pp. 1–9, 2022.

[50] J. Suonan, S. Gao, G. Song, Z. Jiao, and X. Kang, "A novel fault-location method for hvdc transmission lines", *IEEE Transactions on Power Delivery*, vol. 25, no. 2, pp. 1203–1209, 2010.

[51] J. Wang and Y. Zhang, "Traveling wave propagation characteristic-based lcc-mmc hybrid hvdc transmission line fault location method", *IEEE Transactions on Power Delivery*, vol. 37, no. 1, pp. 208–218, 2022. DOI: 10.1109/TPWRD.2021.3055840.

[52] InterOPERA. "Objectives Mutually Compatible HVDC systems". (2023), [Online]. Available: https://interopera.eu/objectives/ (visited on 07/27/2023).

[53] L. Liu, A. Shetgaonkar, and A. Lekić, "Interoperability of classical and advanced controllers in mmc based mtdc power system", *International Journal of Electrical Power & Energy Systems*, vol. 148, p. 108 980, 2023.

[54] G. Bergna-Diaz, J. Freytes, X. Guillaud, S. D'Arco, and J. A. Suul, "Generalized voltage-based state-space modeling of modular multilevel converters with constant equilibrium in steady state", *IEEE Journal of Emerging and Selected Topics in Power Electronics*, vol. 6, no. 2, pp. 707–725, 2018.

[55] A. Shetgaonkar, A. Lekić, J. L. Rueda Torres, and P. Palensky, "Microsecond enhanced indirect model predictive control for dynamic power management in mmc units", *Energies*, vol. 14, no. 11, 2021, ISSN: 1996-1073.

[56] P. Karamanakos, E. Liegmann, T. Geyer, and R. Kennel, "Model predictive control of power electronic systems: Methods, results, and challenges", *IEEE Open Journal of Industry Applications*, vol. 1, pp. 95–114, 2020.

[57] P. McNamara and F. Milano, "Model predictive control-based agc for multi-terminal hvdc-connected ac grids", *IEEE Transactions on Power Systems*, vol. 33, no. 1, pp. 1036–1048, 2018.

[58] J.-W. Moon, J.-S. Gwon, J.-W. Park, D.-W. Kang, and J.-M. Kim, "Model predictive control with a reduced number of considered states in a modular multilevel converter for hvdc system", *IEEE Transactions on Power Delivery*, vol. 30, no. 2, pp. 608–617, 2015.

[59] M. Ahmadijokani, M. Mehrasa, M. Sleiman, M. Sharifzadeh, A. Sheikholeslami, and K. Al-Haddad, "A back-stepping control method for modular multilevel converters", *IEEE Transactions on Industrial Electronics*, vol. 68, no. 1, pp. 443–453, 2021.

[60] Y. Jin, Q. Xiao, H. Jia, *et al.*, "A dual-layer back-stepping control method for lyapunov stability in modular multilevel converter based statcom", *IEEE Transactions on Industrial Electronics*, vol. 69, no. 3, pp. 2166–2179, 2022.

[61] Z. Liu, S. Xie, and Y. Kang, "Disturbance-tracking-based backstepping control for vsc-hvdc systems with mismatched uncertainties", in *2020 12th IEEE PES Asia-Pacific Power and Energy Engineering Conference (APPEEC)*, 2020, pp. 1–5.

[62] X. Zhao and K. Li, "Adaptive backstepping droop controller design for multi-terminal high-voltage direct current systems", *IET Generation, Transmission & Distribution*, vol. 9, no. 10, pp. 975–983, 2015.

[63] R. Sadeghi, S. M. Madani, M. Ataei, M. R. Agha Kashkooli, and S. Ademi, "Supertwisting sliding mode direct power control of a brushless doubly fed induction generator", *IEEE Transactions on Industrial Electronics*, vol. 65, no. 11, pp. 9147–9156, 2018.

[64] C. Lascu, A. Argeseanu, and F. Blaabjerg, "Supertwisting sliding-mode direct torque and flux control of induction machine drives", *IEEE Transactions on Power Electronics*, vol. 35, no. 5, pp. 5057–5065, 2020.

[65] P. Rault, O. Despouys, A. Petit, *et al.*, "Implementation of a dedicated control to limit adverse interaction in multi-vendor hvdc systems", in *15th IET International Conference on AC and DC Power Transmission (ACDC 2019)*, 2019, pp. 1–6.

[66] L. Liu, A. Lekić, and M. Popov, "Robust traveling wave-based protection scheme for multiterminal dc grids", *IEEE Transactions on Power Delivery*, vol. 38, no. 5, pp. 3117–3129, 2023. DOI: 10.1109/TPWRD.2023.3265748.

[67] C. Collados-Rodriguez, M. Cheah-Mane, F. Cifuentes-Garcia, *et al.*, "Integration of an mmc-hvdc link to the existing lcc-hvdc link in balearic islands based on grid-following and grid-forming operation", *IEEE Transactions on Power Delivery*, vol. 37, no. 6, pp. 5278–5288, 2022. DOI: 10.1109/TPWRD.2022.3175251.

[68] J. Dakic, M. Cheah-Mane, O. Gomis-Bellmunt, and E. Prieto-Araujo, "Hvac transmission system for offshore wind power plants including mid-cable reactive power compensation: Optimal design and comparison to vsc-hvdc transmission", *IEEE Transactions on Power Delivery*, vol. 36, no. 5, pp. 2814–2824, 2021. DOI: 10.1109/TPWRD.2020.3027356.

[69] J. Hu, H. Xu, and Y. He, "Coordinated control of dfig's rsc and gsc under generalized unbalanced and distorted grid voltage conditions", *IEEE Transactions on Industrial Electronics*, vol. 60, no. 7, pp. 2808–2819, 2013. DOI: 10.1109/TIE.2012.2217718.

[70] K. Ni, Y. Hu, D. T. Lagos, G. Chen, Z. Wang, and X. Li, "Highly reliable back-to-back power converter without redundant bridge arm for doubly fed induction generator-based wind turbine", *IEEE Transactions on Industry Applications*, vol. 55, no. 3, pp. 3024–3036, 2019. DOI: 10.1109/TIA.2019.2892925.

[71] R. Cardenas, R. Pena, S. Alepuz, and G. Asher, "Overview of control systems for the operation of dfigs in wind energy applications", *IEEE Transactions on Industrial Electronics*, vol. 60, no. 7, pp. 2776–2798, 2013. DOI: 10.1109/TIE.2013.2243372.

[72] S. Ali, Z. Ling, K. Tian, and Z. Huang, "Recent advancements in submodule topologies and applications of mmc", *IEEE Journal of Emerging and Selected Topics in Power Electronics*, vol. 9, no. 3, pp. 3407–3435, 2021. DOI: 10.1109/JESTPE.2020.2990689.

[73] O. C. Sakinci and J. Beerten, "Generalized dynamic phasor modeling of the mmc for small-signal stability analysis", *IEEE Transactions on Power Delivery*, vol. 34, no. 3, pp. 991–1000, 2019.

[74] Ö. C. Sakinci, A. Lekić, and J. Beerten, "Generalized impedance-based ac/dc power system modeling for harmonic stability analysis", *International Journal of Electrical Power & Energy Systems*, vol. 143, p. 108 456, 2022, ISSN: 0142-0615.

[75] W. G. Cigré, "B4. 57."Guide for the Development of Models for HVDC Converters in a HVDC Grid"", *CIGRE Technical Brochure*, vol. 604, 2014.

[76] R. Wachal, A. Jindal, S. Dennetiere, and H. Saad, *HVDC Converters in a HVDC Grid*. 2014, ISBN: 9782858733057.

[77] S. Liu and M. Popov, "Development of hvdc system-level mechanical circuit breaker model", *International Journal of Electrical Power & Energy Systems*, vol. 103, pp. 159–167, 2018.

[78] S. Liu, M. Popov, S. S. Mirhosseini, *et al.*, "Modeling, experimental validation, and application of varc hvdc circuit breakers", *IEEE Transactions on Power Delivery*, vol. 35, no. 3, pp. 1515–1526, 2020.

[79] K. Sano and M. Takasaki, "A surgeless solid-state dc circuit breaker for voltage-source-converter-based hvdc systems", *IEEE Transactions on Industry Applications*, vol. 50, no. 4, pp. 2690–2699, 2014. DOI: 10.1109/TIA.2013.2293819.

[80] X. Han, W. Sima, M. Yang, L. Li, T. Yuan, and Y. Si, "Transient characteristics under ground and short-circuit faults in a ±500 kV mmc-based hvdc system with hybrid dc circuit breakers", *IEEE Transactions on Power Delivery*, vol. 33, no. 3, pp. 1378–1387, 2018. DOI: 10.1109/TPWRD.2018.2795800.

[81] S. Liu, Z. Liu, J. de Jesus Chavez, and M. Popov, "Mechanical dc circuit breaker model for real time simulations", *International Journal of Electrical Power & Energy Systems*, vol. 107, pp. 110–119, 2019, ISSN: 0142-0615.

[82] S. S. Mirhosseini, S. Liu, J. C. Muro, Z. Liu, S. Jamali, and M. Popov, "Modeling a voltage source converter assisted resonant current dc breaker for real time studies", *International Journal of Electrical Power & Energy Systems*, vol. 117, p. 105 678, 2020, ISSN: 0142-0615.

[83] L. Ängquist, A. Baudoin, S. Norrga, S. Nee, and T. Modeer, "Low-cost ultra-fast dc circuit-breaker: Power electronics integrated with mechanical switchgear", in *2018 IEEE International Conference on Industrial Technology (ICIT)*, 2018, pp. 1708–1713. DOI: 10.1109/ICIT.2018.8352439.

[84] PROMOTioN. "Task 6.8 Develop roadmap for VARC DC CB scaling to EHV DC voltage". (2019), [Online]. Available: https://www.promotion-offshore.net/fileadmin/PDFs/D6.8_Developing_roadmap_for_VARC_DCCB_TUD_SCiBREAK_TenneT.pdf (visited on 07/25/2023).

[85] H. Ye, W. Pei, L. Kong, and T. An, "Low-order response modeling for wind farm-mtdc participating in primary frequency controls", *IEEE Transactions on Power Systems*, vol. 34, no. 2, pp. 942–952, 2019. DOI: 10.1109/TPWRS.2018.2874042.

[86] L. Liu, A. Lekić, and M. Popov, "Robust adaptive back-stepping control approach using quadratic lyapunov functions for mmc-based hvdc digital twins", in *International Symposium on Leveraging Applications of Formal Methods*, Springer, 2022, pp. 126–138.

[87] R. E. Kalman and J. E. Bertram, "Control system analysis and design via the "second method" of lyapunov: I—continuous-time systems", 1960.

[88] E. Davison and E. Kurak, "A computational method for determining quadratic lyapunov functions for non-linear systems", *Automatica*, vol. 7, no. 5, pp. 627–636, 1971, ISSN: 0005-1098.

[89] T. Kadota and H. Bourne, "Stability conditions of pulse-width-modulated systems through the second method of lyapunov", *IRE Transactions on Automatic Control*, vol. 6, no. 3, pp. 266–276, 1961.

[90] T. Hu and Z. Lin, "Composite quadratic lyapunov functions for constrained control systems", *IEEE Transactions on Automatic Control*, vol. 48, no. 3, pp. 440–450, 2003.

[91] M. M. Peet and A. Papachristodoulou, "A converse sum of squares lyapunov result with a degree bound", *IEEE Transactions on Automatic Control*, vol. 57, no. 9, pp. 2281–2293, 2012.

[92] M. M. Peet, "Exponentially stable nonlinear systems have polynomial lyapunov functions on bounded regions", *IEEE Transactions on Automatic Control*, vol. 54, no. 5, pp. 979–987, 2009.

[93] M. Aghahadi, L. Piegari, A. Lekić, and A. Shetgaonkar, "Sliding mode control of the mmc-based power system", in *IECON 2022 – 48th Annual Conference of the IEEE Industrial Electronics Society*, 2022, pp. 1–6.

[94] J. Stojković, A. Lekić, and P. Stefanov, "Adaptive control of hvdc links for frequency stability enhancement in low-inertia systems", *Energies*, vol. 13, no. 23, 2020.

[95] A. Shetgaonkar, L. Liu, A. Lekić, M. Popov, and P. Palensky, "Model predictive control and protection of mmc-based mtdc power systems", *International Journal of Electrical Power & Energy Systems*, vol. 146, p. 108 710, 2023.

[96] L. Wang, *Model predictive control system design and implementation using MATLAB®*. Springer Science & Business Media, 2009.

[97] L. Liu, F. Xie, M. Popov, Z. Hao, and A. Lekić, "Single-ended dc fault location method for mmc-based hvdc power system using adaptive multi-step levenberg-marquardt algorithm", in *2023 IEEE Belgrade PowerTech*, 2023, pp. 1–6.

[98] CIGRE Working Group B4.76, "DC-DC converters in HVDC grids and for connections to HVDC systems", Tech. Rep. March, 2021, pp. 1–196.

[99] C. Zhang, G. Song, A. S. Meliopoulos, and X. Dong, "Setting-less nonunit protection method for dc line faults in vsc-mtdc systems", *IEEE Transactions on Industrial Electronics*, vol. 69, no. 1, pp. 495–505, 2022.

[100] D. Mu, S. Lin, P. He, and X. Li, "An improved method of traveling wave protection for dc lines based on the compensation of line-mode fault voltage", *IEEE Transactions on Power Delivery*, vol. 38, no. 3, pp. 1720–1730, 2023. DOI: 10.1109/TPWRD.2022.3222375.

[101] F. Dai, D. Zeng, S. Liu, and G. Wang, "A practical impedance modeling method of mmc-hvdc transmission system for medium- and high-frequency resonance analysis", *Electric Power Systems Research*, vol. 212, p. 108 636, 2022, ISSN: 0378-7796.

[102] S. Yang, W. Xiang, and J. Wen, "An improved dc fault protection scheme independent of boundary components for mmc based hvdc grids", *IEEE Transactions on Power Delivery*, vol. 36, no. 4, pp. 2520–2531, 2020.

[103] C. Zhang, G. Song, T. Wang, L. Wu, and L. Yang, "Non-unit traveling wave protection of hvdc grids using levenberg–marquart optimal approximation", *IEEE Transactions on Power Delivery*, vol. 35, no. 5, pp. 2260–2271, 2020.

[104] F. Magnago and A. Abur, "Fault location using wavelets", *IEEE Transactions on Power Delivery*, vol. 13, no. 4, pp. 1475–1480, 1998. DOI: 10.1109/61.714808.

[105] A. Megahed, A. Moussa, and A. Bayoumy, "Usage of wavelet transform in the protection of series-compensated transmission lines", *IEEE Transactions on Power Delivery*, vol. 21, no. 3, pp. 1213–1221, 2006.

[106] C. Zhang, G. Song, T. Wang, and X. Dong, "An improved non-unit traveling wave protection method with adaptive threshold value and its application in hvdc grids", *IEEE Transactions on Power Delivery*, vol. 35, no. 4, pp. 1800–1811, 2020.

[107] L. Tang, X. Dong, S. Shi, and B. Wang, "Analysis of the characteristics of fault-induced travelling waves in mmc-hvdc grid", *The Journal of Engineering*, vol. 2018, no. 15, pp. 1349–1353, 2018.

[108] J. Fan, J. Huang, and J. Pan, "An adaptive multi step levenberg marquardt method", *Journal of Scientific Computing*, vol. 78, no. 1, pp. 531–548, 2019.

[109] C. Zhang, Y. Li, G. Song, and X. Dong, "Fast and sensitive nonunit protection method for hvdc grids using levenberg–marquardt algorithm", *IEEE Transactions on Industrial Electronics*, vol. 69, no. 9, pp. 9064–9074, 2021.

[110] RTDS Technologies Inc, "VSC small time-step turorial of RTDS user manuals", Tech. Rep., 2013, pp. 4–48.

[111] T. Maguire, B. Warkentin, Y. Chen, and J. Hasler, "Efficient techniques for real time simulation of mmc systems", in *Proc. Int. Conf. Power Syst. Transients (IPST)*, 2013, pp. 1–7.

[112] M. Matar, D. Paradis, and R. Iravani, "Real-time simulation of modular multilevel converters for controller hardware-in-the-loop testing", *IET Power Electronics*, vol. 9, no. 1, pp. 42–50, 2016.

[113] *Weather file*, https://weatherfile.com/, Accessed: 2021-12-08, 2022.

GLOSSARY

List of Abbreviations

AC	alternating current
AMLM	adaptive multi-step levenberg-marquardt
BTWs	backward TWs
BSC	back-stepping control
CCSC	circulating current suppression control
DC	direct current
DCCB	DC circuit breaker
DWT	discrete wavelet transform
DFIG	doubly-fed induction generators
EMD	empirical mode decomposition
FFT	fast fourier transform
FTWs	forward traveling waves
FPGA	field programmable gate array
GSC	grid side converter
HVDC	high voltage direct current
IGBT	insulated gate bipolar transistor
FB	full bridge
HB	half bridge
HIF	high impedance fault
HHT	hilbert huang transform
HVAC	high voltage alternating current
HIL	hardware-in-the-loop
IOP	interoperability
LM	levenberg-marquardt
LCC	line commutated converter
MMC	modular multilevel converter
MTDC	multi-terminal HVDC
MPC	model predictive control
NTG	negative pole-to-ground
OHL	overhead line
OGCC	output grid current control
pu	per unit

PI	proportional integral
PLL	phase locked loops
PTG	positive pole-to-ground
PTP	pole to pole
PCC	point of common coupling
PWM	pulse width modulation
RTDS	real time digital simulator
ROCOV	rate of change of voltage
ROTV	ratio of transient voltage
ROW	right of way
RSC	rotor side converter
SMC	sliding mode control
SM	sub-modular
SIL	software in the loop
STSMC	super-twisting sliding mode control
SFFT	short-time fourier transform
SNR	signal-noise-ratio
TWs	traveling waves
TWP	traveling wave protection
VSC	voltage source converter
VARC	VSC-assisted resonant current
WT	wavelet transform

ACKNOWLEDGEMENTS

Time flies like an arrow. The three-year journey I experienced while pursuing my Ph.D. at TU Delft make precious, memorable, and fulfilling time in my life. The scene of boarding the flight from Xi'an to the Netherlands is still clear in my mind as it was just yesterday. Completing my Ph.D. would not have been possible without the support and assistance of many people. I sincerely express my profound gratitude to everyone in the following remarks.

First of all, I would like to thank my promotor, Prof. Dr. Marjan Popov. My connection with Marjan began at the IEEE APAP conference in Xi'an in October 2019 when I served as a volunteer. During the conference, we had many inspired discussions, which motivated me to join TU Delft. The first year of my Ph.D. was particularly challenging as everyone was isolated at home and worked remotely due to COVID-19. In this tough period, Marjan showed great concern for my well-being. He would say, "Keep healthy, keep motivated," and everything will be fine. This consideration greatly reduced my stress, allowing me to maintain my physical and mental health. In the later stage of my Ph.D., when I felt anxious and pressured to publish papers, Marjan advised me to stay calm and focus on the quality of my research, which he considered more important than the quantity of publications. His strict but motivating way of work was challenging, so that all my papers, especially my final Ph.D. thesis, received prompt, critical, and inspired feedback. This greatly enhanced my academic writing and scientific skills, especially in our regular progress discussions on 'protection' topics, where Marjan's expertise was invaluable. These scientific discussions were not only greatly appreciated but also deeply enjoyed. When I felt stressed or lost, Marjan was there with timely, warm support and encouragement. Throughout the three-year collaboration with Marjan, I gradually clarified my academic goals. I evolved from feeling lost and helpless to becoming more firm and confident. What I gained was not just a Ph.D. degree but, more importantly, personal development, a clearer vision of my career, and the courage and confidence to face future challenges.

Next, I would like to convey my sincere gratitude to my daily supervisor/copromotor, Dr. Aleksandra, Lekić. When I first started my Ph.D. research, I was struggling with control theory. Aleksandra provided timely assistance with my control topic. She patiently explained the basics to me and sent me many references. This greatly boosted my academic research and extended my academic thinking, allowing me to finalize the Ph.D. thesis with protection and control interoperability. Aleksandra helped polish and revise all my papers and responses to reviewers' comments, providing many revision suggestions and enabling me to finish my tasks very fast. Besides, Aleksandra also offered much help in life, always advising me to relax, enjoy life, and release myself from work. I will always remember the relaxed and joyful times working and discussing with Aleksandra, and I am grateful for all the help, support, encouragement, and feedback from her.

Besides my supervisors, I would like to thank my Ph.D. committee members for their

nice discussion and insightful comments, which inspired me to finalize the Ph.D. thesis and my future research.

I would like to express my special thanks to my master's supervisor, Prof. Xiaoning Kang. I joined Prof. Kang's research group in September 2017. With Prof. Kang's recommendation, I was lucky to participate in the double master's degree program between Xi'an Jiaotong University and Politecnico Di Milano during 2017-2020. This year of overseas study in Milan has broadened my horizons and reshaped my mindset. This experience motivated me not to settle for a stable job but to seek out what I genuinely want to do — a meaningful and challenging job and career. During my Ph.D. studies in Delft, Prof. Kang provided me with a lot of support and advice for my career development. This was also a crucial source of motivation and belief when facing difficulties and challenges during my doctoral studies. I am deeply grateful for all the assistance Prof. Kang has given me over the past six years during my master's and doctoral studies!

Once again, I would like to thank my friend, Dr. Zongbo Li can truly be considered as a mentor and guide in my academic journey. Even though we are separated by thousands of miles and time zones, whenever I encounter problems or feel confused, Zongbo is the first person that comes to my mind. We often discuss numerous academic topics, such as how to write and publish papers, and how to seek academic positions. During our days working together in room 107 of the "Fadian" department, Zongbo always worked till late at night and was the last to leave. I still remember one late evening when I wanted to pursue a Ph.D. but was hesitant, fearing I couldn't complete the doctorate project. I jokingly asked Zongbo, "Do you think publishing two journals is very difficult?" Zongbo said no. The next day, I changed my mind and became firmer about the idea of pursuing a doctorate. Even today, I often joke with Zongbo, saying, if you had said, "It's very hard, I suggest you don't go for a Ph.D.," I might be working in a company now. In summary, I am deeply grateful for all the guidance and help that Zongbo has given. I sincerely wish Zongbo great success in his work, family, and life. I hope we can always walk on the path we desire and can continue to collaborate, promote, and support each other in the future in China.

Next, I would like to express my gratitude to my Chinese friends and IEPG colleagues, not only to Chenguang, Hu Ting, Aihui, Yuexiang, Lian Liu, Yuhan, Siyuan Liu, Na Li, Yigu Liu, Haiwei Xie, Shengren Hou, Haixiao Li, Dongyu Li, Fan Xie, Shuyi Gao, Shen Yan, Hongjin Du, Nan Lin, Weijie Xia, Dong Liu, Zhisheng Xiong but also to my friends Liqi Cao, Xueqing Miao, Yaqian Zhang, Xiao Hu, Cheng Chang, Cheng Liu, Fenghua Wang, Jing Xu, Jinke He, Li Wang, and Jianfeng Fu, for their invaluable contributions to my academic and life experiences. We experienced so many wonderful discussions and activities. Time always flies by, but all the memories will be unforgettable and cherished for a lifetime, becoming a part of my life as I continue to move forward. I am deeply grateful to and respectful of all the friendships, support, and precious memories I have gained with you in The Netherlands.

I would like to express my gratitude to my coauthors Ajay, Fan Xie, and Prof. Zhiguo Hao for the nice discussions and their invaluable contributions to our research. Their insights and expertise have greatly enhanced the quality of my Ph.D. research, and I am deeply grateful for their collaboration. I also want to thank my current IEPG staff members. Collaborating with individuals from diverse cultural backgrounds has expanded

my perspectives and enhanced my understanding of various subjects. I appreciate the opportunity to work and learn from all of you. Moreover, I would like to express my appreciation to Carla and Sharmila for their invaluable assistance, as well as Remko for his outstanding technical support in my RTDS lab testing. I wish all the best and success to all of you in your work, family, and life.

I would like to express my gratitude to my country, China, as my entire Ph.D. work in TU Delft is supported and funded by the China Scholarship Council (CSC).

In the end, some words to my parents:

爸妈, 从高考成绩揭晓的那一刻起, 经历了在交大和米兰理工读研的岁月, 再到代尔夫特大学深造攻博, 转眼间十年已然悄然流逝。这十年间,我走过的每一步, 做出的每一个决定, 都离不开你们无条件的支持和不断的关心与鼓励。海外读博的生涯中, 有艰难, 有枯燥, 有迷茫, 有失落, 也有喜悦, 有激动, 有收获, 有坚定。正因为有了你们作为我不断前进的精神力量源泉和坚定的后盾, 我能够克服一个又一个难关。正如你们所言: "路虽远行则将至, 事虽难做则必成", 前面的道路还会有更大的挑战, 我还有更多梦等待实现, 而我已经准备好了! 感谢你们这些年的耐心等待, 无私的付出和陪伴! 愿你们保重身体, 保持心态, 享受每一个美好的瞬间! 永远爱你们!

Le Liu
Delft, November 2023

CURRICULUM VITÆ

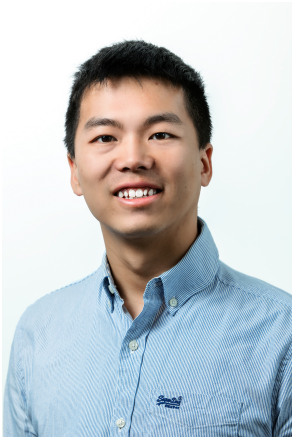

Le Liu was born in Weinan, Shaanxi Province, China, in 1996. He received his bachelor's degree from the Xi'an University of Technology, Xi'an, China, in 2017. He received M.Sc degrees from the School of Electrical Engineering at Xi'an Jiaotong University, China, and Politecnico di Milano, Italy, in 2020. He is now working towards his Ph.D. degree in the Intelligent Electrical Power Grid (IEPG) group at the Delft University of Technology, under the supervision of Prof. Marjan Popov and Dr. Aleksandra Lekić. His Ph.D. project is supported by the China Scholarship Council (Scholarship No. 202006280010).

His main research interests are protection and fault location for MTDC power systems, Nonlinear MMC control, and control interoperability.

LIST OF PUBLICATIONS

Journal papers

1. **L. Liu**, A. Lekić, M. Popov, *Robust Traveling Wave-based Protection Scheme For Multiterminal DC Grids*, IEEE Transactions on Power Delivery, vol. 38, no. 5, pp. 3117-3129, Oct. 2023.

2. **L. Liu**, A. Shetgaonkar, A. Lekić, *Interoperability of classical and advanced controllers in MMC based MTDC power system*, International Journal of Electrical Power & Energy Systems **148**, 108980 (2023).

3. A. Shetgaonkar, **L. Liu**, A. Lekić, M. Popov, P. Palensky, *Model predictive control and protection of MMC-based MTDC power systems*, International Journal of Electrical Power & Energy Systems **146**, 108710 (2023).

Conference papers

1. **L. Liu**, F. Xie, M. Popov, Zhi. Hao, A. Lekić, *Single-ended DC Fault Location Method For MMC-Based HVDC Power System Using Adaptive Multi-step Levenberg-Marquardt Algorithm*, IEEE PES PowerTech Belgrade 2023 (2023).

2. **L. Liu**, A. Lekić, M. Popov, *Robust Adaptive Back-Stepping Control Approach Using Quadratic Lyapunov Functions for MMC-Based HVDC Digital Twins*, 11th International Symposium, ISoLA 2022, **13704**, (2022).

3. F. Xie, **L. Liu**, Zhi. Hao, A. Lekić, M. Popov, *Non-unit DC Line Protection Method for Multiterminal MMC-HVDC System Based on Normalized Backward Traveling Waves*, IEEE PES ISGT Europe 2023 (2023).